Photonic whispering-gallery resonators in new environments

Thesis by
Eric Paul Ostby

In Partial Fulfillment of the Requirements
for the Degree of
Doctor of Philosophy

California Institute of Technology
Pasadena, California
2009

(Defended May 20, 2009)

Acknowledgements

I have immensely enjoyed my time at Caltech, it has been the most challenging and rewarding experience in my life. I owe a debt of gratitude to the many people who contributed to my maturity as a researcher and analytical thinker at Caltech. I would like to first thank my advisor Professor Kerry Vahala. He expertly guided me to success in the many projects I worked on, and I have benefited from his intelligence, creativity, and rigorous approach to science. In spite of his busy schedule, Kerry always made time for individual meetings and easily moved between projects offering insightful advice. Also, Rosalie deserves praise for her fast resolution of any administrative matters and kindness.

No researcher works in a bubble, and so it was in my graduate career. I thank my fellow group members who offered open ears, suggestions, or even their time to help me − Mani Hossein-Zadeh, Lan Yang, Tao Lu, Andrea Armani, Bumki Min, Hansuek Lee, Ivan Grudinin, and Tong Chen. I thank Mani for his advice and mentorship, I based my vacuum chamber design on the first vacuum chamber that he built. Mani and I spent many hours together at Caltech, and I am thankful for the strong friendship we formed. Just when Mani was leaving to become professor, Hansuek Lee joined the group and we formed a close friendship as well. Hansuek taught me advanced fabrication techniques and generously collaborated on the spiral and vacuum reflow projects. I am especially thankful for his help during the last months before graduation, and have enjoyed spending time with him and his growing family. I would also like to thank Joyce Poon for insightful discussions on plasmonics and help with metal evaporation. Raviv Perahia lightened up challenging research with jokes, and also selflessly giving his time to take SEM images.

I cannot imagine my years at Caltech without my two closest friends, Jim Adleman and Johnny Green. Jim and I worked together in Professor Dimitri Psaltis' group for two years, and formed a lifelong bond. I thank Jim for his unwavering support of me − in my research, at Raytheon, and at my wedding in Rio de Janeiro. We shared many laughs, cold pints, and lopsided defeats in GSC basketball games. Johnny and I quickly became great friends, celebrated our Norwegian heritage, and were roommates for one year. Johnny has been a constant companion − encouraging me through the challenges of doctoral research, supporting me as I courted my wife from long distance, and spotting my bench presses. Jim and Johnny are wonderful friends, and they have painted a rich fabric of memories that I will never forget. I also thank all of my other friends, each of you has brightened my day and made my Caltech experience amazing. The students, faculty, and staff at Caltech are brilliant, providing for a diverse and stimulating intellectual environment.

My dream of achieving a doctoral degree in engineering was only possible with the lifelong love and formation I received from my parents, John and Sandy. I thank them for their tireless support, trips to see me, and understanding of the challenges I faced. My parents are my heros − they have given me not only the academic rigor and work ethic necessary to succeed, but most importantly they taught me to be a kind person, to love all good things. Also, I am thankful for the support and love I have received from my brother and sisters – Anna, Tim, Janelle, and Katrina.

Finally, I am most grateful to my wonderful wife Maria Fernanda Oppermann Bento. She has supported me throughout my graduate career, encouraged me on the hard days, and celebrated with me on the good ones. She always showed great interest in my research, and even helped me on several experiments. I am blessed by her love everyday, and thank her for all the sacrifices she has made for us. I respect my wife a great deal, and admire her sensitive heart and kindness towards others. I dedicate this thesis to Fernanda, my true love.

Eric Ostby
May 2009
Pasadena, CA

Abstract

Optical whispering-gallery devices, like the microtoroid or microdisk, confine light at resonant frequencies and in ultra-small volumes for long periods of time. Such ultra-low loss resonators have been applied in diverse areas of scientific research, including low-threshold lasers on-chip, biological sensing, and quantum computing. In this thesis, novel ultra-low loss microstructures are studied for their unique characteristics and utility. The author investigates the interaction between microcavities and various environments in order to quantify the results and lay the foundation for future applications.

The first optical cavity studied is the microtoroid, which possesses ultra-high quality factor (Q) on account of its nearly atomic smooth surface, produced by surface-tension induced laser reflow. Ytterbium-doped silica microtoroids are fabricated by a sol-gel technique. The ytterbium microtoroid laser achieves record-low laser threshold (2 μW) in air, and produces the first laser output for a solid-state laser in water. This laser in water can be developed as an ultra-sensitive biological sensor, with potentially record sensitivity enabled by gain-narrowed linewidth. Also, a novel CO_2 laser reflow and microtoroid testing vacuum system is demonstrated. Fabrication and testing of microtoroids is performed in a vacuum chamber to study the effect of atmospheric water and upper limit of Q in microtoroids.

The selective reflow of microtoroids presents difficulties for integration of on-chip optical waveguides. As an alternative, dimension-preserving low-loss optical structures are researched for their unique applications. A gold-coated silica microdisk is fabricated, and demonstrates record and nearly-ideal quality factor (1,376) as a surface-plasmon polariton resonator. The hybrid optical-plasmonic mode structure is studied in simulation and experiment. The plasmonic resonator has ultra-low mode volume and high field confinement, making it suitable for short-range optical communication or sensing. Finally, a novel whispering-gallery optical delay line in a spiral geometry is designed and experimentally demonstrated. The center transition region of the spiral is optimized for low transmission loss by beam propagation simulation. A 1.4 m long spiral waveguide within a 1 cm^2 area is presented. The spiral waveguide structure is being developed as a real-time optical delay line with fiber-like loss, important for optical communication and signal processing.

Contents

List of Figures

List of Publications

Portions of this thesis have been drawn from the following publications:

Yb-doped glass microcavity laser operation in water E. Ostby and K. Vahala, Optics Letters, **34**, 1153−1155 (2009).

High-Q surface-plasmon-polariton whispering-gallery microcavity B. Min, E. Ostby, V. Sorger, E. Ulin-Avila, L. Yang, X. Zhang, and K. Vahala, Nature, **457**, 455−458 (2009).

Ultralow-threshold Yb3+:SiO2 glass laser fabricated by the solgel process E. Ostby, L. Yang, and K. Vahala, Optics Letters, **32**, 2650−2652 (2007).

A Photon Turnstile Dynamically Regulated by One Atom B. Dayan, A. Parkins, T.Aoki, E. Ostby, K. Vahala, and H. Kimble, Science, **319**, 1062−1065 (2008).

Efficient routing of single photons by one atom and a microtoroidal cavity T. Aoki, A. Parkins D. Alton, C. Regal, B. Dayan, E. Ostby, K. Vahala, and H. Kimble, Physical Review Letters, **102**, 083601 (2009).

Wavelength-independent coupler from fiber to an on-chip cavity, demonstrated over an 850nm span T. Carmon, S. Wang, E. Ostby, and K. Vahala, Optics Express, **15**, 7677−7681 (2007).

Chapter 1

Introduction

1.1 Microcavities

Optical microcavities are small devices that confine light for long periods of time by repeated reflection. They can take different geometric shapes−linear cavities such as vertical-cavity surface-emitting lasers (VCSEL) [1] and distributed-feedback lasers (DFB) [2], or circular cavities like micro droplets [3] and silicon micro-ring filters [4]. Microcavities have made a significant impact in both practical systems and laboratory research due to their small optical mode volume (V) and high quality factor (Q), which is a measure of the photon lifetime in the cavity. Fused silica (SiO_2) is the dielectric material of choice for solid microcavities thanks to its extremely low transmission losses in the optical communication band (1.55 μm). Braginsky and Ilchenko pioneered the study of ultra-high Q microspheres and predicted numerous nonlinear applications [5]. Subsequently, Gorodesky [6] and Vernooy [7] demonstrated silica microspheres with Q as high as 8×10^9, close to the intrinsic loss limits of silica in the visible band. Although higher quality factors are expected at longer wavelengths in the near-infrared (NIR) due to silica's absorption spectrum, in fact the Q did not increase. Both authors considered that the cause may be absorption loss due to water on the surface of or even inside the microsphere.

One requirement for ultra-high quality factor is low scattering caused by surface roughness. Indeed, a microsphere's nearly atomically smooth glass surface (1.7 nm rms roughness [7]) is made possible by surface-tension-controlled melting using a flame [7] or CO_2 laser [8]. The CO_2 laser reflow process, developed by Vahala for microspheres and later applied to microtoroids, can raise the Q factor from 1 million (microdisk) to over 100 million (microtoroid) by reducing surface roughness created during fabrication. Still, it is possible to produce high Q in a non-reflowed silica microdisk by carefully controlling the cavity mode profile. Kippenberg demonstrated a silica microdisk with Q as high as 60 million, by confining the optical mode away from the disk perimeter (where etch roughness is greatest) with a wedge feature [9].

The silica microtoroid is a planar on-chip resonator that was invented at Caltech and first reported by Armani [10]. Toroidal microcavities can confine light in ultra-small mode volumes (V =100 μm^3) [11] for photon lifetimes as long as 300 ns [12], and are easily fabricated on a silicon substrate [10].

Long photon lifetime and nearly ideal fiber taper coupling [13] of microtoroids enables researchers to experimentally observe nonlinear effects such as Raman scattering [12], parametric oscillation [14], third-harmonic generation [15], and radiation-pressure-driven mechanical oscillations [16]. The high Q/V figure for microtoroids, significantly better than that of microspheres, is important for cavity quantum electrodynamics (cQED) research. Aoki achieved strong coupling for the first time between the electromagnetic field of a microtoroid cavity and a cesium atom [17], made possible by more than 100,000 average round trips made by each photon. Photons are confined in the microtoroid cavity by repeated total-internal reflection, thus forming the whispering-gallery mode (WGM) structure of toroids. In every microcavity, a portion of the WGM's power resides outside of the cavity, this is the evanescent field component. The evanescent field in microtoroids allows fiber taper coupling of pump light, and makes the microtoroid extremely sensitive to both its own defects and the environment. High sensitivity to water vapor and dust limits the open-air quality factor of toroids over long periods of time. But, many benefits of the long interaction length and large interaction cross-section can be found. Armani demonstrated low-concentration biological sensing of interleukin-2 molecules with a silica microtoroid[18].

Microtoroids are naturally an ideal platform for making low-threshold single-frequency lasers. High quality factors permit laser action at very low concentrations (0.01% atm.), and small toroid diameters reduce the number of laser modes by virtue of the large free-spectral range (FSR) [19]. Yang adapted the solgel technique for making silica thin-films to fabricate single-frequency erbium-doped glass microtoroids [20], and Min studied ion-implanted erbium-doped microcavities [21].

1.2 Thesis outline

This thesis presents the author's scientific research into the physics defined by the interaction of high Q silica microcavities and materials including silver thin films, ytterbium ions, cesium ions, and water. The goal is to understand how these unique systems function, and explore applications that include optical communication, sensing, and cavity quantum electrodynamics. Low loss optical fiber tapers provide coupling of optical radiation to and from the resonator. As the basis for much of this work, microtoroid fabrication and experimental testing are first discussed in **Chapter 2**.

The previous work in erbium-doped silica microtoroid lasers by Yang paved the way for the investigation of ytterbium-doped lasers [20]. The first Yb:SiO_2 toroidal microcavity laser is demonstrated with a record-low pump threshold of 2 μW and single-frequency operation [19]. The laser performance is completely characterized in **Chapter 3**. In addition to several unique laser properties, ytterbium was chosen as the gain medium for its laser emission at 1 μm, where the absorption coefficient of water is 75 times less than at 1.5 μm [22]. **Chapter 4** explores the author's demonstration of the first-ever microcavity laser in water [23]. Simulation of the microtoroid laser in water is performed to find the optimum combination of doping concentration and toroid major diameter. This laser produces more than 2 μW of stable output power while completely submerged in water, opening up the possibility of an active laser sensor due to its narrow linewidth compared to passive cavities.

Chapter 5 focuses on the author's research on the interaction between high Q glass microresonators and metal thin films. Surface plasmon polaritons (SPPs) are electron density waves excited at the interface between metals and dielectric materials. Plasmonic waveguides and resonators are being intensely studied for possible applications in short-range communications, sensing, and filtering given their high field intensity and small mode volume [24, 25, 26, 27, 28]. The author, in collaboration with Bumki Min, demonstrates a high Q WGM microcavity constructed of a silica microdisk coated with a thin layer of silver [29]. The geometrical shape formed by specific fabrication techniques produced a SPP resonator with a record Q factor of 1,376, more than an order of magnitude higher than the previous micro-ring measurement [27]. The results of experimental measurement and finite-element modeling describe the operation of this plasmonic microcavity.

The issue of absorption loss due to water in silica microspheres was already mentioned. The author has directed research into the effects of water on microtoroids, with the purpose of increasing the current ultra-high quality factors ($Q < 5 \times 10^8$). **Chapter 6** presents the author's research into the affect of water on microtoroids. A novel vacuum chamber has been designed, built, and tested for laser reflow and fiber taper testing of microtoroids in vacuum. The aim of vacuum reflow is to eliminate any water that may limit Q. Laser reflow of microtoroids in vacuum has been demonstrated, and microtoroids with $Q = 2.2 \times 10^8$ have been fabricated. Continued research aims to increase quality factor as high as 1×10^{10}, due to the clean and dry vacuum environment.

The benefit of a wedge structure at the outer edge of the microdisk was previously highlighted. By confining the optical mode away from roughness caused by etching, the quality factor of microcavities can be increased by an order of magnitude. Putting this new technology to work, the author directed research into wedged whispering-gallery spiral waveguides for optical delay as described in **Chapter 7**. The WGM waveguides are only several microns in diameter, which allows them to be tightly packed into a spiral geometry. The spiral waveguide can provide over 1 m of optical delay packed into a 1 cm^2 surface area, a time delay sufficiently long enough to have applications in optical communications and laser-radar. Beam propagation simulations are performed for optimization of the center region of the spiral, where the WGM power flow changes direction from clockwise to counterclockwise. Spiral waveguides were designed, fabricated, and tested using a dual-taper coupler.

Also, the author developed the concept and performed simulations of a new short pulse microcavity laser. The pulsed laser consists of a Cr,Yb-doped silica microtoroid fabricated by the solgel method. Laser simulations included in **Chapter 7** predict the passive Q switched laser pulses to have 100 pJ energy and 1 ns duration.

In addition, the author contributed to the cavity quantum electrodynamics research of Professor Kimble at Caltech. Small mode volume and high-Q microtoroids were fabricated for experiments studying the interaction between the microtoroid's electromagnetic field and cesium atoms. Dayan demonstrated the first microcavity-atom photon turnstile in an experiment with a microtoroid [30]. Also, Aoki improved the efficiency of the single photon router to 60% by overcoupling the microtoroid and fiber taper [31].

Chapter 2

Ultra-high Q microtoroid

2.1 Microtoroid resonator overview

The silica microtoroid is an ultra-high Q (UHQ) and ultra-small mode volume microcavity fabricated on silicon using standard microelectronics techniques. Although silica microspheres have shown higher quality factors than microtoroids (8×10^9 compared to 5×10^8), their geometry and fabrication method present practical limitations [32]. The physical dimensions of a microsphere are difficult to control during melting, since there is no physical stop for the surface-tension induced reflow. Secondly, the microsphere's mode spectrum is more dense and complicated than the microtoroid, because the optical mode is not restricted in azimuthal and vertical degrees of freedom as the microtoroid is [33]. These challenges, and lack of planar integration of the microsphere in a compact package, led to the invention of the microtoroid [10]. The microtoroid is the first microcavity that offers ultra-high quality factor on silicon. The highest Q factor recorded in a microtoroid to date is 4×10^8, which corresponds to a cavity finesse ($F = \frac{\lambda Q}{\pi n D}$) of 1×10^6. Also, the microtoroid's cavity dimensions can be accurately controlled during fabrication to produce the desired resonator. For instance, small diameter toroids are needed for cQED experiments, where as larger toroids are important for laser operation in water.

A SEM image of a typical silica microtoroid is shown in Figure 2.1, with 60 μm major diameter (D) and 5 μm minor diameter (d). After fabrication, the microtoroid can be described as a glass ring cavity with a dumbbell-like cross section, suspended over a silicon pillar by a silica membrane. In microtoroids, like optical fiber and microspheres, the silica is amorphous. Alternatively, crystalline quartz rods have been carefully polished into WGM resonators with ultra-high Q (5×10^9) [34]. The advantage of amorphous silica is that it can easily be melted or drawn into the desire shape, though care should be taken not to freeze significant refractive index variations in the glass that cause scattering loss. Input light, for example from a fiber taper, orbits the microtoroid confined by TIR until it is absorbed, scattered out, or coupled out by another waveguide.

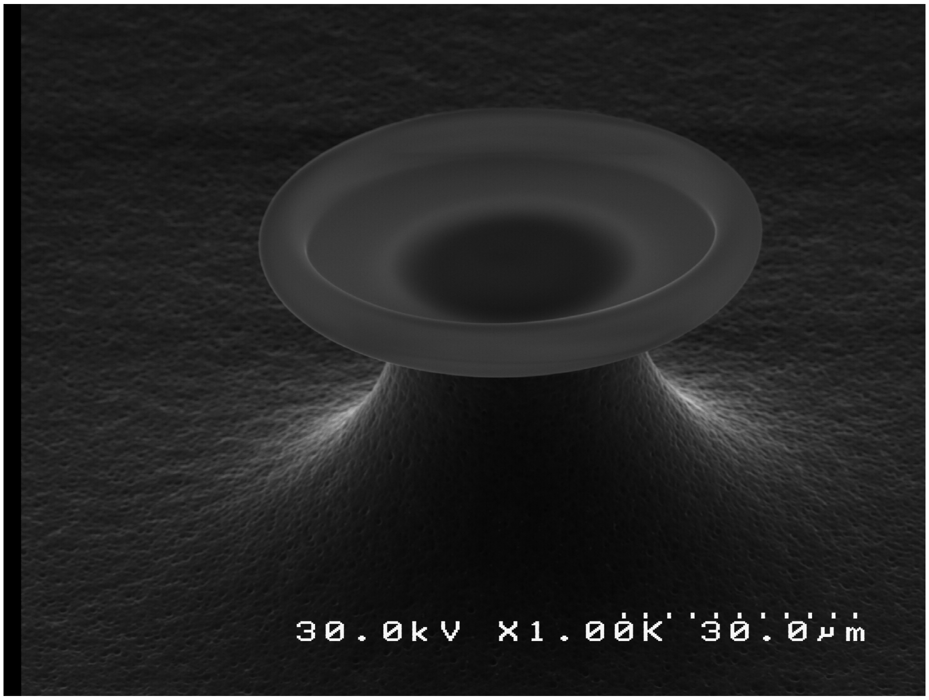

Figure 2.1. SEM image of a UHQ microtoroid resonator with 60 μm major diameter (D) and 5 μm minor diameter (d)

2.1.1 Whispering-gallery mode structure

The spatial confinement of microtoroids supports less transverse and radial modes than microspheres. These are whispering-gallery modes, so named because the photons circulate at the surface of the glass microcavity in a similar manner as sound waves do around the dome in St. Paul's Cathedral in London. Unlike the complete theory developed for microspheres, analytical expressions for the microtoroid mode structure are not possible because only one coordinate of the wave equation is separable. Therefore, the two-dimensional Helmholtz equation must be solved numerically, or by semi-analytical methods [35]. Sean Spillane developed a model of the 2D cross section of the microtoroid including rotational symmetry using a finite element eigenmode solver (Femlab). This full-vectorial model gives accurate solutions of the toroid's electromagnetic field distribution. The model can also calculate cavity mode volume, radiation Q, and resonance wavelengths. Figure 2.2 is a cross-sectional plot of two microtoroid cavity modes.

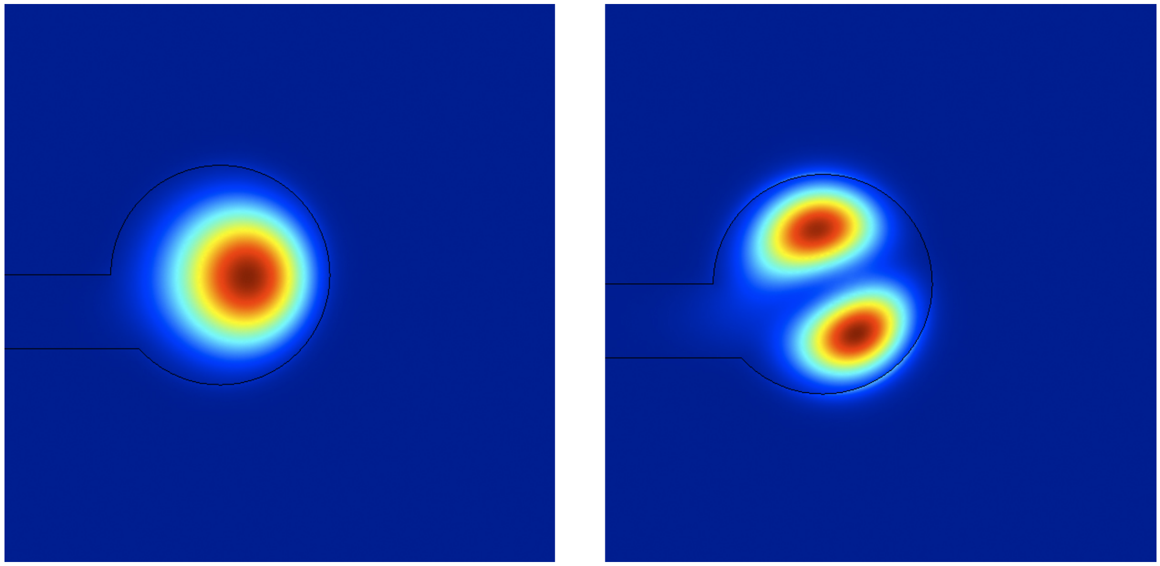

Figure 2.2. Plot of the electric field intensity profile $|E_\phi|^2$ of a 120 μm diameter toroid, showing the fundamental mode (left) and a higher-order mode (right). The field profiles are calculated by a FEM simulation of the microtoroid

To give a theoretical overview of the microtoroid cavity, the equations describing the microtoroid's mode structure are briefly detailed. To determine the proper description, start with Maxwell's equations in an isotropic charge free medium following Yariv [36].

$$\nabla \times \mathbf{H} = \varepsilon \frac{\partial \mathbf{E}}{\partial t} \tag{2.1}$$

$$\nabla \times \mathbf{E} = -\mu \frac{\partial \mathbf{H}}{\partial t} \tag{2.2}$$

$$\nabla \cdot (\varepsilon \mathbf{E}) = 0 \tag{2.3}$$

After taking the curl of Equation (2.2) and substitution, the expression becomes

$$\nabla^2 \mathbf{E} - \mu\varepsilon \frac{\partial^2 \mathbf{E}}{\partial t^2} = -\nabla(\frac{1}{\varepsilon}\mathbf{E} \cdot \nabla\varepsilon) \tag{2.4}$$

Next, write the field components $(H_r, H_\phi, H_z, E_r, E_\phi, E_z)$ in cylindrical coordinates, which is logical because of the microtoroid's rotational symmetry. For instance, the electric field $\mathbf{E}$ is written

$$\mathbf{E}(r, \phi, z, t) = \mathrm{Re}[\mathbf{E}(r, \phi, z)e^{iwt}] \tag{2.5}$$

The coordinate axis with respect to the toroid are shown in Figure 2.3.

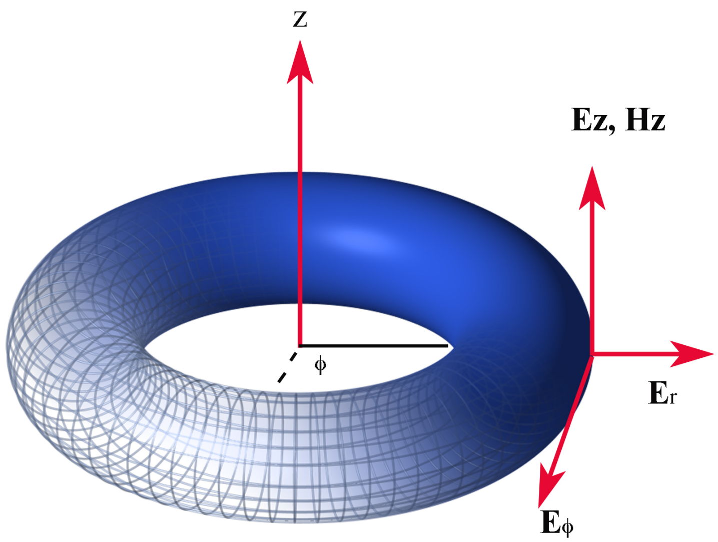

Figure 2.3. Diagram of a toroid with field components in cylindrical coordinates for the TM-type whispering-gallery modes

Next, set the right side of Equation (2.2) equal to zero, since the permittivity of the medium is constant over one wavelength. After taking the double partial differential of **E**, one produces the famous wave equation:

$$(\nabla^2 + \mu\varepsilon w^2)\mathbf{E} = 0 \tag{2.6}$$

Now, the scalar wave equation approximation can be applied because the refractive index is constant over a wavelength in the microtoroid, and the whispering-gallery mode polarization is preserved. Also, apply the substitution of $\mu\varepsilon = \mu_0\varepsilon_0 n^2 = n^2/c^2$. The resulting expression is the scalar wave equation for propagation in a dielectric medium, also known as the Helmholtz equation.

$$(\nabla^2 + \frac{w^2n^2}{c^2})E = 0 \tag{2.7}$$

The microtoroid modes, solutions to Equation (2.7), have either transverse-electric (TE) or transverse-magnetic (TM) polarization in the cavity. In TE modes, the electric field oscillates in the (r, z) plane, transverse to the propagation direction (along ϕ), and hence $E_\phi = 0$. Likewise, in TM modes the magnetic field oscillates in the (r, z) plane and $H_\phi = 0$. The four remaining field components can be expressed with two field components ($H\phi$ for TE modes, and $E\phi$ for TM modes). After expanding the Laplacian operator, the scalar wave equation in terms of E_ϕ is

$$\left[\frac{\partial^2}{\partial r^2} + \frac{\partial}{r\partial r} + \frac{\partial^2}{r^2\partial\phi^2} + \frac{\partial^2}{\partial z^2} + \frac{w^2n^2}{c^2}\right] E_\phi = 0 \tag{2.8}$$

Next, separate variables and express the electric field as $E_\phi = E_\phi(r, z)e^(\pm il\phi)$, where l is the angular mode number.

$$\left[\frac{\partial^2}{\partial r^2} + \frac{\partial}{r\partial r} - \frac{l^2}{r^2} + \frac{\partial^2}{\partial z^2} + \frac{w^2n^2}{c^2}\right] E_\phi(r, z) = 0 \tag{2.9}$$

After arranging the terms, one reaches the Helmholtz equation in partial differential format.

$$\left(\frac{\partial}{\partial r}\frac{1}{r}\frac{\partial}{\partial r} + r\frac{\partial^2}{\partial z^2}\right) E_\phi + \left(\frac{w^2n^2}{c^2} - \frac{l^2}{r^2}\right) rE_\phi = 0 \tag{2.10}$$

The whispering-gallery mode profiles can be calculated by using a FEM solver, like Femlab, to simulate the partial differential equations describing the optical field in a microtoroid. In addition to mode profiles, it is possible to calculate the mode volume and radiation Q of specific microtoroid resonators. Figure 2.2 is a plot of the fundamental WGM for a 120 μm major diameter and 3 μm minor diameter toroid generated by Femlab.

2.2 Microtoroid fabrication

2.2.1 Photolithography and wet etching

Microtoroids are easily fabricated using standard microelectronic fabrication techniques in a process developed by Armani [10]. A diagram showing the fabrication steps is given in Figure 2.4.

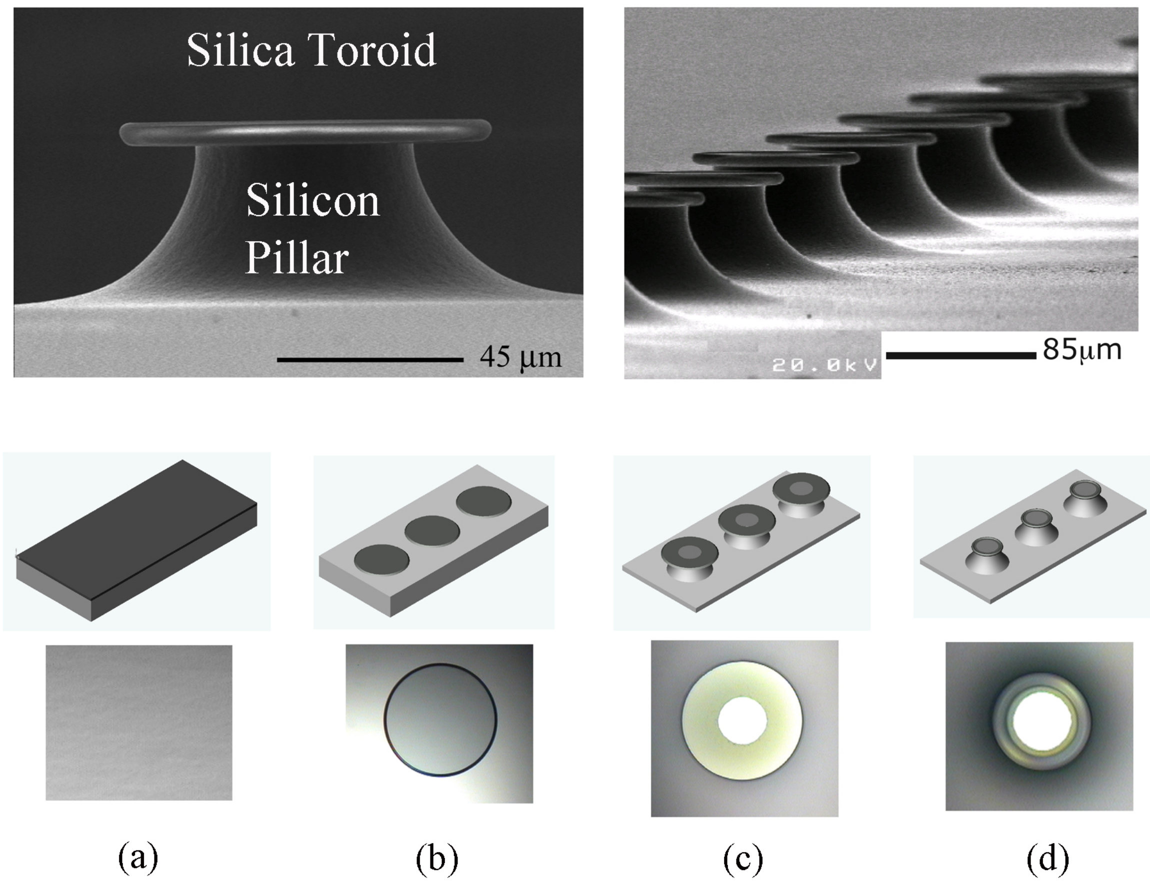

Figure 2.4. Diagram of the fabrication steps of silica microtoroids. (a) First, a photoresist layer is deposited on a SiO_2-on-Si wafer. (b) After photolithography, an HF wet etch creates silica pads. (c) A high-selectivity XeF_2 dry etch isolates silica microdisks from the silicon substrate. (d) Finally, CO_2 laser reflow produces a microtoroid.

First, start with a (100) prime silicon wafer with a 2 μm layer of thermally grown oxide (SiO_2) on top. If necessary, clean the wafer with acetone and isopropyl-alcohol, and dry with nitrogen gas. After the surface is treated with HMDS for 2 minutes to promote surface adhesion, spin coat a uniform layer of Shipley 1813 photoresist onto the wafer at 3,000 rpm. Soft-bake the wafer at 90°C to remove solvents. Next, use a mask aligner (Carl Zuss MJ-BA3) to expose the photoresist with a mask containing arrays of disks (40−180 μm diameter). Stir the exposed wafer in developer until the developing process is complete, normally 30 seconds. For positive resists like S1813, exposed photoresist becomes soluble in developer and is washed away. Left behind are crisp circular pads of photoresist covering the oxide layer. Next, a hard bake is performed at 110°C to reflow the photoresist pads and prepare for wet etching. The photoresist disk pattern is transferred into the oxide layer by a 19 minute buffered-oxide etch (BOE), in a 2% hydrofluoric acid (HF) solution. The HF etch undercuts the photoresist by a controllable amount, depending on the adhesion strength of resist to the oxide, and any extra etching time added. The HF undercut produces a bevel on the edge of the circular microdisks of the oxide (SiO_2). Normally, this bevel has an angle of 45° with respect to the disk plane, but the angle can be reduced to less than 10°. Small bevel angles are key to high Q in microdisks, which will be discussed in **Chapter 5**.

At this stage in the fabrication, the silica microdisks cannot support whispering-gallery modes because any circulating optical radiation will leak into the higher index silicon substrate. Therefore, a pulsed XeF_2 isotropic dry etch is used, which selectively etches the silicon approximately 1,000 times faster than silica. The etch rate ($\Delta D/\Delta T$) for 4 chips (5×20 mm size) with 100 μm diameter disks is measured to be 0.01 μm per minute for sequential 90 s pulses, depending on the total silicon surface area and pillar diameter. The etch rate is inversely proportional to the pillar diameter as shown in Figure 2.5.

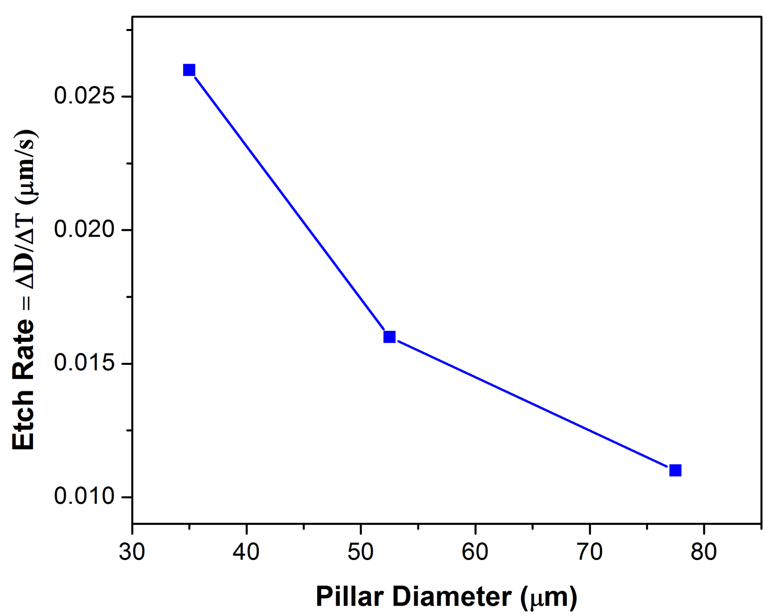

Figure 2.5. Plot of the etch rate of silicon ($\Delta D/\Delta T$) as a function of pillar diameter observed for one microdisk. The etch rate is inversely proportional to the pillar diameter.

The chemical reaction during XeF_2 etching is described by $2XeF_2 + Si \rightarrow 2Xe + SiF_4$. The dry etch should continue until the desired diameter of the silicon pillar is reached, for instance a 40 μm pillar for a 100 μm diameter disk. It is important to note that the silicon chip must be dry before etching. Otherwise, any water on the chip will react with the xenon difluoride gas to produce HF, which etches oxide rapidly and produces surface roughness on the microdisk [37]. After the dry etch, the undercut silica microdisk is supported on a silicon pillar. Microdisks normally have Q factors near 1×10^6, limited by scattering from lithographic and etching roughness. Since the microdisks are fabricated on silicon by standard lithography techniques, they can be easily integrated with other devices on chip, like modulators or detectors.

2.2.2 CO_2 laser reflow

While lasers [9] and plasmonic resonators [29] have been developed using microdisks, the benefits of higher quality factor are well known [38]. Higher Q leads to lower threshold lasers, more sensitive detectors, higher resolution filters, and higher strong coupling coefficients for cQED. After care has been taken to preserve high Q in microdisks by eliminating all contaminants and defects, the quality factor can be increased by an order of magnitude or more by CO_2 laser reflow.

At the CO_2 laser wavelength, 10.6 μm, the absorption cross section of silica is 100 times larger than silicon. Hence, the thermally conductive silicon pillar functions as a circular heat sink, and the silica microdisk is melted to form the toroid geometry. The newly minted glass microtoroid has nearly atomic smooth finish due to surface-tension, like microdroplets [39] and microspheres [6].

A 10 Watt CO_2 laser (Synrad Corp.) is controlled either manually for continuous-wave (cw) power, or by a function generator for pulsing. The author performed laser reflow in three different manners on almost identical microdisks on the same silicon chip to determine the optimum reflow setting. In the first method, the laser is operated in quasi-cw mode, and the laser power is increased steadily until the silica microdisk melts into a microtoroid. In the second method, a single square pulse with 100 ms duration is sent from a function generator to the laser. In the third method, the laser is also controlled with the function generator, but the single 100 ms pulse waveform follows a linearly increasing ramp function. After testing the toroids fabricated according to these three methods, the Q factors were highest for method three. Therefore, the author chose to reflow all microtoroids in the future using the ramp waveform and a single pulse with 100 ms duration. If the laser power (controlled by the peak-to-peak voltage from the function generator) is too low, then the reflow will not be complete and the toroid may be asymmetric. On the other hand, if the laser power is too large, then silicon material can be sputtered onto the toroid and cause absorption loss. For each initial disk diameter and pillar size, there is an optimum reflow power that must be experimentally determined.

2.3 Experimental testing of microtoroids

The standard experimental measurements performed on silica microtoroids for the research presented in this thesis are discussed in detail here. The main elements of toroid testing include: optical excitation of the microcavity by a fiber-coupled tunable laser, coupling of light into and out of the microtoroid with an adiabatic fiber taper, and finally any post-processing of the output light (e.g., wavelength filtering) and optical detection (i.e., conversion from optical to electrical power).

Fiber-coupled semiconductor laser diodes generate optical radiation at 970 nm or 1550 nm for the experiments presented in this work. The lasers are single-frequency and have a bandwidth of less than 300 kHz. The lasers are optically isolated to prevent reflected light from causing laser instability, and the laser is tuned over a wavelength range of more than ten nanometers. Light can be coupled into a microcavity in several ways, including prisms [6], end polished fibers [40], free-space coupling, or fiber tapers [41].

2.3.1 Low-loss optical fiber coupling to microcavities

Tapered optical fibers can excite whispering-gallery resonators with higher efficiency and ideality than any other coupling mechanism [13]. Fiber taper coupling to cavities was first demonstrated with microspheres [42]. Coupling between a taper and any microcavity relies upon the physical overlap and vector phase matching of the evanescent field components of the fiber taper and the microtoroid. With proper phase matching for critical coupling, it is possible to excite the resonator with 100% of the input radiation, made possible by the tapered optical fiber's record ideality (99.999%) [13]. With low transmission loss, low scattering during coupling, and flexible phase-matching, there is no better laboratory tool for probing microcavities than fiber tapers.

2.3.1.1 Fiber taper fabrication

A straight fiber taper is made by pulling a standard single-mode fiber (SMF) at a constant speed (using motors attached to both sides of the fiber) over a hydrogen flame. As the fiber heats up and melts, its diameter is adiabatically reduced until the desired diameter is reached, usually $1-2$ μm. The taper length and final diameter are controlled by adjusting the gas flow rate, the pulling speed, and the flame location. Single-mode tapers can be fabricated with extremely low transmission losses, enabling efficient and ideal coupling to ultra-high Q microtoroids.

Straight fiber tapers are only well phase-matched to a specific microtoroid over a modest wavelength range, roughly 100 nm. For wavelengths outside of this phase-matching range, the optical field phase fronts inside the straight taper is mismatched from the optical field inside the curved resonator. Therefore, the author helped develop a bent fiber taper with a circular twist in the middle [43]. If the radius of curvature of the bent taper fiber matches the microtoroid, coupling is observed

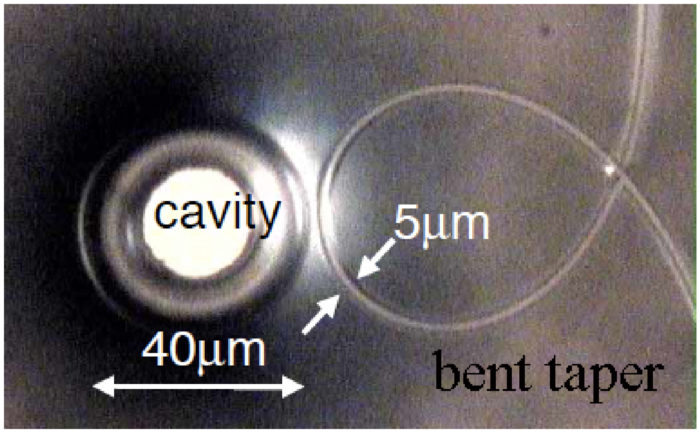

Figure 2.6. Image of a bent fiber taper coupled to a microtoroid. The taper diameter is as small as 5 μm in the center, and the loop diameter is 50 μm.

between the taper and microtoroid over an 900 nm wavelength range from 670 nm to 1570 nm. To make a bent tapered fiber, a straight taper is first pulled from standard SMF. Next, the two sides of the taper are pushed toward one another, forming a circular loop as the taper crosses itself. The fiber positions are carefully controlled to create the desired bent taper diameter, and the loop is frozen into place with gentle heating. The result is a tapered fiber, shown in Figure 2.6 with a circular loop in the center, that can be used to couple optical radiation to a microtoroid over a large bandwidth.

2.3.1.2 Fiber taper phase matching

The taper and toroid must be phase matched to allow efficient optical coupling from one to the other. Therefore, the effective mode indices of the taper (n_{tap}) and toroid (n_{tor}) must be equal. First, the effective mode index of the toroid (n_{tor}) is determined using the previously mentioned finite-element model. Then, the fiber taper mode index is calculated by solving for the propagation constant (β) of light in the fiber. Key physical constants include the fiber core's index of refraction (n), the taper radius (a), and the propagation constant of light ($k_0 = 2\pi/\lambda$). To simplify the final expression to be solved, several dependent variables can be defined [36].

$$
\begin{aligned}
q &= \sqrt{\beta^2 - k_0^2} \\
h &= \sqrt{n^2 k_0^2 - \beta^2} \\
\mathrm{R} &= \sqrt{-\left(\frac{n^2-1}{2n^2}\right)^2 \left(\frac{\mathrm{K}_2(qa)}{qa \cdot \mathrm{K}_1(qa)}\right)^2 + \left(\frac{\beta}{nk_0}\right)^2 \left(\frac{l}{q^2a^2} + \frac{1}{h^2a^2}\right)^2} \qquad (2.11)
\end{aligned}
$$

After solving the wave equation for the dielectric fiber taper with no cladding, a transcendental

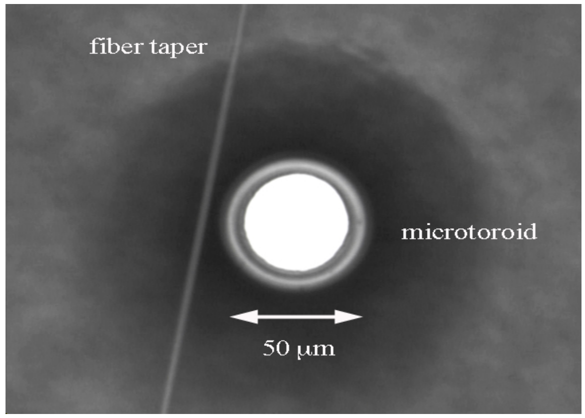

Figure 2.7. Top view image showing coupling between a microtoroid ($D = 50\ \mu$m) and fiber taper

equation is derived that can be graphically solved for β, the propagation constant.

$$\frac{\mathrm{J}_0(ha)}{ha \cdot \mathrm{J}_1(ha)} = \frac{1}{h^2a^2 - \mathrm{R}} - \left(\frac{n^2+1}{2n^2}\right)\left(\frac{\mathrm{K}_2(qa)}{qa \cdot \mathrm{K}_1(qa)}\right) \tag{2.12}$$

After solving for β, the taper mode index is easily calculated as $n_{tap} = \beta/k_0$. To achieve phase matching between the taper and toroid, ensure that $n_{tap} = n_{tor}$. The fiber taper index is matched to the toroid mode by choosing the correct fiber taper radius, a. Normally, the fiber taper is pulled to a minimum diameter less than optimum for phase matching, and the taper position is adjusted with respect to the microtoroid until the phase matched diameter is found. A coupling setup showing the fiber taper waveguide and microtoroid resonator is shown in Figure 2.7.

2.3.2 Quality factor

Silica microcavities can be classified by the optical Q of their WGM resonances−lithographically defined micro-rings ($Q \sim 10^5$), microdisks ($\sim 10^6$), microtoroids ($\sim 10^8$), and microspheres ($\sim 10^9$). The Q factor can be expressed in terms of the linewidth (in frequency or wavelength) of the cavity resonance.

$$Q = \frac{\lambda}{\Delta\lambda} \tag{2.13}$$

Where $\Delta\lambda$ is the full-width at half-maximum (FWHM) of the resonance lineshape. Or alternatively, the cavity Q can be calculated in terms of the photon lifetime.

$$Q = w\tau \tag{2.14}$$

These different but equivalent expressions for Q highlight the two methods that can be used to quantify the intrinsic Q. The first and simplest measurement of cavity Q is quantified in Equation (2.13). This method requires a measurement of the cavity linewidth ($\Delta\lambda$) with the taper and toroid in the undercoupled regime. The injected optical power is kept low ($P < 10\,\mu$W) to avoid thermal broadening of the cavity linewidth, which will be discussed in Section 2.3.3. To make the measurement, the tunable laser wavelength is linearly scanned at 10 Hz. The taper transmission, which exhibits a dip at the cavity resonance, is measured using a low noise optical detector. Finally, the toroid's resonance lineshape is captured with an oscilloscope, and fit to a Lorenzian function to calculate the width ($\Delta\lambda$) as presented in Figure 2.8. Surface roughness or internal scattering (e.g., index modulation) cause back-scattering in the microtoroid, which splits the previously degenerate cavity resonance into a doublet (two Lorenzian resonances) as shown [44].

If a series of measurements of the linewidth are made and plotted as a function of the taper-toroid gap width, then the intrinsic Q (approached asymptotically) can be calculated by fitting the lineshape. Though the cavity linewidth measurement is the quickest way to estimate Q, this technique is only accurate for cavity linewidths larger than the tunable laser's linewidth (300 kHz). Therefore, the resonance linewidth measurement is only accurate for Q less than 3×10^8.

Alternatively, the toroid intrinsic Q can be accurately determined by a cavity ringdown measurement, a technique that is unaffected by thermal distortion of the cavity linewidth and the laser linewidth. The fiber taper is aligned in critical coupling with the toroid (i.e., $T = 0$) while the laser wavelength is scanned in time like the previous method. At precisely the point when maximum power is coupled into the toroid, the laser excitation is gated off using a high speed, external phase modulator. Afterwards, the taper output power is due entirely to the exponential decay of energy stored in the toroid resonator. The taper output power is recorded in time using a high speed detector and oscilloscope. The cavity lifetime is measured by fitting an exponential to the taper transmission. The result of a cavity ringdown measurement is shown in Figure 2.9. It is important to note that this lifetime for critical coupling (τ_{cc}) is smaller than the intrinsic lifetime (τ_0) due to cavity loaded by the fiber taper. To calculate the intrinsic Q factor, it is necessary to account for taper loading and back-scattering in the resonator that couples the clockwise and counterclockwise modes.

The frequency splitting ($2\gamma^{-1}$) between the doublet modes is proportional to the amount of back-scattering. With measurements of the loaded lifetime and splitting, the intrinsic Q can be calculated using the following equation.

$$Q_0 = w\tau_0 = \frac{2w}{\tau_{crit}\left(\frac{1}{\tau_{crit}^2} - \frac{1}{\gamma^2}\right)} \tag{2.15}$$

The record microtoroid Quality factor is currently 4×10^8, observed by Tobias Kippenberg in a 70 μm toroid [12]. The author's research into the upper limit of Q factor in microtoroids is discussed

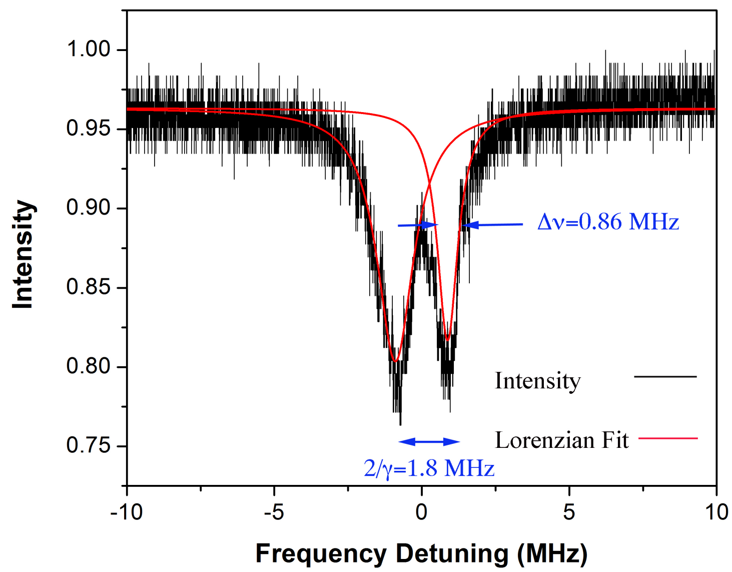

Figure 2.8. Plot of the taper transmission versus laser detuning frequency, showing a characteristic doublet mode of a microtoroid ($D = 55\ \mu$m). The resonance lineshape of each mode (black) is fit to a Lorenzian (red). The sub MHz linewidth ($\Delta\nu$) of one resonance and the splitting frequency (γ^{-1}) are also marked.

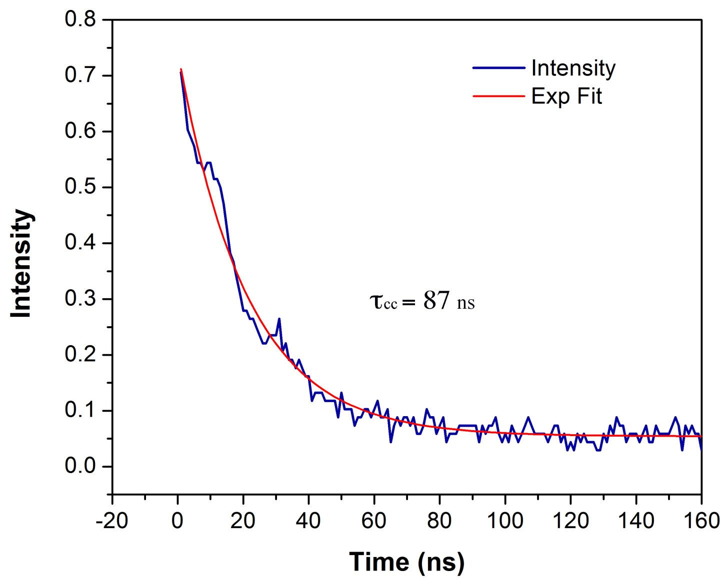

Figure 2.9. Plot of the power emitted from a critically coupled microtoroid during cavity ringdown measurement. The cavity output is recorded after the input is gated off by a modulator. The intensity decay in time is fit to an exponential, and the cavity ringdown lifetime (τ_{cc}) at critical coupling is calculated.

in **Chapter 6**.

2.3.3 Thermal broadening

Microtoroids exhibit thermal broadening of ultra-high Q resonances for moderate input powers due to the low thermal conductivity of silica and the toroid's small mode volume. Resonant buildup of cavity energy can create large amounts of circulating power. For instance, 1 mW of input power critically coupled into a microtoroid with $Q = 1 \times 10^8$ can produce 100 W of circulating power (see Equation (2.16))! For a 50 μm diameter toroid, 100 W of internal power corresponds to a circulating intensity of 1 GW/cm^2, sufficient to observe many nonlinear phenomena.

$$P_{circ} = \left(\frac{4\lambda Q_0}{9\pi^2 nD} \right) P_{in} \tag{2.16}$$

The temperature of the microtoroid cavity will increase with such a large amount of power is circulating inside the glass. As a result, the microtoroid's resonance location will red-shift (towards longer wavelengths), due to the positive thermal coefficient of the refractive index of silica ($\frac{dn}{dT} = 1.3 \times 10^{-5} K^{-1}$) [45]. Also, the thermal expansion coefficient of silica ($\alpha_T = 5.5 \times 10^{-7}$) induces a smaller red-shift of the resonance location.

The normal red-shift of the cavity resonance is illustrated in Figure 2.10, where the normal Lorenzian lineshape has broadened into a triangle. The broadening occurs as the laser wavelength is swept upwards in time, shown by the plot of the laser piezo voltage. The laser wavelength is linearly increased in time, and as the taper-cavity coupling approaches critical coupling, the circulating power in the toroid increases linearly. As a result, the resonance location moves towards longer wavelengths, lengthening the amount of time required to reach critical coupling and thereby broadening the resonance. At critical coupling, the cavity power is maximum, and therefore the resonance location cannot move further. Finally, the laser wavelength (still increasing in time) moves past the cavity's shifted resonance wavelength, and the taper transmission snaps quickly back to 100%. But, when the laser wavelength is scanned downwards in time (shown on the left side of Figure 2.10), the cavity resonance width is artificially compressed as the resonance red-shifts against the blue-tuning laser. In summary, the positive thermal coefficients (thermal and expansion) of silica at room temperature cause thermal broadening of the resonance when the pump wavelength is tuned upwards, and contraction for negative tuning. A helpful review of the thermal effects in silica microtoroids has been written by Carmon [46].

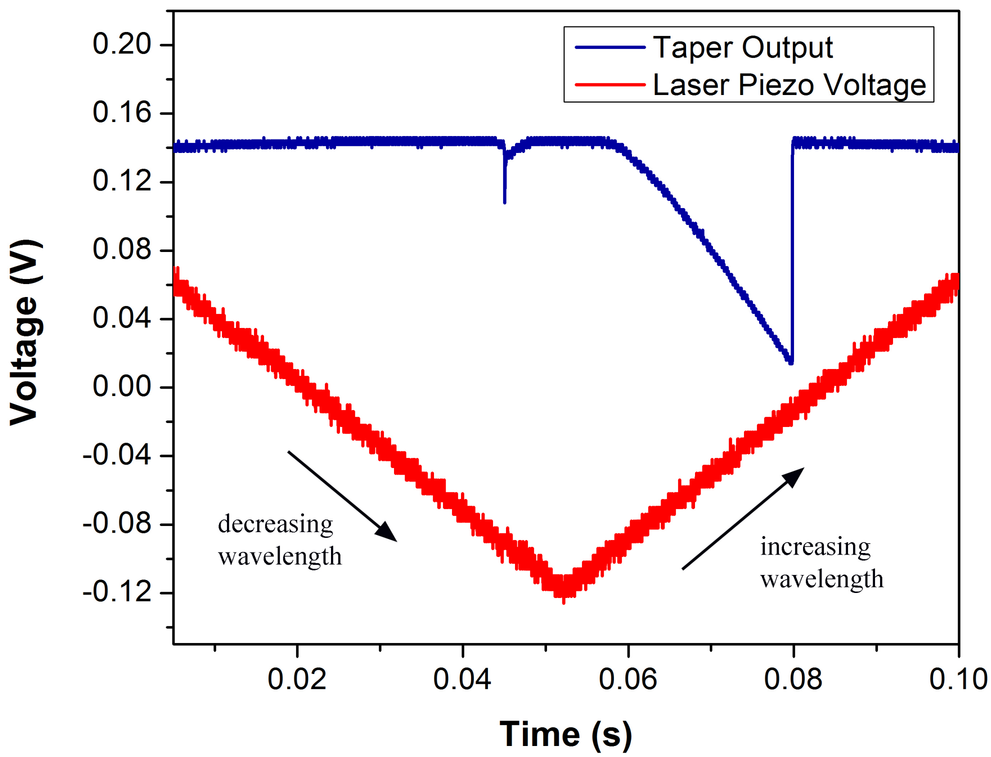

Figure 2.10. Plot of the taper transmission in time (shown in blue) and the laser piezo voltage (shown in red) when critically coupled to a microtoroid exhibiting thermal broadening due to $+\delta n/\delta T$. The normal Lorenzian mode is broadened when the laser wavelength is increased in time (positive slope for laser piezo−right side), and the resonance is narrowed in time when the laser wavelength is swept downwards (negative slope for laser piezo−left side).

2.3.4 Inverse thermal broadening

Thermal broadening can be exploited to stabilize the taper and toroid coupling. If the laser frequency is detuned to the blue-shifted side of the broadened resonance (left side of triangle), then any perturbations such as temperature, coupling, or frequency jitter of the laser will be compensated by the thermal effect. However, blue-shifted photons (lower wavelength) cause heating of the toroid mode. If the total thermal coefficient of silica could be made negative, then a pump laser could be stabilized on the red-side of a toroid cavity resonance, which would cool the toroid mode. Laser cooling of microcavities is very important, for it would aid researchers in reaching the quantum mechanical ground state of a macroscopic object [47]. Kippenberg has demonstrated side-band resolved cooling of a microtoroid, using a state-of-the-art feedback system for stabilizing the laser wavelength on the red-side of the cavity resonance [48].

The author has successfully demonstrated stabilized laser coupling on the red-side of a microtoroid resonance. The thermal coefficient of refractive index of the cavity mode was changed from positive to negative with a thin polymer coating. Polymethyl Methacrylate (PMMA) has a negative thermal coefficient of refractive index ($\frac{dn}{dT} = -1.2 \times 10^{-4}\mathrm{C}^{-1}$) [49], however its optical loss ($\alpha = 23\,\mathrm{m}^{-1}$) is greater than silica's at $\lambda = 1550$ μm [50]. To demonstrate a microtoroid with negative thermal broadening, a high Q microtoroid was first tested and its Q factor recorded ($Q_0 = 1 \times 10^7$). Then, a drop of 4% PMMA polymer was applied to the microtoroid, and the microtoroid was spun at 2,000 rpm for 30 seconds, resulting in a 0.4 μm thick PMMA coating on the toroid. The silicon chip, on which the silica toroid resides, was baked at 170°C for 10 minutes to cure the polymer. Finally, the thermal broadening characteristics of the polymer coated toroid were measured using a tunable laser, and the final Q was measured to be 4×10^5, which is 25 times lower than the Q before coating. Figure 2.11 demonstrates that the cavity mode thermal coefficient is now slightly negative, since the thermal broadening occurs when the the laser wavelength is scanned downwards (left side). As the power stored in the microtoroid resonator increases, the resonance wavelength blue-shifts to lower wavelengths. With this novel microcavity, a pump laser can be stabilized on the red-shifted side of the cavity mode, which in turn can cool the microtoroid mode.

Following the author's work, a colleague showed a similar effect for a microtoroid coated with PDMS. The final Q factor (1.5×10^6) is higher than for PMMA due to the lower absorption coefficient of PDMS ($\alpha = 4\,\mathrm{m}^{-1}$) [51]. However, any polymer coating will reduce the Q of the microtoroid since its loss cannot match that of silica, possibly limiting the application of this technique. Future experiments can study the use of other thin film materials (e.g., Cytop, $\alpha = 0.2\,\mathrm{m}^{-1}$) with lower absorption loss [50].

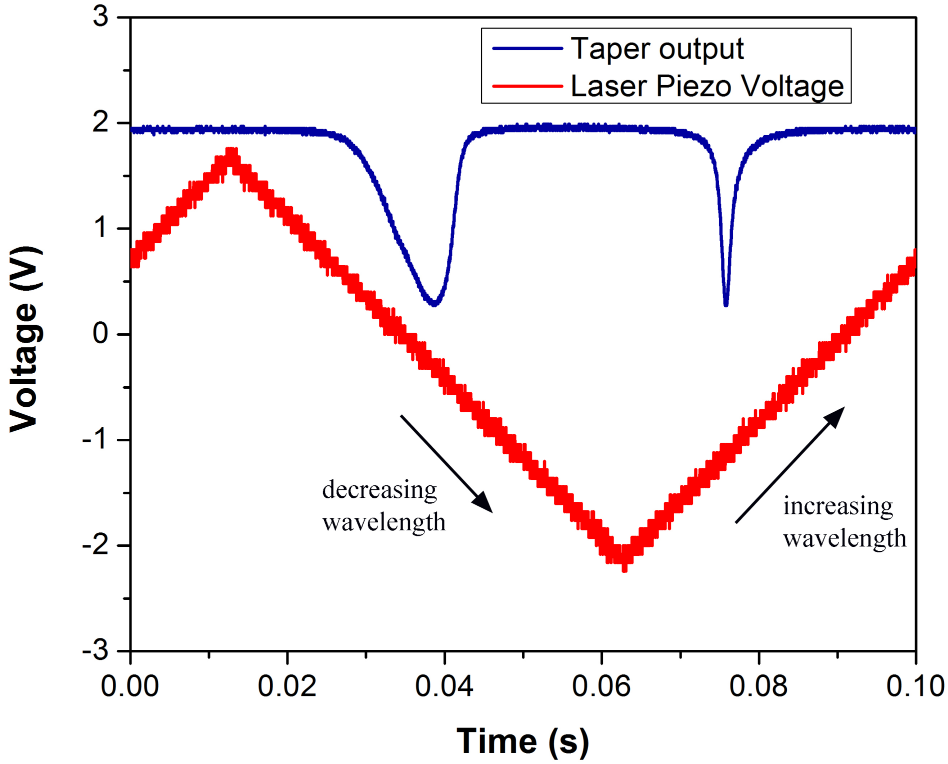

Figure 2.11. Plot of the taper transmission in time (shown in blue) and the laser piezo voltage (shown in red) when critically coupled to a microtoroid exhibiting inverse thermal broadening due to the cavity mode's effective $-\delta n/\delta T$. The normal Lorenzian resonance broadens in time when the laser wavelength is swept downwards in time−negative slope for laser piezo, and the resonance narrows when the laser wavelength is decreased in time−positive slope for laser piezo.

2.4 Summary

In this chapter, the ultra-high Q microtoroid resonator was discussed. Microtoroid's have extremely low cavity loss and ultra-small mode volumes, making them unique resonators with applications in low-threshold lasers and nonlinear optics to name just a few. The whispering-gallery mode structure of microtoroids was analyzed with a finite element model. The evanescent field component of WGMs is an important element of the work presented in this thesis, and enables long duration and efficient interaction of optical radiation with different environments.

Also, the fabrication process for creating optical microtoroids was discussed. Microtoroids can be made quickly and inexpensively on silicon. The selective laser reflow of microdisks into microtoroids endows them with ultra high quality factors. The experimental testing of microtoroids was described, including fiber taper coupling. Finally, the thermal broadening effect in silica microtoroids was investigated. The author coated microtoroids with a polymer to change the sign of the thermo-optical coefficient, which made stable coupling on the red-shifted side of cavity resonance possible.

Chapter 3

Ultralow-threshold ytterbium-doped glass laser fabricated by the solgel process

3.1 Introduction

Rare-earth ions (e.g., Er^{3+}, Nd^{3+}, Yb^{3+}, Ho^{3+}) are popular dopants for solid-state lasers due to their high efficiencies, long upper-level lifetimes, ability to generate short pulses, and straightforward incorporation into host materials including glasses and crystals [52]. In addition, the rare-earth aggregate emission spectrum spans many key wavelengths from 0.3 to 3 μm that are important for imaging, sensing, medical treatment, and communications. While rare-earth lasers have been built in large form factors for high-power laser cutting and defense applications, they can also be designed to be small, low power, and ultrasensitive to the environment. The laser resonator finesse, defined as the free spectral range (FSR) divided by the resonance linewidth, quantifies the loss and hence energy storage efficiency of a resonator. For a given cavity, higher finesse results in lower threshold for lasing. Lacovara measured a 71 mW threshold for a Yb^{3+}:YAG microchip laser with a cavity finesse of 57 [53]. Asseh demonstrated 230 μW threshold for a $Yb^{3+}:SiO_2$ fiber laser with a finesse of 630 [54]. Recently, the ultra high Q ($> 10^8$) toroid whispering-gallery resonator was invented [10]. The extremely low loss of this device enabled significant reduction of the threshold for an Er-doped silica solgel laser [20]. The Yb-doped silica toroid microcavity laser reported here has an on resonance finesse greater than 10,000.

The Yb-doped silica gain medium of this microlaser is fabricated on a silicon chip according to the solgel chemical synthesis method. The solgel technique for making thin films is attractive because it is low cost, fast, and extremely flexible [55]. Indeed, solgel techniques have been used to make optical couplers, Er^{3+}–Yb^{3+}-doped waveguide amplifiers, and even silica nanotubes [56, 57, 58]. A $Yb^{3+},Al^{3+}:SiO_2$ solgel fiber laser achieved a threshold of 80 mW launched power [59]. The author has developed a fiber-coupled Yb-doped silica solgel microtoroid laser with 1.8 μW threshold, which is believed to be the lowest threshold to date for any ytterbium-doped laser.

3.2 Solgel fabrication of silica thin-films

The laser's ytterbium-doped silica gain material is fabricated according to the well-known solgel technique. Solgel is a flexible and cost effective wet-chemistry synthesis method commonly utilized for preparation of glasses and ceramics. The applications of solgel materials are diverse, covering optics, electronics, chemistry, and biology. For instance, a novel field-effect transistor (FET) was recently reported with a zinc oxide (ZnO) thin film fabricated by the solgel technique [60]. The foundation for solgel fabrication was laid in the 1800s by Ebelman and Graham, who discovered that it was possible to synthesize silicon dioxide (silica) in gel form by hydrolysis of tetraethyl orthosilicate (TEOS) in an acidic environment [55]. This basic solgel technique, including TEOS and an acidic catalyst, survives today and forms the framework of the author's solgel fabrication of silica thin films for rare-earth doped microtoroid lasers. Research into practical applications for solgel fabricated glasses and ceramics exploded in the 1990s [55, 61]. A previous graduate student in the Vahala group, Lan Yang, developed solgel fabrication of erbium-doped silica thin films at Caltech. Lan demonstrated novel erbium-doped silica microsphere and microtoroid lasers [62, 63, 20].

Solgel fabrication of amorphous silica (SiO_2) can be divided into three main parts: hydrolysis to produce a colloidal suspension (sol), water condensation into a liquid phase gel, and high temperature annealing to form dense glass. Here, the general method of solgel fabrication of silica thin films will be discussed. Specific fabrication details will be given later in the chapter.

Simply put, the goal of solgel fabrication of silica is to create a dense and uniform network of silicon and oxygen atoms in a precise stoichiometric ratio ($\ldots - \mathrm{Si} - \mathrm{O} - \mathrm{Si} - \mathrm{O} - \ldots$). Of course, this silica network must be free of contaminants like water or $-\mathrm{OH}$ bonds, solvents, or organics in order for the final silica material to exhibit ultra-low loss in the infrared. A co-solvent, such as methanol or isopropanol, is included during the chemical reaction to allow thorough mixing of TEOS and water, which are normally immiscible.

3.2.1 Sol synthesis by hydrolysis

TEOS, with chemical formula $Si(OC_2H_5)_4$, is the metal alkoxide precursor for the solgel reaction. An alkoxide (represented as $-\mathrm{OR}$) consists of an organic group (i.e., C_2H_5) bound to an oxygen atom, and is very reactive in the presence of proton donor molecules like water. The first fabrication step is hydrolysis, in which alkoxide groups ($-\mathrm{OR}$) of TEOS are replaced by hydroxyl groups ($-\mathrm{OH}$) as shown in Equation (3.1).

$$\mathrm{Si} - \mathrm{OR} + \mathrm{H} - \mathrm{O} - \mathrm{H} \longrightarrow \mathrm{Si} - \mathrm{OH} + \mathrm{R} - \mathrm{OH} \tag{3.1}$$

The acidic catalyst (HCl) for the hydrolysis reaction adds protons (H^+) to the alkoxide groups, and makes them more reactive with water. The mixture of alkoxide gel precursors ($\mathrm{Si}-\mathrm{OH}$ molecules) is named the colloidal solution (sol).

3.2.2 Gel synthesis by condensation

Next, the alkoxide gel precursors undergo a polymerization reaction with the acid catalyst. This reaction produces cross-linked polymer chains of silicon and oxygen, which are the foundation of the silica network, and also causes water condensation as shown in Equation (3.2). Two hydrolyzed Si-OH molecules are linked together in the condensation reaction to form a siloxane (Si−O−Si) bond.

$$\mathrm{Si-OH+Si-OH \longrightarrow -Si-O-Si-+H-OH} \tag{3.2}$$

During condensation, the sol particles form a continuous liquid phase (gel) of silicon and oxygen chains surrounded by water, organics, and co-solvent. Moderate heating, at less than 100°C to prevent evaporation of water, is commonly used to speed up the hydrolysis and condensation reactions.

The next important step for solgel fabrication is drying. Water and solvent are removed from the interconnected pores of the gel, and the polymer chain aggregation increases as the gel is dried at room temperature. If the solvent and water cannot evaporate easily, microcracks form as non-uniform gel shrinkage builds up stress. Cracking is normally found only in larger solgel bulk material (1 mm or larger) and can be eliminated through careful control of the solgel chemistry.

3.2.3 Glass densification by heat treatment

The dry gel with silica pores is then subjected to a high temperature heat treatment in the final solgel fabrication step, normally at 1,000°C or higher for silica. During high temperature annealing, any remaining organics are forced out of the silica gel, additional polycondensation occurs, the pores disappear, and the silica network is densified. After the heat treatment is complete, the density of a well fabricated solgel silica glass is equal to fused silica. Yang measured the Fourier Transform Infrared (FTIR) spectrum of a silica solgel thin film after high temperature annealing, and showed that it closely matches the spectrum of wet-deposition thermal oxide [20]. Another method for verifying the quality of silica is by measuring the buffered-oxide etching (BOE) speed. The author measured that the ytterbium-doped silica solgel thin film (1.5 μm thick) has an etch rate of 13 Å/s, identical to fused silica, which confirms the correct density of solgel silica.

3.3 Ytterbium activated silica for laser gain

If properly excited by pump radiation, ytterbium ions can provide laser gain by stimulated emission in host materials like silicate glass or yttrium aluminum garnate (YAG) crystal. For solgel fabrication of glass thin films, silica can be doped with ytterbium by adding ytterbium nitrate, $Yb(NO_3)_3$, to the initial solution. In this way, silica can be doped with virtually any rare-earth ion, showing the great flexibility of solgel fabrication.

The first ytterbium-doped silica laser on record was demonstrated in 1962 by Etzel [64]. The ytterbium laser cavity can be a fiber, microchip, or microtoroid like the laser presented here [53, 54, 19].

3.3.1 Electronic structure of ytterbium

One of the most attractive features of ytterbium for laser action is its simple electronic structure, consisting of only the ground manifold ($F^2_{7/2}$) and excited manifold ($F^2_{5/2}$) [65]. As shown in Figure 3.1, the ground manifold has four Stark levels and the excited manifold has three Stark levels. The Stark levels are formed by splitting of the spectral lines of the ytterbium atoms by the silica network's electric field.

The large energy gap between the ground and excited manifolds prevents non-radiative decay, increasing the laser's upper-level lifetime (τ_{Yb}). Also, no laser up-conversion is expected for ytterbium silica due to the lack of higher electronic states [65]. Erbium doping cannot exceed 1%, or else deleterious concentration-quenching will reduce the laser efficiency. Ytterbium does not suffer from this effect and can be doped to much higher concentrations, even exceeding 20%.

3.3.2 Ytterbium laser characteristics

Ytterbium has a broad absorption line centered on 920 nm, and a narrow absorption peak near 970 nm with higher cross section of absorption. All of the ytterbium lasers discussed in this thesis are optically pumped on the 970 nm line, which has a 10 nm full-width at half-maximum (FWHM) absorption peak. Ytterbium can have higher pump efficiency than erbium because ytterbium's cross section of absorption ($\sigma_{a,Yb}(975\text{nm}) = 2.5 \times 10^{-24}\text{m}^2$) is larger than erbium ($\sigma_{a,Er}(1460\text{nm}) = 2 \times 10^{-25}\text{m}^2$). Figure 3.2 is a plot of the cross sections of absorption and emission versus wavelength for Yb:SiO_2. Ytterbium has a large emission cross section from $1010-1050$ nm, with emission being observed even as high as 1200 nm. Ytterbium-doped tunable lasers take advantage of this large emission bandwidth [66].

In this thesis, the ytterbium-doped silica lasers are pumped at 970 nm and laser emission is generated around 1040 nm. The small quantum defect, $(\lambda_{laser} - \lambda_{pump})/\lambda_{pump} = 7\,\%$, is an important advantage for ytterbium because the laser cavity generates significantly less heat than a correspond-

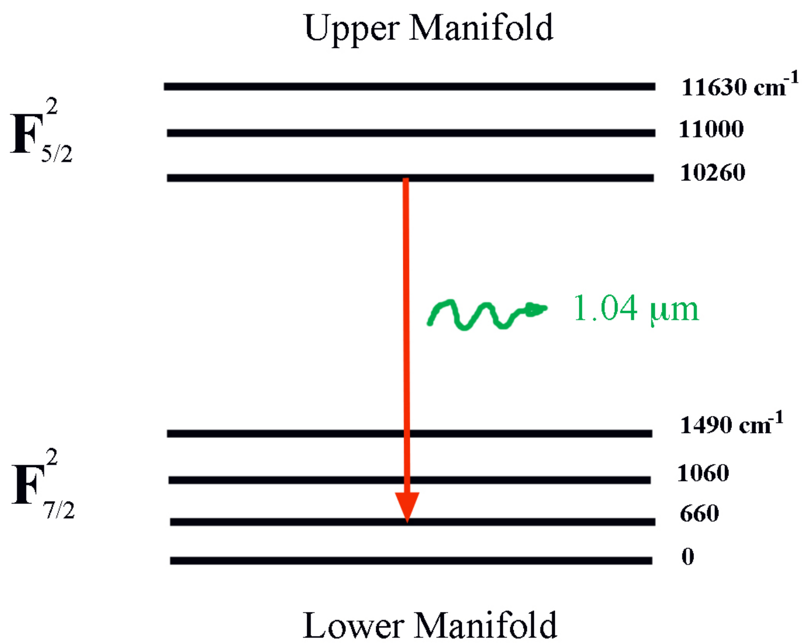

Figure 3.1. Energy level diagram for Yb^{3+}, showing the ground manifold ($F^2_{7/2}$, four Stark levels) and excited manifold ($F^2_{5/2}$, three Stark levels). The energy in wavenumbers (cm^{-1}) of each level is shown. Also, one of the primary laser transitions ($\lambda = 1.04\,\mu$m) is marked with a red arrow.

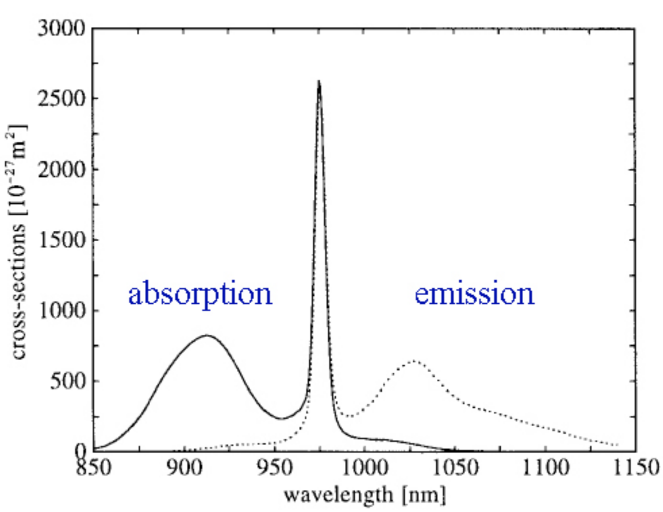

Figure 3.2. Absorption and emission cross-sections of $Yb^{3+} : SiO_2$ reproduced from Paschotta et al. [67]. The microtoroid lasers are pumped at 970 nm, laser emission is normally at 1040 nm.

ing neodymium-doped laser. Low laser heating is important for high power lasers [68] and will also be beneficial for laser cooling applications. Ytterbium's pump and emission wavelengths are similar, allowing efficient fiber taper coupling of the pump and laser radiation using a single fiber taper.

To summarize, ytterbium is an attractive laser dopant because of its high cross section of absorption, low quantum defect, simple electronic structure, and high concentration doping capability. In addition, the 1 μm emission wavelength of ytterbium is very useful, as will be discussed in **Chapter 4**.

3.4 Yb:SiO_2 laser modeling

3.4.1 Laser model parameters

A laser model of the Yb:SiO_2 microtoroid was developed to determine the design parameters of the laser and anchor the experimental results. The author modified a microtoroid laser model, developed for erbium silica microlasers by Min [21], for the ytterbium silica microtoroid laser resonator. This model is based on a coupled-mode theory of a microtoroid resonator and fiber taper waveguide [69, 70, 13, 71].

Several constants must be included to properly model the laser dynamics. The cavity mode volume, V, is calculated as $V = (2\pi R_{toroid})(\pi r_{mode}^2)$. The coupling factor ($\kappa_{ext} = \sqrt{1/\tau_{ext}}$) is the amplitude coupling coefficient between the toroid and the taper's pump wave. The extrinsic microtoroid cavity lifetime ($\tau_{ext} = Q_{ext}/2\pi f_s$) is influenced by the coupling between the taper and toroid, in addition to intrinsic cavity loss factors. Next, define several parameters that model the gain properties of the laser (also known as Giles parameters).

$$\begin{aligned} \alpha_p &= \Gamma N_T \sigma_p^a \ , \ \alpha_s = \Gamma N_T \sigma_s^a \\ g_p^* &= \Gamma N_T \sigma_p^e \ , \ g_s^* = \Gamma N_T \sigma_s^e \end{aligned} \tag{3.3}$$

The overlap factor, Γ, represents the physical overlap of the cavity pump and signal modes inside the microtoroid. The near ideal phase matching between the microtoroid mode and taper mode, and the small cavity mode volume are expected to give an overlap factor approaching unity. The similar pump and signal wavelengths ($\lambda_p = 970$ nm, $\lambda_s = 1040$ nm) of ytterbium also contribute to the large overlap factor. Therefore, $\Gamma = 1$ will be assumed for the ytterbium laser modeling. The ytterbium concentration, N_T, has been modeled within the range of 2×10^{18} to 1×10^{20}. Ytterbium's pump and signal absorption and emission are given by σ, whose values can be found in literature [67]. The cross section values used for simulations in this research are given in Table 3.1.

$\sigma_p^a = 2.7 \times 10^{-24}$ m^2	$\sigma_s^a = 1.0 \times 10^{-26}$ m^2
$\sigma_p^e = 2.7 \times 10^{-24}$ m^2	$\sigma_s^e = 5.0 \times 10^{-25}$ m^2

Table 3.1. Pump and signal cross sections of absorption and emission for Yb:SiO_2

Also, passive cavity loss terms are defined at both pump and signal wavelengths as

$$\alpha_{p,passive} = 2\pi \frac{n_p}{\lambda_p Q_{passive}} \;\; , \;\; \alpha_{s,passive} = 2\pi \frac{n_s}{\lambda_s Q_{passive}} \tag{3.4}$$

where $Q_{passive}$ is the loaded quality factor ignoring the absorption due to ytterbium ions. The room-temperature refractive indices of silica at the pump and signal wavelengths are given by n_p and n_s. The long laser upper-level lifetime of ytterbium silica ($\tau_{Yb} = 0.7$ ms), while not as large as erbium's (10 ms), enables high laser efficiency as already demonstrated in a fiber laser [72]. To account for the absorption by ytterbium ions, an appropriate absorption coefficient is defined as $\alpha_{yb} = \frac{n_s}{c\tau_{yb}}$.

3.4.2 Laser pump threshold

After applying coupled-mode theory to the microtoroid and taper system, the ytterbium microtoroid laser's threshold power for laser operation can be derived [21].

$$\begin{aligned} P_{th} =& N_t h\nu V \left(\frac{f_s n_s}{f_p n_p}\right)\left(\frac{c^2}{4n_p^2\kappa_p^2}\right) \\ &\times \frac{\left[(\alpha_p + \alpha_p^{passive})(\alpha_s + g_s^*) - (\alpha_p + g_p^*)(\alpha_s + \alpha_s^{passive})\right]^2}{(\alpha_s + g_s^*)^2} \\ &\times \frac{\alpha_{Yb}(\alpha_s + \alpha_s^{passive})}{\alpha_p(\alpha_s + g_s^*) - (\alpha_p + g_p^*)(\alpha_s + \alpha_s^{passive})} \end{aligned} \tag{3.5}$$

P_{th} is the absorbed pump power at which the round-trip laser gain is equal to the round-trip loss, and pump powers above threshold will generate laser emission. In addition to threshold, the laser output power and efficiency can be easily calculated [21]. Microtoroid lasers doped with erbium or ytterbium normally have threshold pump powers on order of 10 μW, record values for rare-earth doped lasers. Low thresholds are made possible by small cavity diameters, low doping levels (of order 0.1% or less) and efficient taper fiber coupling.

3.4.3 Laser model results

The author used the laser model described above to determine an optimum doping concentration and toroid diameter for laser experiments. The ytterbium concentration was adjusted to minimize the pump threshold, and made possible development of a record-low threshold ytterbium laser. The laser threshold dependence on doping concentration is shown in Figure 3.3. The lower panel highlights the low concentration behavior, which shows a rapid increase in pump threshold as the concentration is reduced. Lasing is not predicted for ytterbium concentrations less than 2.9×10^{18} cm^{-3}. There is a local minimum for laser threshold at $N_T = 3 \times 10^{18}$ cm^{-3}, around which the threshold increases. At lower concentrations, the threshold increases because the ytterbium ions must be pumped at a higher rate to overcome the intrinsic loss of the cavity and taper system. For concentrations higher than the optimum, the threshold increases since the additional ions must be pumped to transparency. Ytterbium is a quasi-three level laser, meaning it has ground state absorption due to room-temperature occupation of the lowest energy level.

As part of the ytterbium laser design exercise, the threshold dependence on major diameter was modeled. Figure 3.4 shows the linear relationship between laser threshold and toroid diameter for a ytterbium doping concentration of $N_T = 8 \times 10^{18}$ cm^{-3}. Smaller mode volume requires less pump power to reach the gain necessary for laser output. Based on the results of threshold simulations for dependence on toroid size and doping concentration, a suitable solgel fabrication produced microtoroids with record low threshold. For that laser, to be discussed in later sections, the toroid diameter (D) is 43 μm, and the doping concentration (N_T) is 4×10^{18} cm^{-3}.

The dependence of quality factor on ytterbium concentration shows the influence of the laser ions on cavity loss. At the pump wavelength (near 970 nm), the Q of the ytterbium doped microtoroid cavity is low due to the necessary pump absorption. Far away from the ytterbium absorption lines, at 1550 nm for example, the cavity Q is as high as the Q of undoped solgel silica microtoroids ($Q = 2.5 \times 10^7$), indicating that the scattering loss of the ytterbium ions is negligible. The on-resonance Q depends inversely on the doping concentration as shown in Figure 3.5. In this figure, both the model predictions shown in red, and the actual experimental Q agree well. As expected, higher Yb concentration gives lower Q due to the useful laser ion absorption.

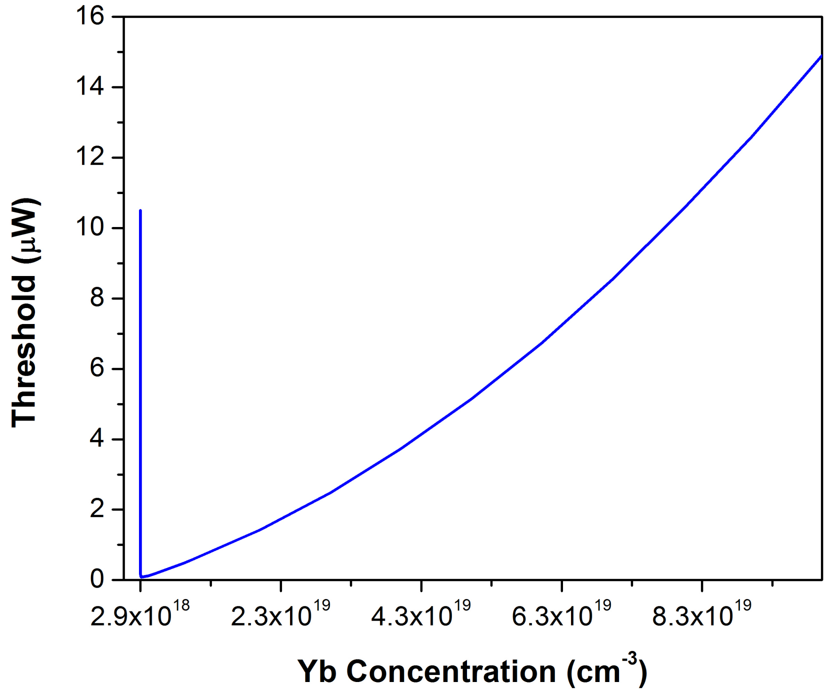

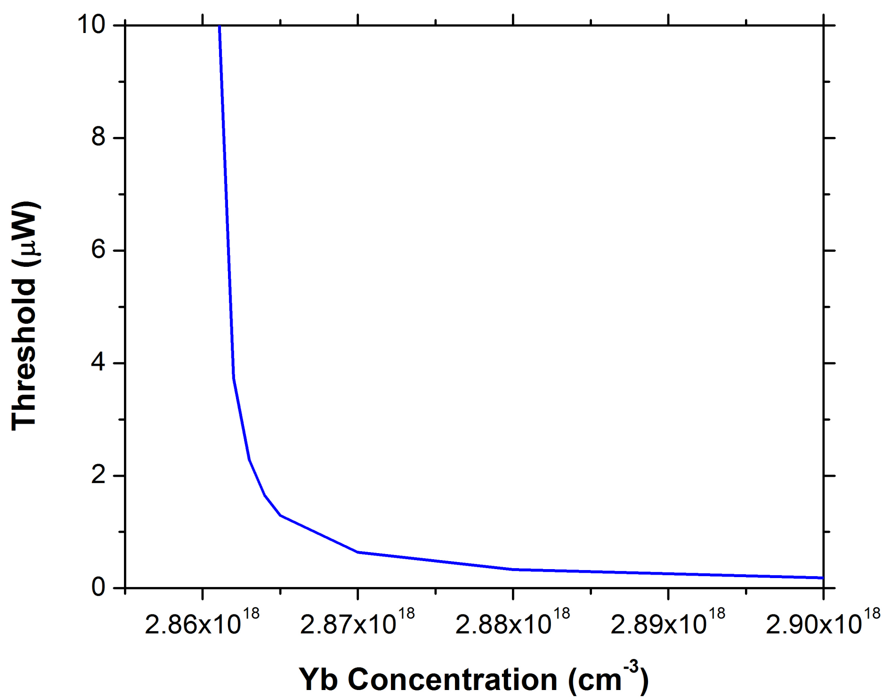

Figure 3.3. Plot of model predictions of Yb:SiO_2 laser threshold as a function of ytterbium concentration (N_T) for a $D = 43$ μm microtoroid. The lower panel shows more detail at low concentrations, where the laser threshold increases rapidly.

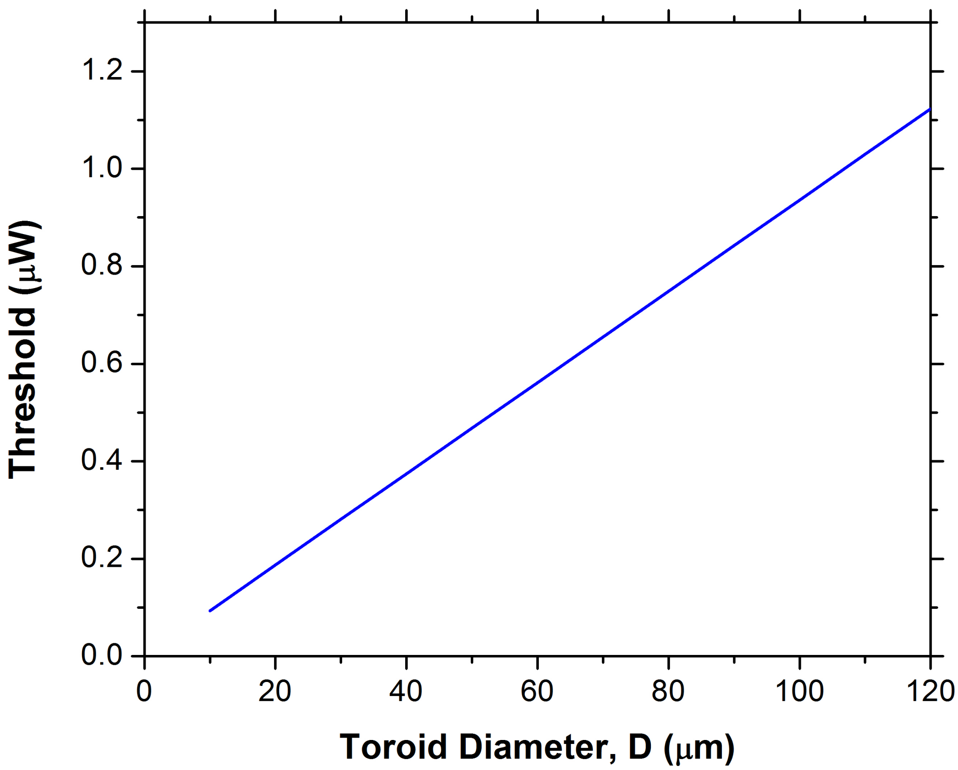

Figure 3.4. Plot of $Yb{:}SiO_2$ laser threshold as a function of toroid major diameter (D) for $N_T = 1 \times 10^{19}$ cm^{-3}

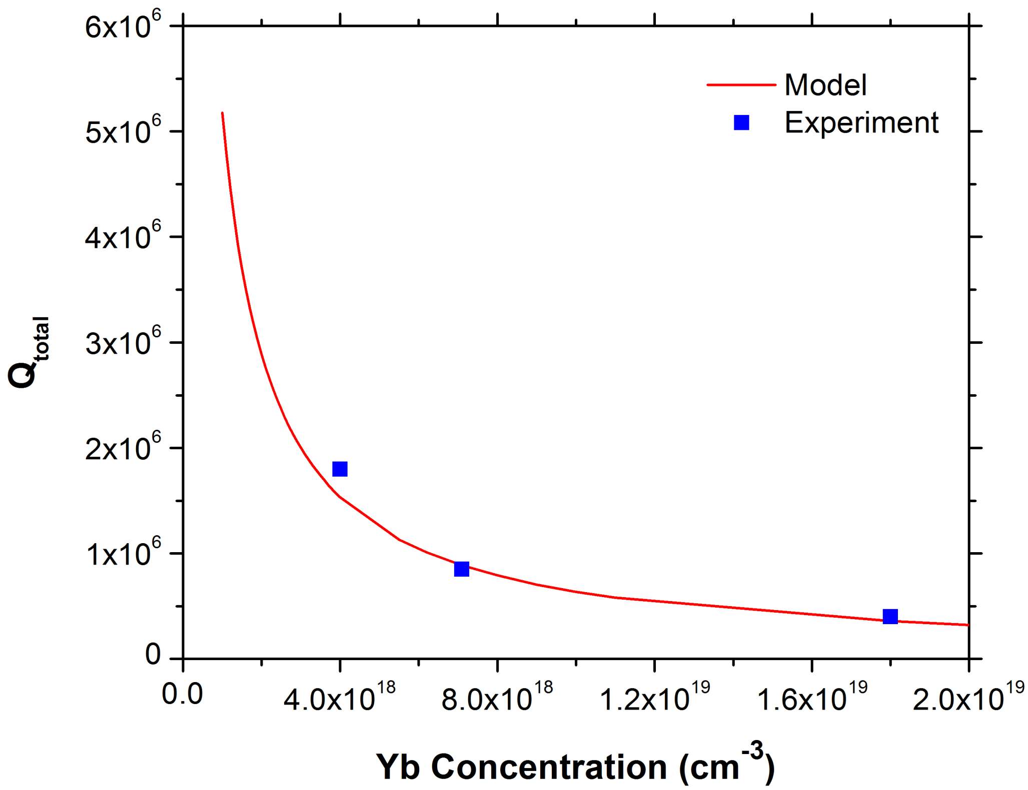

Figure 3.5. Yb:SiO_2 laser Q at the pump resonance as a function of the Yb concentration – the model prediction (red line) and experimental results (blue points) agree well. The Q decreases with Yb concentration as expected.

3.5 Yb:SiO_2 laser fabrication

3.5.1 Silica thin film preparation by the solgel method

Fabrication of the laser microcavity begins with solgel synthesis of the Yb-doped silica thin film, and closely follows the general solgel fabrication given in Section 3.2. First, tetraethoxysilane (TEOS) is hydrolyzed with a molar ratio of water to TEOS between 1:1 and 2:1. Isopropanol is the co-solvent and hydrochloric acid the catalyst. After the alkoxide groups in TEOS are replaced with hydroxyl groups, the remaining hydrogen atoms are removed through a condensation reaction. Finally, Yb nitrate is introduced to produce the desired Yb^{3+} concentration in the silica thin film. The entire mixture is stirred on a hot plate at 70°C for 3 h to produce the solgel liquid. The general solgel recipe including the quantity of each specific chemical is given in Table 3.2. While this recipe will produce undoped silica, rare-earth ions, like Yb^{3+} in the form of ytterbium nitrate, can be added. Since ytterbium nitrate is normally dissolved in water, the solgel engineer must adjust the added water so the total water mass is 1.4 g. After the heat-assisted chemical reaction, the Yb-doped silica solgel is deposited in three layers onto a silicon substrate by spin coating. Immediately after each layer is deposited, the thin film is annealed at 1,000°C in normal atmosphere for 3 h to remove the solvent, undesired organics, and hydroxyl groups in the solgel network [73, 74]. During solgel fabrication, only fresh chemicals (especially TEOS) clean glassware should be used in order to produce a high-quality silica solgel free of cracking.

Chemical Name	Formula	Mass (g)
Water	H_2O	1.40
Isopropyl Alcohol	C_3H_7OH	11.00
Hydrochloric Acid	HCl	1.10
Tetraethylorthosilicate	$SiC_8H_{20}O_4$	12.45

Table 3.2. solgel recipe for pure silica. Dopants like ytterbium nitrate can be included, and any water added for dilution should be included in the total water mass.

3.5.2 Microtoroid fabrication

After the solgel silica thin film is complete, the glass film is patterned by standard lithography and isolated silica disks are defined on the silicon substrate using a buffered oxide wet etch. The disks are then optically isolated from the underlying silicon using XeF_2 to selectively etch silicon, leaving Yb^{3+}:SiO_2 disks supported by silicon pillars. In the final step, a CO_2 laser (10.6 μm) symmetrically reflows the silica microdisk to form a smooth microtoroid with a 40 μm principal diameter. Surface tension during melting defines the toroid shape and increases the cavity quality factor by significantly reducing surface roughness.

3.6 Laser testing

3.6.1 Experimental setup

A single submicrometer diameter fiber taper, which is phase matched to the microcavity's whispering gallery spatial mode, couples light into and out of the microtoroid at the equatorial plane as shown in Figure 3.6 [13, 8]. The coupling parameter, which determines the cavity loading and consequently the laser performance, is precisely adjusted by moving the silica cavity with respect to the fiber taper using a three-axis nano-positioning system.

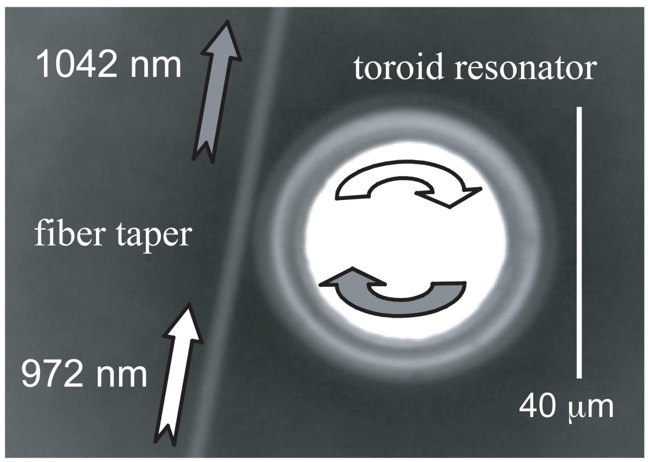

Figure 3.6. Top-view photograph of testing setup showing evanescent coupling of fiber taper to Yb^{3+}:SiO_2 microtoroid laser

A tunable, single-frequency, narrow linewidth 300 kHz semiconductor diode laser provides pump light in the 970 nm absorption band of Yb. At the fiber output, Yb^{3+}:SiO_2 laser emission at 1042 nm and unabsorbed pump light at 972 nm are separated by a fiber-coupled WDM filter with 45 dB isolation. The coupling and laser output are monitored with an optical detector, power meter, and spectrum analyzer (0.07 nm resolution). The intrinsic microcavity quality factor is calculated by measuring the resonance linewidth in the undercoupled regime. At the pump wavelength of 972 nm, the Q is 1×10^6 due to resonant absorption by the ytterbium ions. The cavity Q at 1550 nm, well removed from the Yb absorption band, is 25×10^6 and reflects the low scattering loss of the cavity.

3.6.2 Ytterbium concentration

Since the average pump photon makes 1,000 round trips in the cavity, this Yb-doped glass laser achieves efficient pump absorption even though the Yb concentration is just 0.01%. High pump

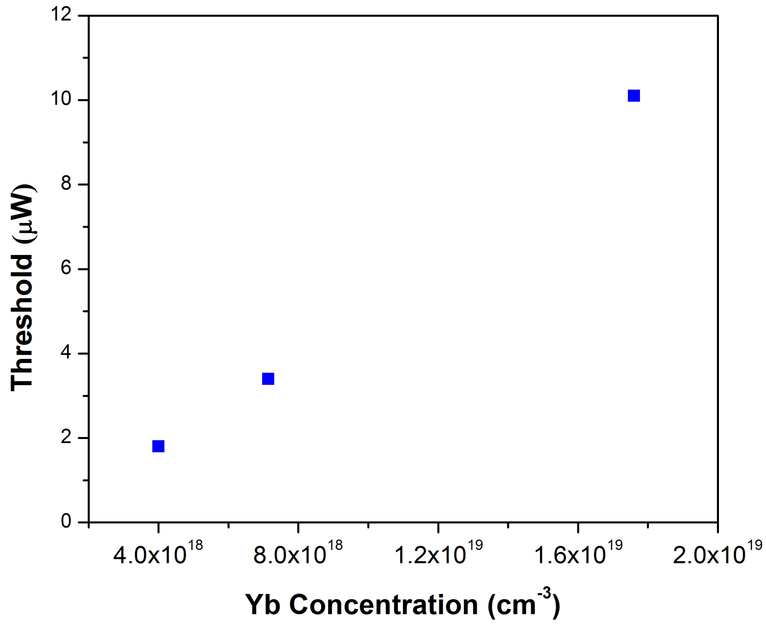

Figure 3.7. Measured laser threshold (absorbed power) as a function of Yb^{3+} concentration for Yb-doped silica microcavity

absorption, short cavity length, and low doping concentration are necessary for low lasing threshold [21]. The doping concentration must be high enough to provide sufficient gain to overcome material and cavity losses. As such, no lasing was observed for Yb concentrations as low as 1×10^8 cm^{-3} given the available pump power. But for concentrations greater than at least 4×10^8 cm^{-3}, the pump threshold was measured to increase with concentration as shown in Figure 3.7. The additional pump power is needed to compensate for the loss from unpumped Yb^{3+} ions because the ground state of Yb is well populated at room temperature.

3.6.3 Laser results

A record low 1.8 μW threshold of absorbed power was demonstrated for a 40 μm diameter silica microtoroid laser with 4×10^8 cm^{-3} Yb^{3+} concentration. To the best of the author's knowledge, this is the lowest published threshold to date for any Yb-doped laser. The laser output power depends linearly on the absorbed pump power (above threshold) as shown in Figure 3.8. The coupler, filter, and taper losses are accounted for in these results. Microtoroids support both clockwise and counterclockwise modes that are coupled by surface scattering [75]. But, only the single-end laser power from the clockwise mode is measured, discarding approximately half of the laser output power. While the laser slope efficiency with respect to absorbed power for the lowest threshold laser is 3%, slope efficiencies as high as 18% were recorded, as shown in Figure 3.8. The highest output power is 12 μW.

Continuous wave (cw) multimode lasing was demonstrated over a 40 nm span for certain taper to cavity couplings conditions, due to the broad emission bandwidth of Yb. But, with proper alignment, single frequency cw laser output is attainable (see the laser spectrum shown in Figure 3.9). The microtoroid laser cavity FSR is 6 nm.

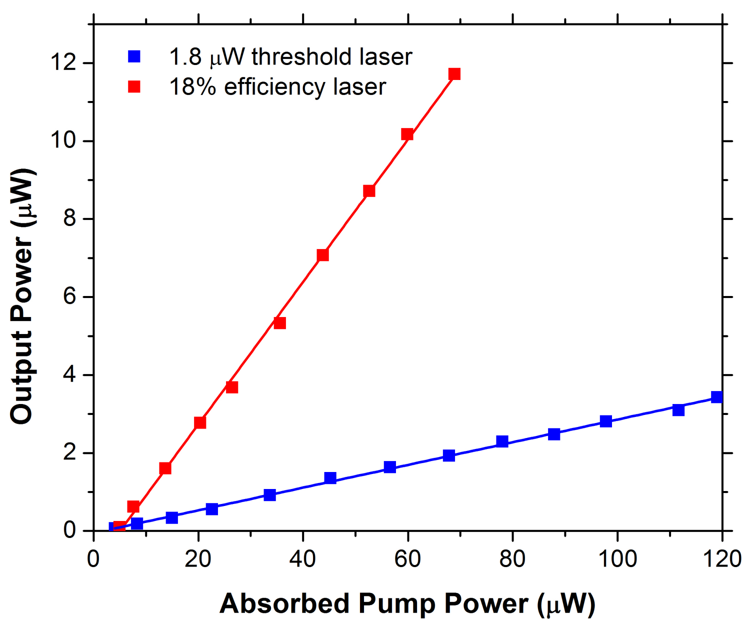

Figure 3.8. Measured laser output power as a function of absorbed pump power for two 40 μm diameter Yb^{3+}:SiO_2 microtoroid lasers. One toroid laser was overcoupled to the taper waveguide and achieved high efficiency (shown in red), the other shows low pump threshold for a slightly undercoupled taper condition (shown in blue)

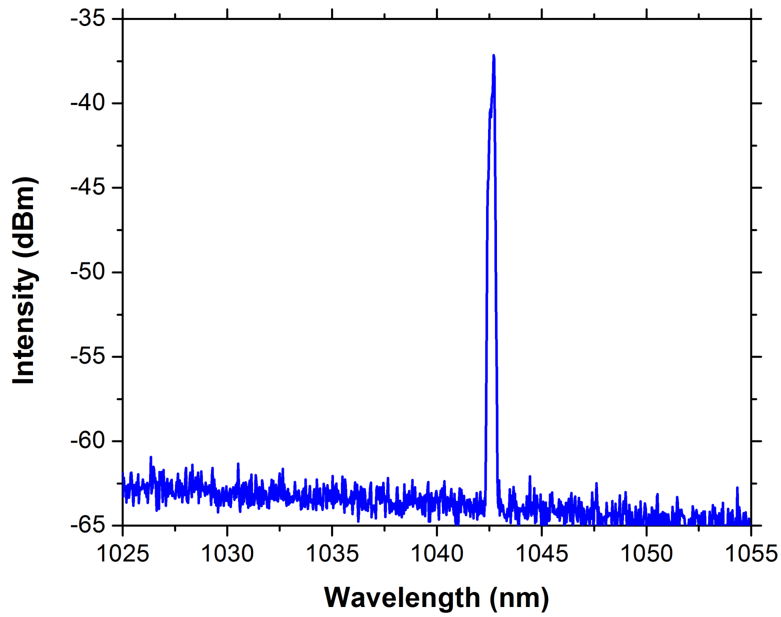

Figure 3.9. Measured laser output spectra of single-frequency Yb^{3+}:SiO_2 microtoroid laser

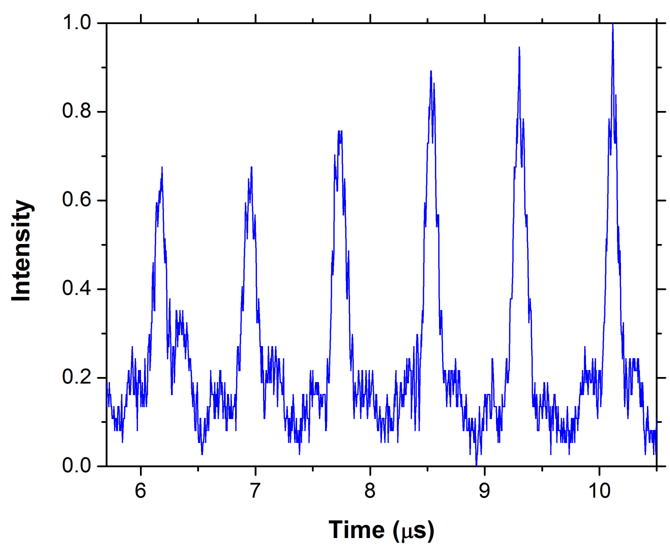

Figure 3.10. Plot of toroid laser output exhibiting 1 Mhz and 200 ns duration pulses caused by saturable absorption of unpumped Yb^{3+} ions

3.6.4 Saturable absorption induced laser pulsing

During testing, several other Yb:SiO_2 lasers exhibited pulsations in the laser output power similar to those found in an Er:SiO_2 microtoroid laser [20]. Pulsing is most easily observed for higher doping concentration (typically 2×10^{19} cm^{-3}). Laser pulsing with 1 MHz repetition rate and 100 ns duration is presented in Figure 3.10. The origin and behavior of pulsations in Yb-doped silica microlasers is believed to be associated with saturable absorption caused by Yb ions adjacent to the laser mode that are not completed excited [62].

3.7 Summary

In conclusion, the author has demonstrated a single frequency on-chip Yb-doped silica laser fabricated by the solgel process. The pump threshold is as low as 1.8 μW, which is more than 100 times less than the lowest published threshold to date for a Yb-doped laser [54]. The slope efficiency is as high as 18%. This Yb^{3+}:SiO_2 laser will operate more efficiently in a water environment compared with a 1.55 μm laser, since the absorption coefficient of water is significantly less at 1.0 μm compared with 1.55 μm (0.16 and 12 cm^{-1}, respectively) [22]. As such, it could function as the laser for an active chemical or biological sensor using surface functionilized protocols readily available for silica. Also, the flexible solgel process and compatibility of the simple electronic structure of Yb with other rare-earth ions can be used in the future for dual-doped lasers such as Er^{3+},Yb^{3+}:SiO_2; a subnanosecond Q-switched Cr^{4+},Yb^{3+}:SiO_2 laser [76]; or upconversion lasers [77]. Applications for this low threshold and small footprint laser may be found in dense on-chip optical communications, active sensors, and rare-earth visible lasers.

Chapter 4

Yb-doped glass microcavity laser operation in water

4.1 Introduction

The previous chapter analyzed the performance of a Yb:SiO_2 microtoroid laser tested in normal air. The knowledge learned through those experiments, and the key 1 μm emission wavelength made it possible to build a microtoroid laser that operates efficiently in water. Whispering-gallery mode (WGM) microcavities feature an evanescent field component that extends into the surrounding medium [78]. Besides enabling a convenient way to couple optical power, the evanescent field provides a natural means by which resonant modes can interact with their environment. This latter feature is the basis of sensing techniques using passive whispering gallery microcavities [79, 80]. For example, heavy water (D_2O), has been detected through measurement of quality factor (Q), and interleukin-2 molecules have been detected by measuring a resonance shift [81, 18]. Theoretical studies have shown that an active microcavity can offer higher sensitivity [82]. As an example of one such device, Lu et al. recently demonstrated a biosensor utilizing the evanescent field component of a dye-doped distributed-feedback laser [83]. In this chapter, a Yb:SiO_2 microcavity laser that operates in water is presented. The work builds upon the ytterbium-doped silica microtoroid laser with record-low threshold operation in air [19]. To the best of the author's knowledge, laser action of a microcavity has not yet been demonstrated in water, and provides an important new feature for active biosensing applications.

4.2 Fabrication of microtoroid for laser in water

The microcavity used in this work is a silica toroid suspended on a silicon pillar and substrate [84]. These devices feature exceptionally high passive Q factors, making them well suited for laser applications when properly doped. In previous work, the sol-gel method has been used to dope the microcavity with erbium or ytterbium [19, 20]. Ytterbium is a more suitable rare-earth dopant than erbium for laser operation in water because the absorption coefficient of water is 0.16 cm^{-1} at 1.04

μm (Yb^{3+} emission) compared to 10 cm^{-1} at 1.55 μm (Er^{3+} emission) [22].

The ytterbium-doped silica gain medium is fabricated on a silicon chip according to the solgel chemical synthesis method detailed in **Chapter 3**. To briefly summarize, tetraethoxysilane, water, isopropyl alcohol, hydrochloric acid, and ytterbium nitrate are mixed in specific quantities at 70°C for three hours to produce the gel. The ytterbium concentration for the laser is 1.1×10^{19} cm^{-3}. Next, the ytterbium-doped solgel is deposited in three layers onto a silicon substrate by spin coating. After each layer is deposited, the thin film is annealed at 1,000°C in normal atmosphere for three hours. The refractive index of the Yb:SiO_2 film is 1.46, according to a spectroscopic ellipsometer measurement (Sentech SE850). Standard photolithography and a buffered oxide wet etch are used to create an array of glass disks with 180 μm diameter. These disks are optically isolated from the silicon substrate by a XeF_2 dry etch, leaving Yb^{3+}:SiO2 disks supported by silicon pillars. Finally, a CO_2 laser symmetrically reflows each silica microdisk into a smooth microtoroid with 120 μm principal diameter. This diameter is optimized for low resonator loss and pump threshold. The reduced index contrast of the toroid resonator in water (0.13) compared to air (0.46) increases both the minimum diameter required to avoid significant radiation loss, and also the fraction of power in the evanescent field [85]. A full vectorial finite-element simulation of the fundamental mode shows that the fraction of intensity located outside of the microtoroid increases from 0.6 to 3.6% when the toroid is immersed in water.

4.3 Laser testing in water

The Yb:SiO_2 microtoroid laser was characterized first in air and subsequently in water. A single sub-micron diameter fiber taper (Fibercore SMF980-5.8-12.5), phase matched to the microtoroid's whispering-gallery spatial mode, simultaneously injects pump light and retrieves lasing output as shown in Figure 4.1 [13, 8].

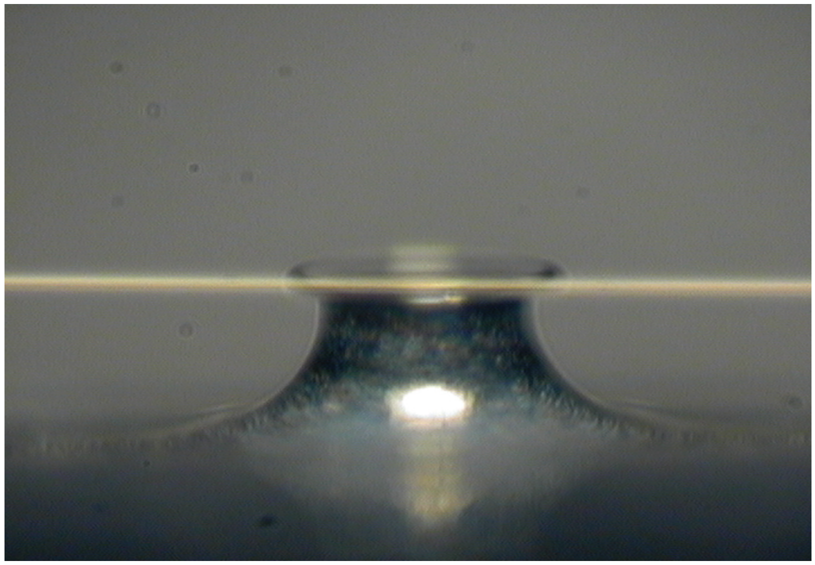

Figure 4.1. Image of testing setup showing evanescent coupling of fiber taper to 120 μm Yb^{3+}:SiO_2 microcavity (side view) in air.

FEM modeling demonstrates that the toroid mode index increases slightly in water compared to air, because the modes evanescent component increases and experiences the higher refractive index of water. It is possible to achieve a full range of coupling conditions in water from under- to over-coupled. The coupling gap increases in water for a given coupling condition, and is caused by spatial mode broadening of the fiber and toroid in water. The taper coupling to the microtoroid is controlled by a three-axis piezo nano-positioning system. A tunable, single-frequency, narrow linewidth (¡300 kHz) semiconductor diode laser provides pump excitation in the 970 nm absorption band of ytterbium. At the fiber output, Yb^{3+}:SiO_2 laser emission at 1040 nm is separated from unabsorbed pump light by a fiber-based WDM filter (45 dB isolation).

For testing in water, a glass cover slip is placed several millimeters above the silicon chip containing the toroid, and the air gap is filled with pure water to produce a temporary aquarium. A diagram of the water testing setup is shown in Figure 4.2. The fiber taper passes through a large water bubble, delivering pump light and extracting laser emission from the microtoroid. The viscosity of water decreases fluctuations in the taper to toroid gap, and creates a more stable coupling condition than in air. The fiber taper transmission is slightly less in water, due to both absorption in the water, and scattering losses incurred when the taper wave passes through the water/air interface. A larger aquarium would reduce the taper losses by placing the water/air interface at locations where the taper mode is more confined in glass fiber.

The quality factor of the microcavity pump resonance was measured to ascertain both the doping level as well as the impact of water absorption on the total microcavity Q. In air, the Q was measured to be 2.8×10^5 ($\lambda = 970.6$ nm). This Q factor is dominated by absorption of the Yb^{3+} ions. Q factors

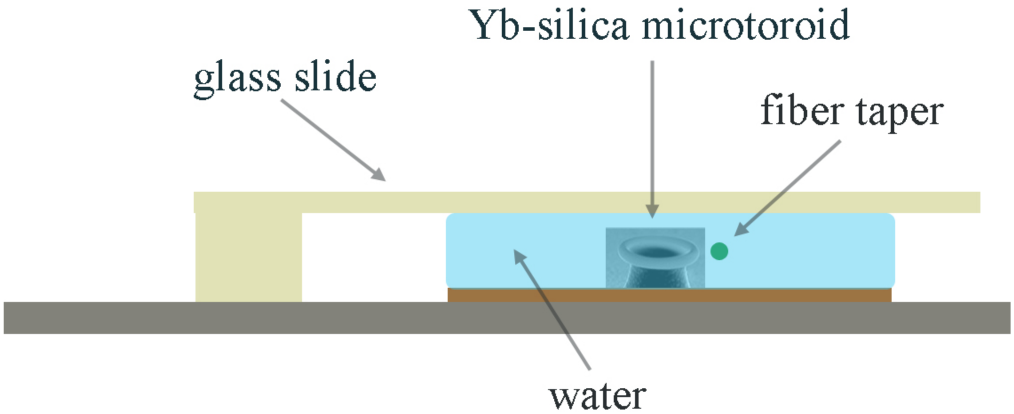

Figure 4.2. Diagram of the setup for testing in water (side view). The taper passes into the temporary aquarium, formed by injecting water in between a top glass slide on the silicon chip containing microtoroids. The toroid is completely surrounded by water.

for silica sol-gel microtoroids have been recorded as high as 2.5×10^7 million. To compare, thermal silica microtoroids routinely have Q factors greater than 1×10^8 [10]. Assuming the measured Q factor (2.8×10^5) is dominated by pump absorption, the doping level is estimated to be 1.1×10^{19} cm^{-3}, in good agreement with the value expected from fabrication (1.2×10^{19} cm^{-3}).

In water, the Q in the pump band is measured to be 1.3×10^5 ($\lambda = 970.8$ nm). Figure 4.3 shows the linewidth measurement of the pump resonance in water in the highly under-coupled regime, which gives the quality factor ($Q = \lambda/\Delta\lambda$). According to published values of the absorption coefficient of water at 970 nm ($\alpha = 45$ m^{-1}), the WGM loss in water should cause a reduction in measured Q to only 2.3×10^5 [22]. Therefore, there exists an additional source of absorption, such as external contaminants carried to the microtoroid by water. Experiments in water normally lasted up to 8 hours, and at the end of this time a decrease in Q factor was observed. The effect of water on solgel silica may be different than on thermally grown silica. Future research will investigate any difference, which could be due to porosity difference between thermal and solgel silica.

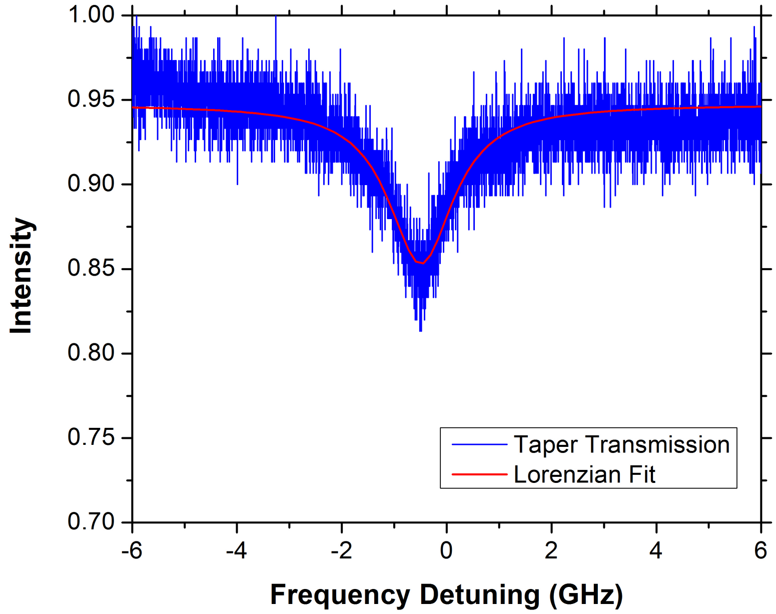

Figure 4.3. Plot of microtoroid pump-mode resonance in water with Lorenzian fit for the under-coupled condition ($Q = 1.3 \times 10^5$ at $\lambda = 970.8$ nm). Data is taken by measuring the transmitted power along the fiber taper while the pump laser wavelength is scanned in time.

The Yb:SiO_2 microtoroid laser output power was measured as a function of the absorbed pump power, for operation in air and water (see Figure 4.4). The microtoroid cavity supports both clockwise and counterclockwise modes, but only the power of the clockwise mode is recorded. Laser output in water was observed in more than ten microtoroids, illustrating the reproducibility of laser operation in water. The laser turn-on pump threshold is 3 μW in air and 15 μW in water, with corresponding slope efficiencies of 1.6% (air) and 0.5% (water). In water, there is a clear threshold for laser operation as well as a linear dependence of output power on absorbed pump power (see Figure 4.5). The maximum output power in water is 2 μW.

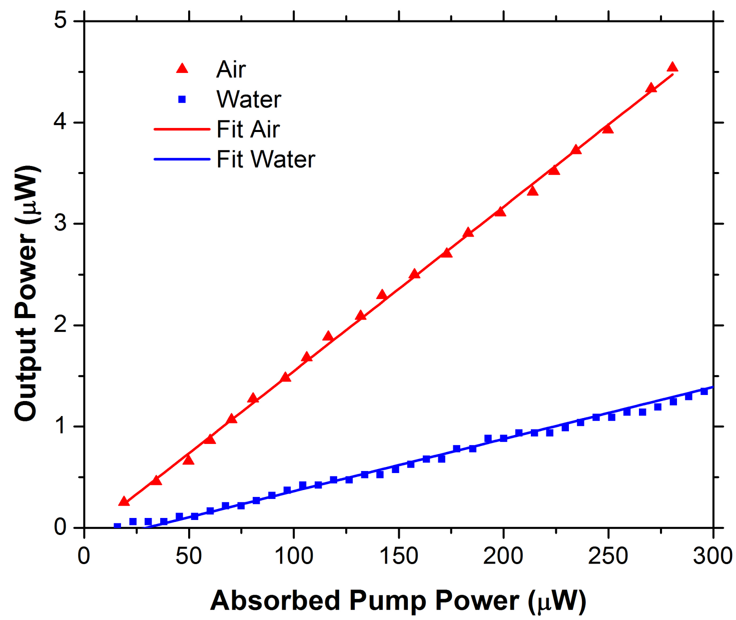

Figure 4.4. Comparison of measured laser output power as a function of absorbed pump power for 120 μm diameter Yb^{3+}:SiO_2 microtoroid in air and water

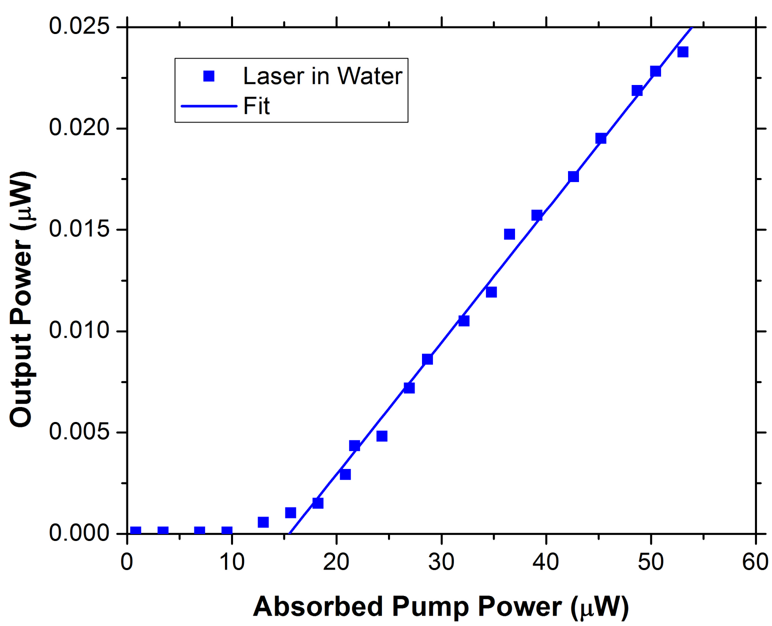

Figure 4.5. Plot of laser output in water at low pump powers showing the laser threshold

The predictions of the laser threshold model detailed in **Chapter 3** are compared with experiment [21]. The affect of the water was included in the model by decreasing the intrinsic quality factor to the actual value that was measured. In water (air), the experimental threshold, 15 μW (3 μW), is in reasonable agreement with the prediction of the model, 4 μW (1 μW). Table 4.1 summarizes the laser performance in air and water.

Environment	Q	Pth (exp)	Pth (sim)	Efficiency	Evanescent component
		μW	μW	%	%
air	$2.8{\times}10^5$	3	1	1.6	0.6
water	$1.3{\times}10^5$	15	4	0.5	3.6

Table 4.1. Comparison of microtoroid laser results in air and water

4.4 Summary

In conclusion, the author has demonstrated a solid-state microcavity laser whose cavity mode extends into water. The ytterbium-doped silica gain medium was fabricated by solgel synthesis. The laser generates light with an output power of 2 μW and threshold of 14 μW. The Schawlow-Townes equation quantifies the fundamental laser linewidth ($\delta\nu$) for a single mode laser ignoring any technical noise [86].

$$\delta\nu = \frac{\pi h \nu^3}{P Q^2} \tag{4.1}$$

Given the experimental values for laser power ($P = 2$ μW) and the water absorption limited quality factor ($Q = 6.5 \times 10^5$) at 1.04 μm, we estimate that the fundamental linewidth of the ytterbium silica laser presented in this work is 60 kHz, which is significantly narrower than the linewidth of an ultra-high-Q passive microcavity (of order 1 MHz). As a result, this laser can have higher sensitivity to biological molecules in aqueous solution than a passive resonator. The laser threshold, output power, efficiency, and emission frequency can be modified by a molecule located close to the microtoroid, providing several possible sensing mechanisms.

In addition to biological sensing, this novel active laser sensor could find application as a chemical sensor, or be utilized for research on thin-films and other material properties.

Chapter 5

High-Q surface plasmon-polariton microcavity

5.1 Introduction

As the research presented in this thesis has shown, microcavities are ideal vehicles for studying light and matter interaction due to their resonant property, which allows individual photons to sample their environment thousands of times. Accurate loss characterization is possible through Q factor measurements, which can elucidate origins of loss if the measurements are performed while varying factors under study (e.g., presence of water).

This chapter explores the interaction of light and metal in surface plasmon polariton (SPP) microcavity resonators. The aim of this research effort is to accurately quantify metal loss for SPP waves traveling at the interface between glass and silver. The electric field components of SPP modes in the resonator are calculated by FEM simulation. Two types of plasmonic microcavity resonators are built and tested based on the microtoroid, and microdisk. Only dielectric resonances are observed in the microtoroid resonator, where the optical radiation is attenuated by a metal coating at the surface. However, a silver coated silica microdisk resonator is demonstrated with surface plasmon resonances. In fact, the plasmonic microdisk resonator has record Q for any plasmonic microresonator. Potential applications of a high quality plasmonic waveguide include on-chip, high-frequency communication and sensing.

5.1.1 Plasmonics

A plasmon is an oscillation of the free electron gas that resides in metals. Plasmons are easy to excite in metals because of the abundance of loosely bound, or free, electrons in the highest valence shell. These electrons physically respond to electric fields, either present in a crystal or from an external source. Obviously, light contains electric field components and can therefore modify the electron gas in a metal. In fact, photons incident on a metal conductor at a frequency less than the plasmon frequency will be reflected. But, if the optical frequency is higher than the plasmon frequency, then the light will be transmitted through the metal since the electrons cannot respond fast enough to screen the light. What if light could interact with a metal in a third manner, one not of reflection or transmission? Such a field exists, named surface plasmonics, and involves traveling waves of electron oscillation in a metal.

5.1.2 Surface plasmon polaritons

Surface plasmons are electron oscillations that are confined to the interface of a metal and a dielectric, for example glass or air. Due to their high electric field components at the surface, surface plasmons are extremely sensitive to surface particles. Surface plasmons have gained significant attention for their high frequencies, as high as 100 THz. High bandwidth transmission lines could be created using surface plasmonics for on-chip computing.

A polariton can be described as a particle, one that results from strong coupling of electromagnetic waves (i.e., light) with electric dipoles (i.e., electron gas). If light is incident on a metal with a momentum matched to that of the SPP mode, then the optical wave can couple into a surface plasmon polariton wave traveling at the surface of the metal. Also, a SPP wave can couple out of the metal and thus reappear as light. This effect is demonstrated by fiber taper coupling of light into and out of a SPP resonator.

5.1.3 Plasmon resonator concept

Whereas optical micro- and nanocavities made of dielectric or semiconducting materials exhibit large Q factors as well as small diffraction-limited cavity mode volumes, their metallic counterparts (surface-plasmonic cavities [24, 25, 87, 26, 88, 89, 90, 91] have been optimized primarily for subwavelength-scale miniaturization and have given results well below the theoretically predicted performance limit−especially in terms of cavity loss−set by ohmic loss in the metal. This is believed to result from other loss contributions such as surface scattering, radiation, finite cavity mirror reflectance or a significant degree of field penetration into the metal. However, these seemingly distinct dielectric and plasmonic waveguiding principles can be combined in a single cavity by using mature optical microcavity technology such as that provided by disk [9, 92] or toroidal microcavities [10]. A surface-plasmonic whispering-gallery microcavity with a cavity plasmon-polariton loss rate close to the theoretical limit will be presented.

5.2 Microtoroid plasmonic resonator

The search for SPP resonances in a microcavity started with a gold coated ultra-high Q microtoroid. At first glance, the microtoroid appears to be better suited than the lower intrinsic optical Q microdisk due to the smoother surface finish formed by selective CO_2 laser reflow. However, near ideal Q SPP resonances will be observed in a silver coated microdisk, possibly due to better coating uniformity and absence of the thin chrome layer.

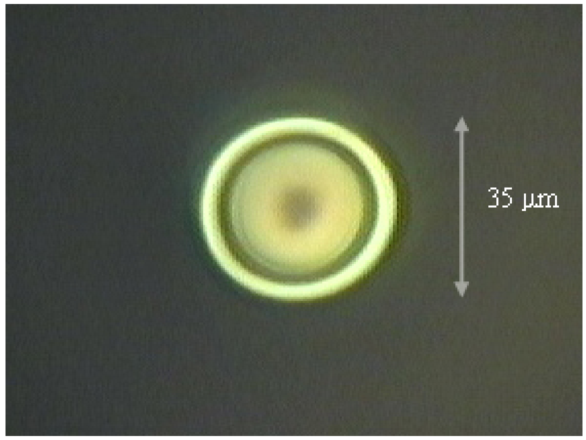

Figure 5.1. Microscope image of a silica microtoroid coated with 200 nm gold coating (top view)

5.2.1 Fabrication of metal coated microtoroid resonator

A small diameter ($D = 34\,\mu$m) microtoroid is fabricated by lithography, etching, and laser reflow. First, a 10 nm layer of chromium is deposited by vacuum sputtering for adhesion. Next, a 200 nm layer of gold is sputtered onto the microtoroids. Gold was chosen because it has lower loss than most metals, except for silver. Figure 5.1 is a microscope image of the gold coated toroid.

5.2.2 Microtoroid resonator results

The gold coated microtoroid resonator is probed optically with a sub-micron diameter fiber taper. For best coupling to the dielectric modes observed in the gold coated toroid, the fiber taper is located underneath the toroid. In this position, the injected optical wave does not have to tunnel through the gold layer. The spectrum of the gold coated toroid resonator was measured using a single frequency tunable laser scanned from 1525 to 1570 nm. The taper transmission, showing the resonance locations, is recorded using a low-noise photodetector.

The resonator spectrum exhibits three resonances as shown in Figure 5.2, locations of propagating modes in the microtoroid. The three resonances are smooth, and appear to correspond to the same mode based on the identical resonance widths and free spectral range (FSR) of the modes. The critical coupled Quality factor is 390, and the FSR is 15 nm. For this toroid's diameter of 3 μm, the FSR indicates an experimental effective cavity mode index (n_{eff}) of 1.45. The resonances observed in this gold coated microtoroid are confirmed to be lossy dielectric modes.

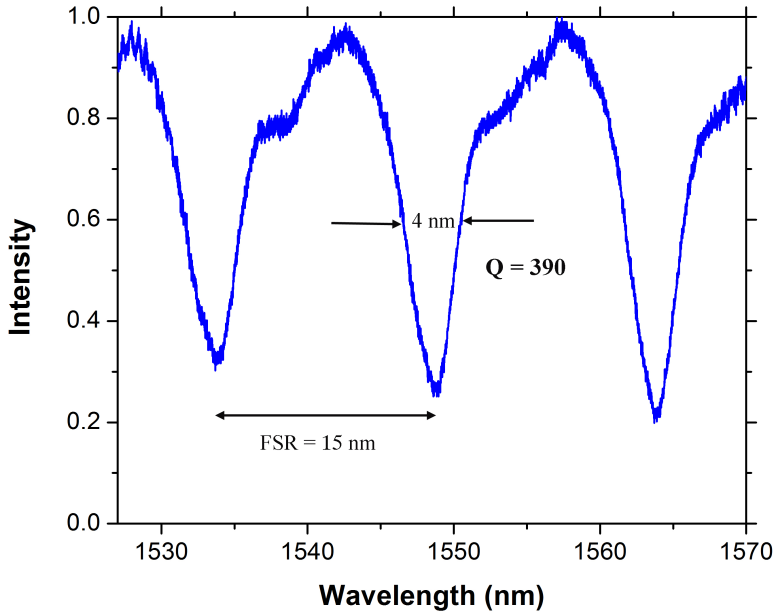

Figure 5.2. Plot of fiber taper transmission versus wavelength of coupling to a gold coated microtoroid showing frequency spectrum of a lossy dielectric mode. Three resonances are shown, corresponding to the same longitudinal mode. The free-spectral range and resonance FWHM linewidth are marked. The resonance $Q = 390$, and FSR= 15 nm.

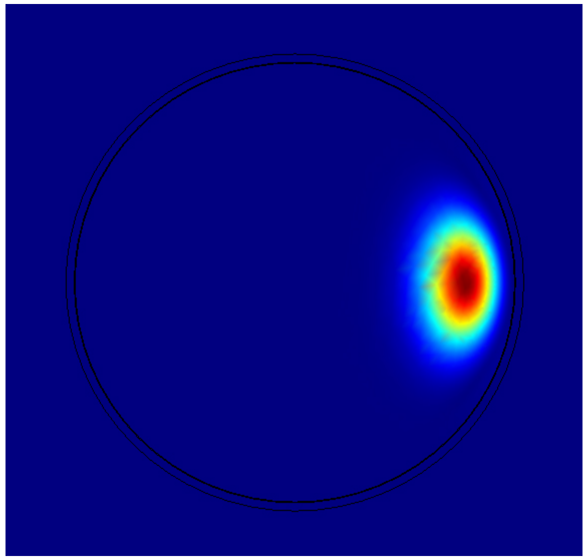

Figure 5.3. Plot of the dielectric cavity mode of a gold-coated microtoroid generated by FEM simulation. The innermost coating is 10 nm of chrome (not visible), and the outer coating is 150 nm of gold (visible).

Bumki Min developed a fully-vectorial finite element model of the silica microtoroid with the 10 nm chrome and the 150 nm gold layers. A cross-sectional image of the fundamental dielectric mode of metal coated microtoroid resonator is shown in Figure 5.3. The dielectric mode's power is confined inside the silica, and decays exponentially within the metal. FEM simulation of the mode for adjacent longitudinal mode numbers, m, determines the cavity mode effective index $n_{eff} = 1.45$, identical to experimental results. Therefore, the only resonances confirmed in the gold coated microtoroid cavity are lossy dielectric modes. One reason for the lack of SPP modes, which have lower Q than dielectric modes, may be non-conformal coating of the microtoroid due to its circular cross section. However, a collaboration between the author and Bumki Min successfully demonstrates a SPP microdisk resonator. The linear geometry of the microdisk bevel edge produces more uniform metal coating of the resonator.

5.3 Microdisk based plasmonic resonator

5.3.1 Plasmonic disk resonator fabrication

A plasmonic microdisk cavity structure is shown in Figure 5.4a. The plasmonic cavity is composed of a silica (silicondioxide) disk microcavity coated with a thin layer of silver. Silica microdisk resonators are ideal templates for the study of surface-plasmonic whispering-gallery modes primarily because they routinely have optical Q factors greater than 10^6. Using the wedge structure shown in Figure 5.4a, Q factors as high as 6×10^7 have been demonstrated [9].

The silica microdisks are fabricated by photolithography and a modified buffered oxide etching. During the wet etch, the photoresist is undercut and produces a bevelled silica edge, which provides conformal silver coating of the top surface of the microdisk. The bevel angle is determined by additional etching time and control of adhesion between the resist and silica layer. The silver coating is deposited on the template silica microdisks using a d.c. sputtering technique with a chamber argon pressure of 30 mtorr.

Two batches of samples (series 1 and 2) are prepared in this way to investigate the size-dependent characteristics of SPP microcavities. A scanning electron image of a silver-coated SPP microdisk resonator is shown in Figure 5.4b, and an expanded view of the edge of the disk resonator is shown in Figure 5.4c.

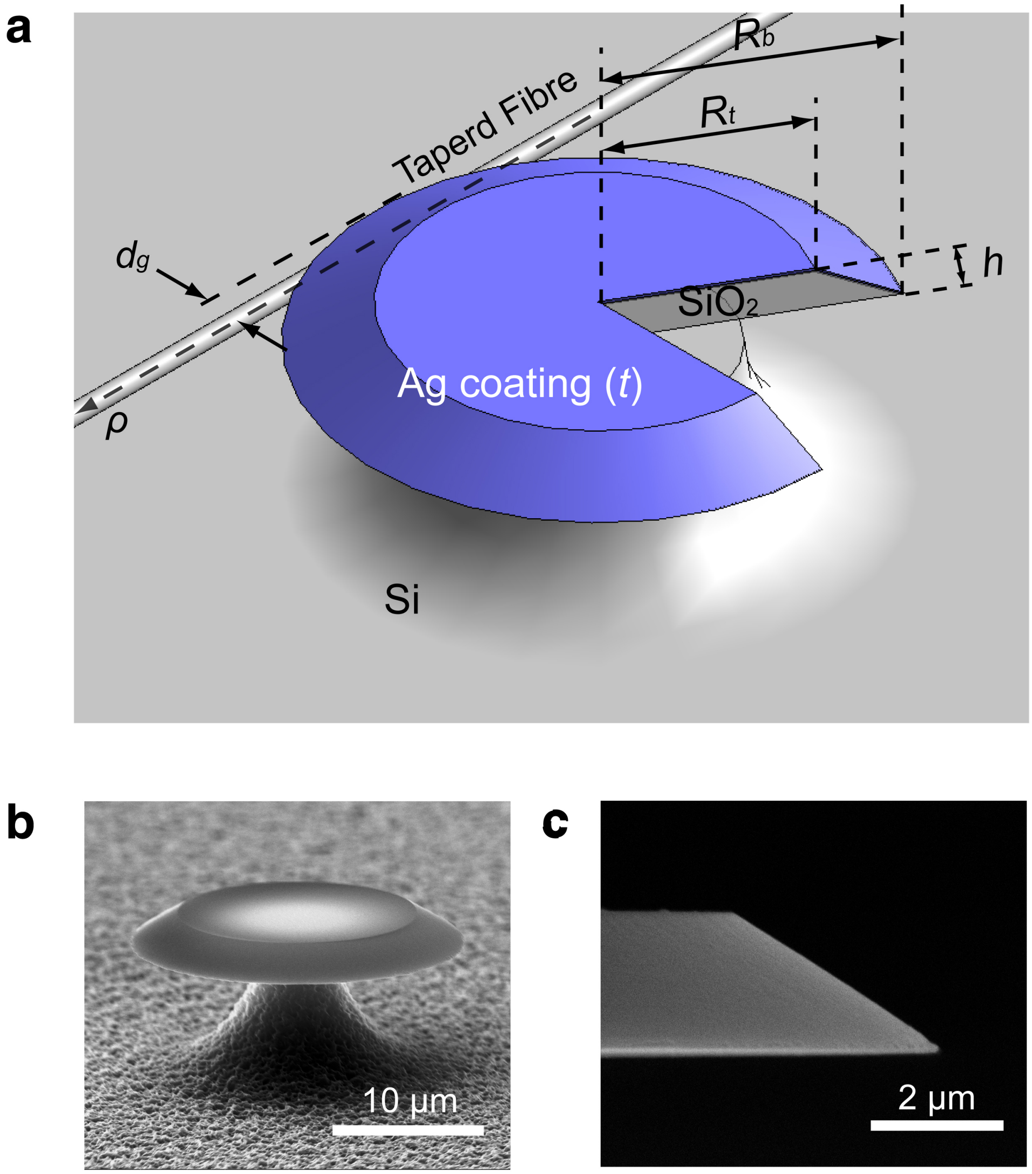

Figure 5.4. **a**, SPP microdisk resonator with a tapered optical fiber passing under its edge. The wedge-shaped disk edge is a by-product of isotropic buffered hydrofluoric acid etching of silica. A transverse cross-section of the cavity is shown for clarity. R_b−bottom radius; R_t−top radius; d−thickness of the silica disk resonator; t−thickness of the metal layer. The straight fiber waveguide axis is denoted by the coordinate ρ and the gap width, d_g, is defined as the horizontal distance from the dielectric cavity edge to the fiber axis. **b**, Scanning electron micrograph of a fabricated silver-coated SPP microdisk resonator ($R_b = 10.96\,\mu$m, $R_t = 57.89\,\mu$m, $d = 2\mu$m, $t \approx 100\,$nm). **c**, Expanded view of the edge of the SPP microdisk resonator.

5.4 Finite-element model of SPP resonator

A full vectorial finite-element analysis was performed for the SPP microdisk resonators [11, 93], taking into account the effects of silver [94] and silica [95] material dispersion. The theoretical cavity mode dispersion diagram of an SPP microdisk resonator (Figure 5.5) shows the real part of the eigenfrequency, f, of the cavity modes as a function of an azimuthal mode number, m. The vacuum light line is defined by $f = \frac{mc}{2\pi R_b}$ with respect to the bottom radius, R_b, of the template silica disk microcavity, and the silica light line is similarly defined by $f = \frac{mc}{2\pi n_{silica}(f)R_b}$. Note that c is the speed of light and n_{silica} is the refractive index of silica. The eigenmodes of an SPP microcavity can be classified into two distinctive categories in terms of the cavity mode dispersion: (1) surface–plasmonic modes at the metal–dielectric interface and (2) optical dielectric modes due to the presence of a dielectric waveguiding channel. The dielectric modes are similar to those observed in the gold coated microtoroid.

In the insets of Figure 5.5, the fundamental SPP eigenmode, the second-order SPP eigenmode and the fundamental dielectric eigenmode are plotted for magnetic energy density $u_M = (1/2\mu_0)|\mathbf{B}(r,\phi,z)|^2$ (where μ_0 is the permeability of free space) using a false-color map (a conventional cylindrical coordinate system (r,ϕ,z) is used for the analysis). The SPP eigenmodes of an SPP microdisk resonator have electromagnetic energy-density profiles with a peak at the silica-metal interface in the transverse plane (constant ϕ). The SPP eigenmodes are identified as SPP_{qm}, where q is the plasmonic mode number ($\mathbf{H}(r,\phi,z) = \mathbf{H}^{qm}_{\mathrm{SPP}}(r,z)e^{im\phi}$), and the optical dielectric eigenmodes are denoted by DE_{hm}, where h is the dielectric mode number ($\mathbf{H}(r,\phi,z) = \mathbf{H}^{hm}_{\mathrm{DE}}(r,z)e^{im\phi}$). The plasmonic mode number is defined as the number of antinodes in $|\mathbf{H}^{qm}_{\mathrm{SPP}}|$ along the silica-metal interface (excluding the vicinity of the sharp corner of the microcavity). Dispersion relations for the four lowest-order SPP eigenmodes ($q = 1,2,3,4$) and the two lowest-order dielectric eigenmodes ($h = 1,2$) are plotted in Figure 5.5. The mode numbers, $h = 1,2,\ldots$, of the dielectric eigenmodes DE_{hm} are assigned in order from lowest to highest order dielectric eigenmode. Depending on the geometry and the mode number h, dielectric eigenmodes can possess certain degrees of plasmonic characteristics due to the presence of the metal–silica interface.

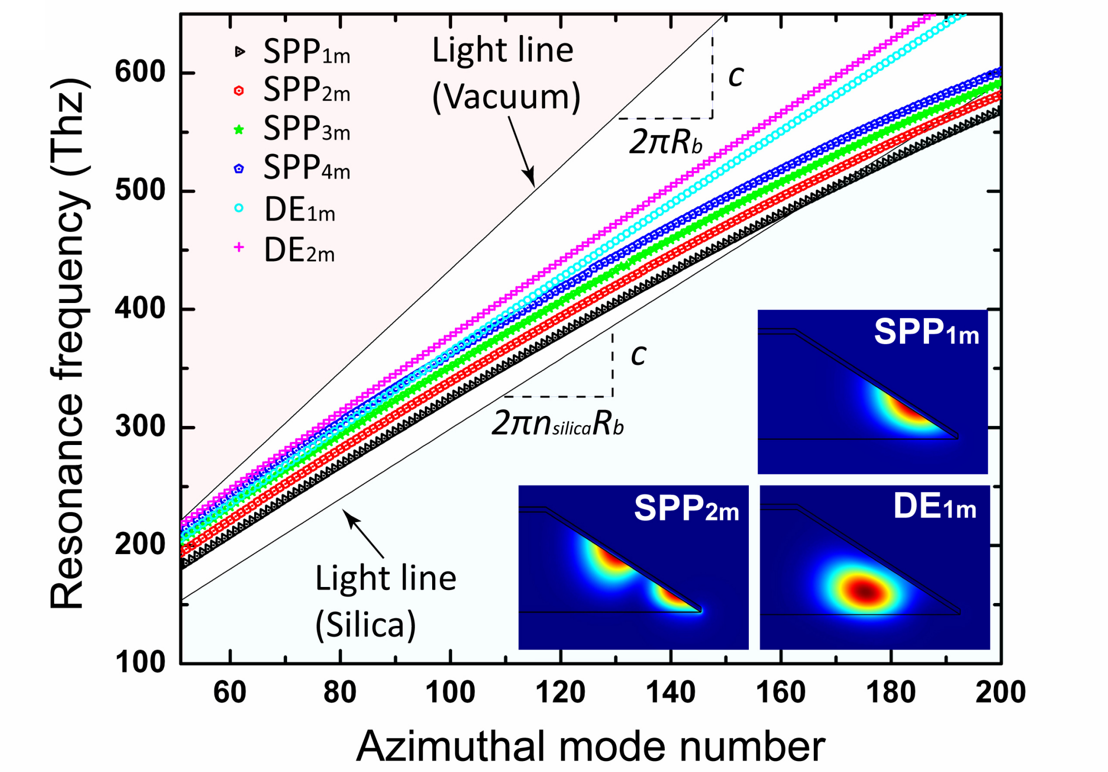

Figure 5.5. Cavity mode dispersion curves for an SPP microdisk resonator, calculated from finite-element eigenfrequency analysis. For this calculation, the thickness of the silver layer is 100 nm, and the bottom and top radii and the thickness of the template silica microdisk resonator were set to 11, 7.9, and 2 μ m, respectively. Light lines, corresponding to vacuum and silica, are given as two black lines (silica material dispersion has been taken into account). For clarity, only the four lowest-order SPP eigenmodes and the two lowest order dielectric eigenmodes are plotted. The first- and second-order SPP eigenmodes (SPP_{1m}, SPP_{2m}) and the fundamental dielectric eigenmode (DE_{1m}) are shown in the inset.

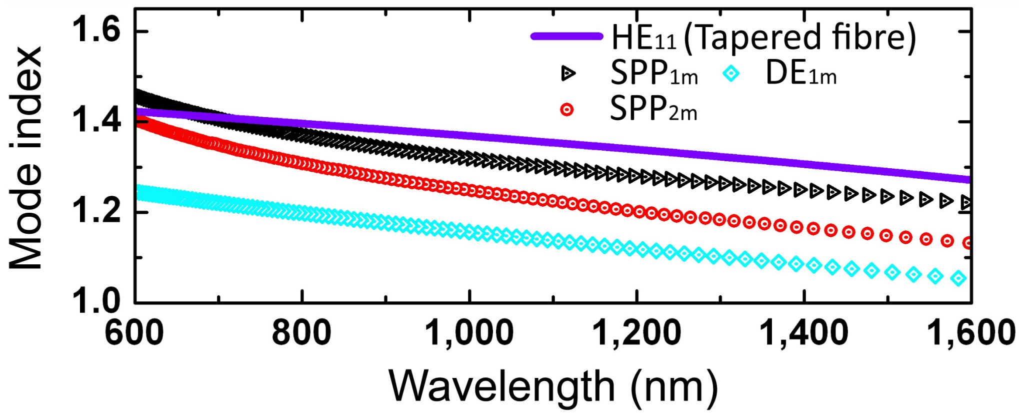

Figure 5.6. Effective cavity mode indices, n_c, of SPP_{1m}, SPP_{2m} and DE_{1m} (with respect to R_b), shown as a function of resonance wavelength. The mode index of a tapered-fiber HE_{11} mode is shown to demonstrate phase matching.

5.4.1 Fiber and SPP resonator phase matching

The cavity mode index, n_c, of a specific eigenmode can be evaluated with respect to the dielectric cavity edge ($r = R_b$) as $n_c = mc/2\pi R_b f$. Figure 5.6 shows the calculated mode index for modes SPP_{1m}, SPP_{2m}, and DE_{1m}. The mode index of a fundamental surface-plasmonic mode (SPP_{1m}) is larger than that of a fundamental dielectric mode (DE_{1m}) within most of the visible and near-infrared frequency band, due to the plasmonic surface-wave characteristics. The mode index is important because it determines the phase matching condition for excitation of SPP modes by a tapered fiber.

After n_c has been calculated, the corresponding phase matched fiber mode index can be obtained by two different approaches. (1) Using the coupled-mode theory, the evaluation of the coupling coefficient κ involves the overlap integral of the cavity eigenmode and the tapered-fiber eigenmode. To have a non-zero coupling strength, the waveguide mode index can be approximated by setting the ϕ dependence of the integrand to zero to give

$$n_w \approx n_c \frac{\sin^{-1}\sqrt{\delta(2-\delta)}}{\sqrt{\delta(2-\delta)}} = n_c(1 + \frac{1}{3}\delta + \frac{2}{15}\delta^2 + O(\delta^3)) \tag{5.1}$$

where $d = -d_g/R_b \geq 0$ denotes the relative gap width (d_g, gap width).

(2) Alternatively, the phase-matching condition can be found by path-averaging the effective mode index seen by the straight fiber waveguide [96]. This gives exactly the same formula

$$n_w \approx n_c \frac{2\tan^{-1}(\delta/\sqrt{\delta(2-\delta)})}{\sqrt{\delta(2-\delta)}} = n_c(1 + \frac{1}{3}\delta + \frac{2}{15}\delta^2 + O(\delta^3)) \tag{5.2}$$

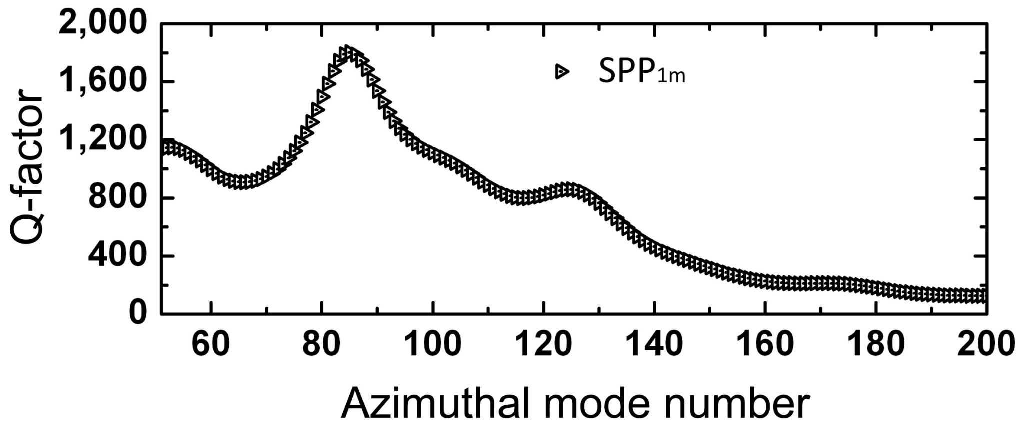

Figure 5.7. The theoretical Q factor for SPP_{1m}, plotted as a function of azimuthal mode number, m

confirming the asymptotic dependence of phase matching on the relative gap width, δ. This formula applies only to the case of negative gap width, that is, $\delta = -d/R_b \geq 0$.

To qualitatively describe the effect of gap width variation on the phase matching, the HE_{11} mode index of a fiber waveguide with a 1-μm waist diameter is shown in Figure 5.6. The fiber mode index is slightly larger than the SPP_{1m} mode index in the near-infrared wavelength band. However, owing to the above phase-matching formula, the SPP_{1m} eigenmode can be effectively phase-matched to the tapered-fiber eigenmode by increasing the relative gap width. The diameter of the tapered fiber can be optimized to phase-match the cavity eigenmodes to the fiber eigenmode.

5.4.2 SPP resonator quality factor

The calculated cavity Q factors for SPP_{1m} eigenmodes as a function of azimuthal mode number, m, are presented in Figure 5.7. The calculated Q factors consist of contributions from intrinsic metal loss (silica material loss is negligible in comparison with metal loss [11, 94, 95]) and the geometry- and material- dependent radiation loss into free space: $Q^{-1} \approx Q^{-1}_{metal} + Q^{-1}_{rad}$. Therefore, this Q value provides the ideal theoretical limit on the Q performance of SPP microdisk resonators that have negligible scattering loss induced by surface roughness.

From the finite-element eigenfrequency analysis, the complex-valued eigenfrequency, $f = f_{re} + if_{im}$, can be calculated, and Q factors evaluated using the formula $Q = f_{re}/2f_{im}$. The radiation-limited Q factor can be estimated and separated from the metal-loss-limited Q factor by removing the imaginary part of the permittivity of silver. For example, the radiation-limited Q factor for $m = 54$ (Figure 5.7) is 3.9×10^6, and for $m = 85$ the Q factor is 6.7×10^9, both of which are orders of magnitude larger than the total Q factors.

The radiation-limited Q factor, Q_{rad}, is orders of magnitude larger than the metal-loss-limited Q

factor, Q_{metal}; the ideal SPP microcavity is thus metal-loss limited: $Q^{-1} \approx Q_{metal}^{-1}$. In Figure 5.8a, the highest fundamental SPP Q factor is found to be 1,800 at the resonant wavelength of 1,062.45 μm (m = 85). At a wavelength of 1,568.25 μm (m = 54), which is close to the value used in measurements described below (Figure 5.8a), the theoretical Q factor is 1,140.

5.5 Plasmonic resonator results

5.5.1 Testing setup

To measure the SPP microdisk resonances experimentally, a narrow linewidth (< 300 kHz) tunable external-cavity semiconductor laser is coupled to the tapered fiber waveguide and scanned over the 1,520–1,570 nm wavelength range. The position of the tapered fiber with respect to the SPP microdisk resonator is controlled at a fixed vertical distance by piezoelectric stages with 100 nm resolution, and the laser polarization is controlled using a fiber polarization controller and monitored with a polarimeter. For large overlap between the cavity and the waveguide modes, the tapered fiber is positioned underneath the bevelled edge of the resonator, where the silica microdisk is free of silver coating. The output transmission is recorded using a photodetector and a digital oscilloscope.

5.5.2 Measured quality factors

Figure 5.8a shows the normalized transmission spectrum from an SPP microdisk resonator with a Lorentzian line-shape fit (Figure 5.8a, red curve) to each resonance. Two resonances, located at 1,523.59 and 1,532.76 nm ($\mathrm{SPP}_{1,83}$ and $\mathrm{DE}_{1,74}$, as estimated by calculation), can be clearly identified. An expanded view of the scan (main panel modes outlined) is shown in the inset of Figure 5.8a and spans three free spectral ranges of SPP and dielectric eigenmodes. The cavity Q factor for the fundamental $\mathrm{SPP}_{1,83}$ eigenmode is found to be 1,377 (which falls within the theoretical Q-factor range of $760 \leq Q \leq 2,360$, with a nominal Q factor of 1,225 for the $\mathrm{SPP}_{1,83}$ eigenmode), and that of the fundamental $\mathrm{DE}_{1,74}$ mode is 4,025. This SPP Q factor of 1,376 is over 30 times larger than the Q factors reported in previous SPP cavity work [97, 27, 98, 99, 100], and larger than the Q factor measured in the gold coated microtoroid the author studied.

To determine the reproducibility of this Q factor, two series of samples of different nominal sizes (series 1, $R_b = 10.93\,\mu$m; series 2, $R_b = 15.56\,\mu$m) were tested. The measured Q factors for both the SPP and dielectric eigenmodes in the 1,550 nm wavelength band are plotted statistically in Figure 5.8b. Two separate clusters of Q factors are seen in this plot, indicating the distinctive resonant characteristics of the two sorts of eigenmode and a tendency for loss to decrease (Q factor to increase) as the size of the cavity increases.

To test the metal-dependent resonance characteristics of the SPP microdisk, chromium (which is

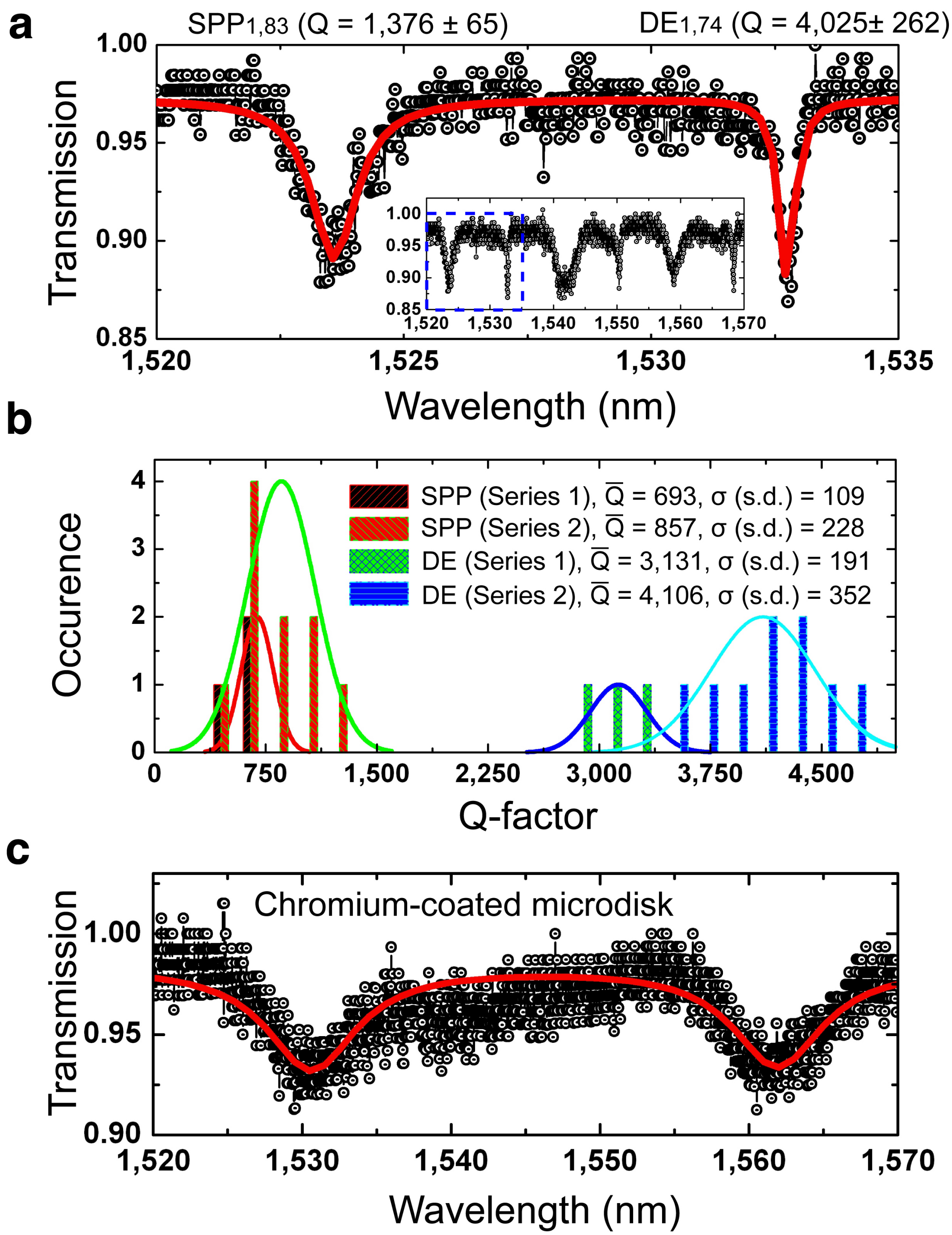

Figure 5.8. **a**, Normalized transmission spectrum showing the highest measured SPP Q factor of 1,377 and a dielectric resonance with a Q factor of 4,025. **b**, Statistical histogram of measured Q values for two different sample batches (series 1 and series 2). Mean ($\overline{Q}$), and standard deviation (σ) of Q factors are shown in the key (series 1, $n = 3$ measurements; series 2, $n = 9$). **c**, Normalized transmission spectrum for a chromium-coated microdisk resonator with Lorentzian fit

highly lossy at optical frequencies) was deposited onto the silica microdisk using the same sputtering process, for use in control experiments. The normalized transmission spectrum for a chromium-coated microdisk resonator is shown in Figure 5.8c. In this case, only low-Q resonances (for example $Q \approx 213$ at 1,561 nm) are observed, owing to the presence of the chromium layer. These resonances are primarily of optical dielectric origin, as confirmed by finite-element simulations, because the fundamental SPP eigenmodes of a chromium-coated microdisk of this size should have a theoretical Q factor of $\sim$10 in the 1,550 nm band.

5.5.3 SPP modes dependence on coupling

To verify the phase-matched excitation of the cavity eigenmodes, a series of measurements were performed with variations in the position of the tapered fiber waveguide relative to the SPP cavity. Figure 5.9 shows the normalized transmission spectra (for an SPP microdisk from a batch from series 2) excited at different gap widths, d_g, and also the corresponding optical micrographs and relative positions between the cavity and the tapered fiber waveguide. Each of the eigenmodes is assigned a mode number (Figure 5.9a) inferred from finite-element simulations. To assign mode numbers to the experimentally obtained resonance spectra, such as those shown in Figure 5.9a, the size of the cavity is measured with a scanning electron microscope and the measured geometrical dimension is used in the finite-element calculation. Owing to the high sensitivity of the resonance frequency with respect to the nanoscale geometrical variation and the permittivity of the component materials, only the approximate mode numbers can be inferred. There being distinct ranges of Q factors indirectly confirms the theoretical SPP and dielectric resonance locations. Then the transmission of each resonance is experimentally determined by varying the gap width and the input polarization to assign distinct resonant characteristics precisely to each of the eigenmodes.

The importance of the phase matching between cavity and fiber eigenmodes is manifest in the observed transmission spectra. At larger gap widths ($d_g \approx 0.8, 0.4\,\mu$m), only the resonances of the first and second-order SPP eigenmodes (SPP_{1m} and SPP_{2m}) are observable, and the fundamental dielectric eigenmode (DE_{1m}) resonances are absent. This is because, for this range of larger gap widths, SPP eigenmodes are better phase-matched to the fiber eigenmode [96] and have a larger field overlap with the fundamental fiber eigenmode (they are located closer to the edge of, and extend farther outside, the microcavity than does the fundamental dielectric eigenmode in the wedge-shaped structure). As the gap width decreases further ($d_g \leq 0$), the fundamental dielectric eigenmodes are excited, as the phase-matching condition can be partly satisfied by decreasing d_g. For negative gap width, the SPP resonances are even more pronounced, as the phasematching condition between the SPP and fiber eigenmodes can be fully satisfied owing to gap-width-induced phase matching, as is shown qualitatively in Figure 5.6. For the SPP resonance at 1565.4 nm, an input power transfer of up to 50% is demonstrated, showing the effectiveness of phase-matching control using the tapered

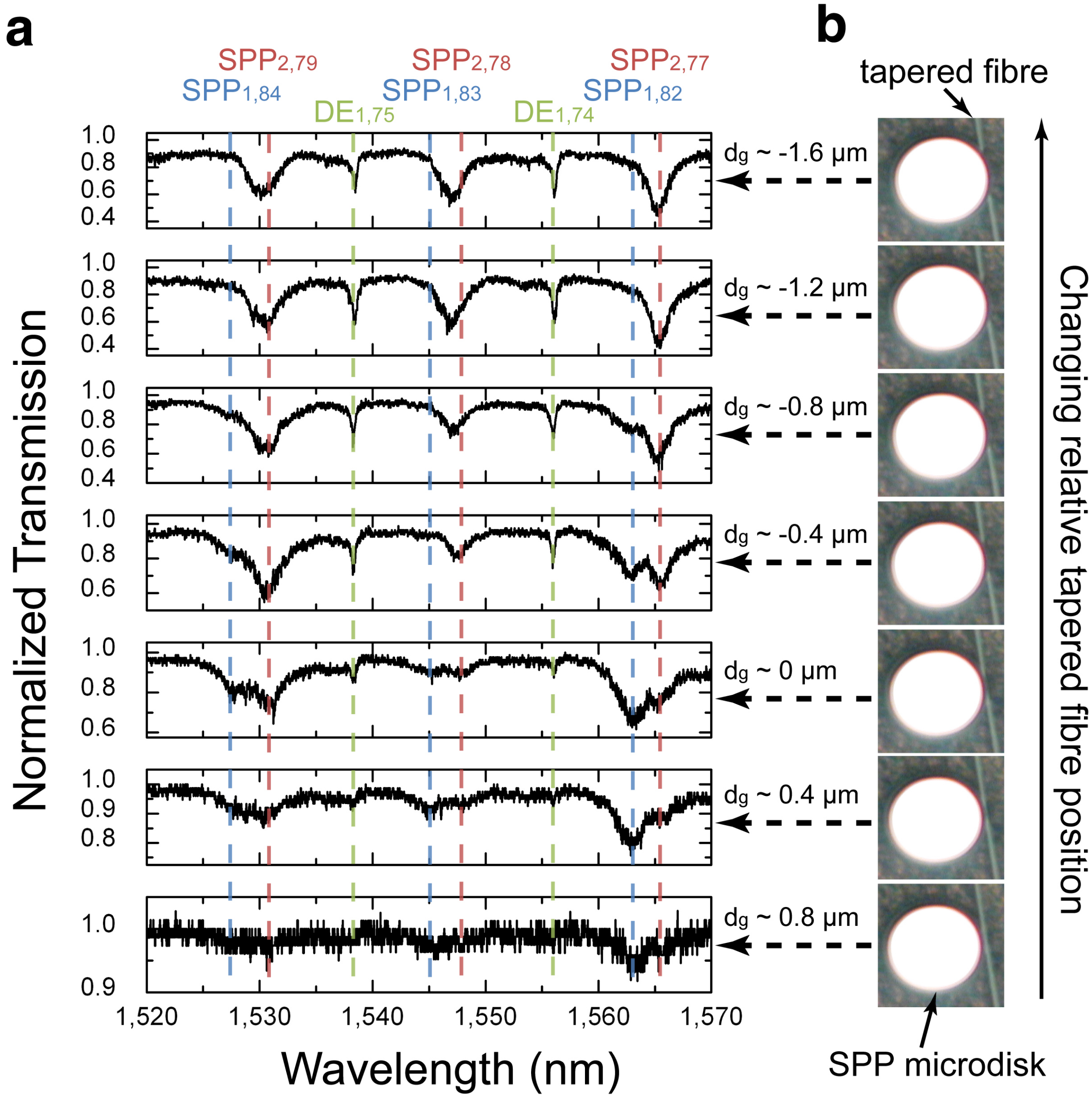

Figure 5.9. Transmission spectrum versus waveguide coupling gap. **a**, Series of normalized transmission spectra, recorded for a variety of gap widths between the tapered fiber waveguide and the edge of the SPP microdisk. Resonances of SPP and dielectric eigenmodes are shown with estimated mode numbers. $R_b = 15.71\,\mu$m, $R_t = 13.09\,\mu$m, $d = 2\,\mu$m, $t < 100$ nm. For the SPP resonance at 1565.4 nm, an input power transfer of up to 50% is demonstrated (second panel from the top). **b**, Optical micrographs corresponding to the recorded normalized transmission spectra. Estimated gap width, d_g, is also shown.

fiber waveguide.

5.6 Application of SPP resonator

The demonstration of high-Q surface-plasmonic microcavities opens many possibilities for applications in fields ranging from fundamental science to device engineering. As a specific example, it could make possible a plasmonic laser, for which adequate gain materials as well as a high-Q SPP cavity are key prerequisites [101]. Although the demonstrated SPP Q factor is still less than that of an optical micro- or nanocavity [78, 102], the corresponding SPP loss coefficient of $\alpha_{\mathrm{SPP}} \approx 2\pi n_c/\lambda Q_{\mathrm{SPP}} \approx 39\,\mathrm{cm}^{-1}$ (where λ is the wavelength) satisfies the experimental criteria for a laser cavity and shows that, in principle, such surface-plasmonic lasing devices are possible. The tapered-fiber excitation scheme also demonstrates a convenient means of exciting these structures and selectively probing SPP cavity modes, because it directly controls the mode overlap and phase matching between the cavity and fiber eigenmodes. Furthermore, it is notable that the SPP Q factor could be substantially increased beyond the values measured here by lowering the temperature of the SPP microcavity [101, 103]. From a fundamental standpoint, the SPP Q factor is sufficient to observe interesting cavity quantum electrodynamical phenomena in the weak-coupling regime relating to enhanced Purcell factors [102, 104, 105]. In addition, using the high nonlinearity of metal (or materials deposited in the vicinity of the metal), it may be possible to extend the applications of nonlinear plasmonics. Finally, it should be noted that, because the $\lambda^3 Q/V$ values of the present SPP microcavity (approximately a few hundred) are still much less than those provided by the photonic-crystal and dielectric whispering-gallery microcavities [78, 102], it is still important to pursue new plasmonic cavity designs.

5.7 Summary

Surface plasmon polaritons (SPPs) are electron density waves excited at the interfaces between metals and dielectric materials [106]. Owing to their highly localized electromagnetic fields, they may be used for the transport and manipulation of photons on subwavelength scales [24, 25, 87, 26, 88, 89, 90, 91]. In particular, plasmonic resonant cavities represent an application that could exploit this field compression to create ultra-small-mode-volume devices. A key figure of merit in this regard is the ratio of cavity quality factor, Q (related to the dissipation rate of photons confined to the cavity), to cavity mode volume, V [78, 102]. However, plasmonic cavity Q factors have so far been limited to values less than 100 both for visible and near-infrared wavelengths [97, 27, 98, 99, 100]. Significantly, such values are far below the theoretically achievable Q factors for plasmonic resonant structures. In this chapter, a high-Q SPP whispering-gallery microcavity was presented, made by coating the surface of a high-Q silica microresonator with a thin layer of a noble metal. Using this structure, a maximum Q of 1,377 was achieved in the near infrared for surface-plasmonic whispering-gallery modes at room temperature. This nearly ideal value, which is close to the theoretical metal-loss-limited Q factor, is attributed to the suppression and minimization of radiation and scattering losses that are made possible by the geometrical structure and the fabrication method.

Chapter 6

Microtoroid reflow and measurement in vacuum

6.1 Introduction

The most commonly quoted specification of microcavities is quality factor, indeed it is now built into the name given to ultra-high Q (UHQ) microtoroids. Microtoroids have already leveraged their high Q to form single frequency lasers, a high resolution optical coupler, an efficient photon router and biological sensors [20, 19, 107, 30, 31]. All of these applications were made possible by the narrow linewidth of microtoroids modes.

The ultimate limit of microcavity Q, in microtoroids or microspheres for example, has been investigated theoretically and experimentally [6, 7, 108]. The theoretical upper limit on Q for millimeter sized fused silica microspheres is argued to be 1×10^{12} [108], an enormous figure that corresponds to a average photon propagation length of more than 200 km, or 40 million round trips. However, the highest Q measured to date in any silica microcavity is slightly less than 1×10^{10} for a microsphere. This discrepancy indicates that one or more sources of loss in microcavities is higher than predicted. The various sources of loss in optical microcavities will be given in Section 6.2.

Like microspheres, microtoroids have yet to reach their theoretical maximum quality factors. The highest Q measured until now in microtoroids is 4×10^8 [12], lower than microspheres. The lower Q in microtoroids may be partially explained by the higher mode confinement (in the azimuthal direction), which exposes higher field intensities of the cavity mode to surface imperfections and contaminants. Silica microtoroids have become the preferred microcavity for advanced experiments because they are easier to fabricate in large quantities on chip, have planar geometry, and have significantly lower mode volume than silica microspheres. Therefore, many applications will benefit from higher Q microtoroids, if the existing sources of loss may be reduced.

The author has directed novel research into increasing the Q of microtoroids by designing, building, and demonstrating a laser reflow and toroid measurement system in vacuum. Record high Q is expected in a water- and dust-free vacuum environment.

6.2 Sources of loss in microtoroids

In order to increase toroid Q to a record level, the reasons for finite Q must first be understood. Loss in microcavity resonators is caused by numerous sources, whose contributions can be quantified by attenuation coefficients (α_i), and corresponding quality factor Q_i. The relationship is defined as $Q_i = \frac{2\pi n}{\alpha_i \lambda}$. The total quality factor in UHQ microtoroid resonators can be expressed in terms of distinct components for each source of loss, as long as each loss factor is small over one cavity round trip [69].

$$Q_{tot}^{-1} = Q_{mat}^{-1} + Q_{WGM}^{-1} + Q_{ss}^{-1} + Q_{cont}^{-1} + Q_{water}^{-1} + Q_{ext}^{-1} \tag{6.1}$$

The major components of whispering-gallery resonator loss listed above are by no means a complete list, other loss factors may exist and can be accounted for easily. But, the major contributions to total Q include: the intrinsic loss of silica due to absorption and Rayleigh scattering (Q_{mat}), radiation loss of the WGM due to photon tunneling (Q_{WGM}), silica roughness induced surface scattering (Q_{ss}), absorption caused by surface contamination (Q_{cont}), absorption caused by OH groups or water molecules adsorbed into the silica toroid or attached to the surface, and external loss caused by useful taper coupling (Q_{ext}).

6.2.1 Intrinsic loss

Silica has a large transparency window including the visible and near infrared (NIR) wavelengths, making it the ideal dielectric medium for UHQ microcavity resonators. Silica has maximum transmission at 1550 nm, the communications band where the majority of optical information is carried around the world. The intrinsic attenuation factor of silica at 1550 nm is $\alpha_{mat} = 0.2\, dB/km$, which accounts for intrinsic absorption loss and Rayleigh scattering in silica.

Rayleigh scattering is the elastic scattering of light by particles or refractive index variations smaller than the wavelength of light. Normally, Rayleigh scattering losses calculated for plane waves in infinite media is applied without modification to curves microcavities. Gorodetsky deduced that mode confinement in microcavities can actually reduce Rayleigh scattering [108]. But, for the calculations in this chapter, the simple bulk intrinsic loss of silica is assumed for ease of calculation. Therefore, the intrinsic quality factor of silica is 3×10^{10} according to the expression given above. Since the highest Q recorded for a microtoroid is 4×10^8, then the intrinsic loss in silica is not currently the limiting factor.

6.2.2 Whispering gallery loss

In whispering-gallery optical resonators, the optical modes are confined by continuous total internal reflection (TIR) at the silica-air interface. For infinite planar structures, light reflected at an angle below the TIR critical angle will be perfectly reflected assuming there are no absorption losses. But, TIR on a curved interface like a microtoroid is not perfect, and a fraction of the circulating power leaks out as a transmitted wave [109]. Intuitively, a fraction of the circulating photons will strike the silica-air boundary at angles higher than the critical angle and escape. The fraction of photons that are able to tunnel out of the bound state of the WGM is dependent on the cavity radius as expected. FEM simulations of the microtoroid by Sean Spillane show that WGM loss decreases exponentially as a function of the toroid major radius. The WGM limited Q (Q_{WGM}) is greater than 10^{12} for toroids with major diameters (D) of 30 μm or larger and minor diameters (d) greater than 3 μm. Therefore, microtoroids with dimensions exceeding these figures are not limited by WGM loss, and the current limitation to Q in microtoroids must lie elsewhere.

6.2.3 External sources of loss

The two main sources of external loss in microtoroids are the fiber taper coupling and any contaminants that reside on the surface of the toroid. To analyze the effect of taper loading on cavity Q, first the basic properties of optical transfer between the taper and toroid must be discussed [69]. The transmission of the fiber taper can be written as

$$T \equiv \left(\frac{1-K}{1+K}\right)^2 \tag{6.2}$$

where K is the coupling factor defined as $K = \kappa_0^2/\sigma_0^2$ [13]. The coupling factor is the dimensionless ratio of the coupling coefficient (κ_0^2) and the intrinsic loss (σ_0^2).

Fiber taper coupling to a microtoroid can be separated into three regimes. Starting with a large gap between the toroid and taper, in the under coupled regime, the total Q of the toroid is dominated by the intrinsic loss ($K < 1$). When the toroid and taper are critically coupled, the coupling and intrinsic loss coefficients are identical ($K = 1$), and the transmission is zero due to destructive interference of the optical wave traveling down the fiber and the optical field inside the toroid, which is π out of phase. Microcavity lasers are typically operated close to critical coupling, where the stored energy inside the microtoroid is maximum, hence giving the highest pump absorption in the laser cavity. In the over coupled regime, waveguide coupling dominates the total Q ($K > 1$), and the taper is located even closer to the toroid.

The relationship between the total Q and the coupling (κ_0) and intrinsic (σ_0) loss components is:

$$Q_{tot} = \frac{2\pi c}{\lambda(\kappa_0^2 + \sigma_0^2)} \tag{6.3}$$

At critical coupling, $\kappa_0^2 = \sigma_0^2$, the quality factor is exactly half of its intrinsic value. This simple relationship between a measurement of Q at critical coupling and intrinsic Q is valid if the intermodal coupling caused by scattering is weak. Alternatively, the expression for calculating intrinsic Q at critical coupling in the presence of mode splitting was given in Equation (2.15) in **Chapter 2**.

The cavity loading effect on microtoroid Q is unavoidable if the cavity is to be used for any experiment. Therefore, the quantifiable reduction in Q at critical coupling as described above will be accounted for. In short, cavity loss due to taper coupling is not a concern for this research.

All other sources of external loss in microtoroids are grouped together as contamination. Some examples include dust from the air (e.g., human skin cells), silicon particles that are sputtered onto the microtoroid during laser reflow, and photoresist left behind during fabrication. These contaminants can be reduced or eliminated with clean fabrication techniques, proper wafer handling, storage of resonators in a clean nitrogen purged environment, laser reflow with appropriate power levels, and finally by protecting the microtoroids during experiment. The vacuum chamber built for this research project will help clean the toroids before reflow, and maintain their pristine quality during testing. But, the laser reflow in vacuum system is designed to reduce the effect of the most likely source for Q limitation in toroids, common water.

6.3 Microtoroid loss caused by water

Water is a key precursor present during wet-deposition of the thermal oxide layer that is processed into silica microtoroids. Although the thermal oxide layer is annealed at high temperature, residual OH ions can remain and cause significant loss in microtoroids. Also, water adsorbs onto the surface of the toroid in one or more monolayers of liquid H_2O if there is any water vapor present in the air. Since normal air has 30% relative humidity, water adsorption onto microtoroids tested in air is unavoidable. Near infrared light excites vibration of the rotational symmetry of the OH group in water or any chemically fashioned OH groups inside the amorphous silica. The attenuation coefficient of water at 1550 nm is $\alpha_{water} = 2.2 \times 10^3$ m^{-1} [22]. A microtoroid immersed completely in water will have lower Q for this reason, as discussed in **Chapter 4**.

The possibility of quality factor reduction caused by water has been considered in microspheres and microtoroids. In a manuscript that explores the limits of ultimate Q in microspheres, Gorodetsky demonstrates that water adsorption onto the surface of a 750 μm diameter microsphere causes a reduction in cavity Q [6]. Immediately after the microsphere is fabricated by flame, he observed a fast decrease of the cavity lifetime within two minutes. This behavior is consistent with the process of chemical formation of water monolayers on the surface of hydrophilic surfaces like silica [110]. The intrinsic Q of the microsphere drops from 8×10^9 to 1×10^9 within an hour. The initial microsphere Q is partially recovered by baking the microsphere at 400°C, giving strong evidence that water adsorption onto the microsphere surface is the source of limitation for maximum Q in microcavities. Theoretically, if the surface-tension induced reflow and testing could be performed in a perfectly dry environment, then the Q would not suffer due to water absorption. Here lies the exact aim of the research documented in this chapter $-$ to reduce or remove the effect of water in microtoroids for exploration of ultimate Q.

The interaction between water and microtoroid cavities was also studied by Rokhsari and Spillane [111]. The thermal bistability effect was applied for loss characterization of microtoroids, and showed that surface water causes heating of the toroid, and subsequently shifting of the cavity resonance. A FEM simulation was developed for studying the effect of water adsorbed on the surface of a microtoroid. The simulation added, to the surface of the silica microtoroid, a thin dielectric shell with the thickness of a monolayer of water and the attenuation coefficient of water. The maximum Q factor for a microtoroid with such a monolayer of water is predicted to be 7×10^8, close to the highest Q value recorded for microtoroids.

The body of work presented above suggests that absorption loss caused by water may be the limiting factor to ultimate Q in current microtoroid research. If vacuum reflow and toroid testing is performed in vacuum, the microtoroid intrinsic Q may be increased beyond the current boundary. Higher quality factor in microtoroids will permit further research into other loss sources in microtoroids and increase the strong coupling between atoms and the cavity in cQED experiments. Other applications may be found in more efficient nonlinear effects of silica, due to the small mode volume and ultra-high Q of microtoroids.

6.4 Vacuum reflow system

A completely new and never-before demonstrated laser reflow and microtoroid testing system in vacuum was designed and built by the author. This system will drastically reduce or eliminate water adsorption onto the toroid surface after laser reflow, and maintain the toroid's pristine surface during fiber taper testing of the quality factor. As Gorodetsky proved, the initial Q of microcavities instantaneously after reflow is significantly higher than the steady-state Q measured in normal atmosphere after several hours, thought to be due to water content in the air. Laser annealing raises the temperature of silica above its melting point of 1,700°C, at which point the amorphous silica collapses into a torus shape due to surface tension. Annealing in vacuum at this high temperature will bake off water on the surface, and perhaps even water trapped inside the silica microdisk, reducing the absorption loss due to OH groups in the newly minted toroid cavity.

A diagram of the UHQ toroid in vacuum system is presented in Figure 6.1. A high power carbon dioxide (CO_2) gas laser generates a short pulse of infrared radiation at 10.6 μm. The collimated laser pulse passes through several mirrors before the beam is focused down to a 200 μm diameter spot located 7" from the lens. The CO_2 laser pulse is focused down through the IR/visible beam combiner. This three-element optical system combines the laser beam line and imaging system beamline to simultaneously allow imaging and reflow of the microdisk. A silica microdisk, located in the exact center of the laser focus, is selectively reflowed by the invisible laser pulse into a

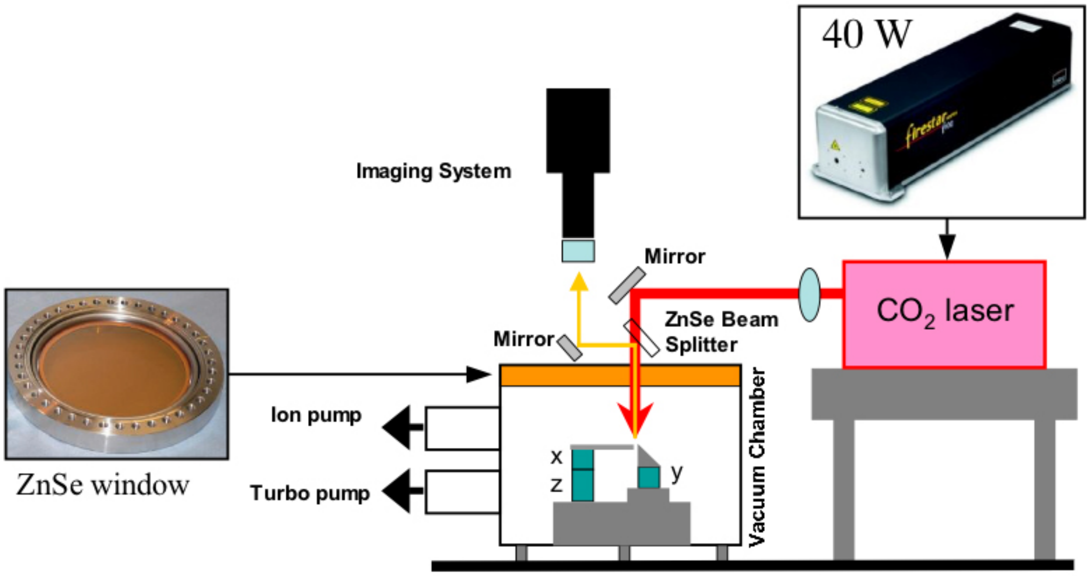

Figure 6.1. Schematic diagram of vacuum reflow concept. The CO_2 laser beam enters the vacuum chamber to reflow microtoroids, and the microtoroids are viewed with a microscope. Coupling is performed with nanopositioners in vacuum.

microtoroid.

The microtoroid is suspended on a silicon substrate, which can be precisely moved using a three-axis Attocube positioning system. After reflow, the microtoroid is translated into coupling with a single-mode fiber taper already resting in the vacuum on an aluminum fork. The combination stepping and piezo movement of the high-precision stages allow for critical coupling of the microtoroid to the tapered fiber. Finally, the intrinsic Q of the microtoroid is measured by cavity ringdown. This entire procedure occurs in high vacuum, at a pressure of 1×10^{-7} Torr. The following sections review the design considerations of the laser reflow and testing systems in vacuum.

6.4.1 Vacuum chamber

The vacuum chamber must be large enough to contain the nanopositioners, fiber taper, large ZnSe upper window, and allow connection of equipment used to maintain and measure the vacuum pressure. The author choose a cylindrical chamber with 8” diameter, 6” height, and a total of 7 vacuum ports. A turbo vacuum pump (Mini Task, Varian) evacuates the chamber from atmospheric pressure down to 1×10^{-5} Torr. However, the turbo pump is mechanical, and therefore causes significant vibrations that prevent stable taper coupling. So, a noble diode ion pump (Vacion Plus 55, Varian) is used to decrease the chamber pressure to 7×10^{-8} Torr. The vibrationless ion pump allows for stable coupling between the toroid and the fiber taper. Two other ports are connected to low (7F, Televac) and high pressure (4A, Televac) vacuum pressure gauges. Also, several ports provide electrical feedthrough of the Attocube cables, and fiber feedthrough. The largest vacuum port connects to the 8" ZnSe window (Torr Scientific) that provides passage of the CO_2 laser beam and visible imaging beam into the chamber at low pressure. The stainless steel vacuum chamber is sourced from Nor-Cal Products Inc., and designed for operation at a pressure as low as 1×10^{-9} Torr.

6.4.2 CO_2 laser annealing

The microtoroid reflow step is the most crucial step in UHQ microtoroid fabrication. The microtoroid must be symmetrically illuminated by a CO_2 laser beam for symmetric reflow in order to show ultra-high Q. The laser beam spot at the microtoroid plane is a product of the laser source and all intermediate optics. A near diffraction-limited ($M^2 < 1.1$) collimated laser beam 2.5 mm in diameter is the output of a commercial high-power CO2 laser (V40, Synrad). Only the highest quality infrared optics were chosen for the laser beamline. Two flat turning mirrors provide accurate beam alignment. A low-distortion ZnSe plano-convex lens with 7" focal length creates a circular beam spot in the focal plane, located inside the vacuum chamber. A third mirror directs the laser pulse down into the chamber, and through a ZnSe flat window that serves as the beam splitter. Finally, the laser beam passes through the 9 mm thick anti-reflection coated ZnSe vacuum window and a 1 mm thick uncoated ZnSe window that protects the ZnSe top window from contamination during laser reflow.

For laser reflow, the microdisk is imaged at lower resolution than used during testing. The distance between the beam combiner and the toroid resonator is large (100 mm), necessitating a long working distance lens objective that results in lower resolution (of order 5 μm). But, the image is sufficiently crisp to allow identification of the microdisk center and observation of the reflow process. The laser focus and microdisk center are aligned together with an alignment mark on the image screen.

The laser is carefully aligned to produce a symmetric and clean focus spot, verified by reflow of glass slides inside the vacuum chamber. The lens position is varied to find the optimum distance between the lens and the reflow plane, which may be different than the focal length. Initially, the silicon chip containing the microdisks to be reflowed was supported by an aluminum base. However, this base was eliminated after discovering that the reflow spot was asymmetric as a result of interference in the toroid plane caused by back reflection of laser light. Also, a thin metal plate bonded at 45° underneath the silicon chip is later added to eliminate a reflection from the aluminum taper holder base.

6.4.3 Microtoroid testing

A solid aluminum base with two towers provides the correct elevation and stable support for the separate taper fiber holder and silicon chip mount. Three Attocube nanopositioners (x,y,z) are stacked on top of one another. Attocube positioners were chosen for their combination of long-range motion (5 mm range), high-resolution (10 nm) piezo actuation, and stability in ultra-high vacuum (UHV). To prevent the laser reflow pulse from damaging or even breaking the fiber taper, the reflow spot is located several millimeters away from the fiber taper. After reflow, an array of up to seven microtoroids on chip is moved towards the fiber taper.

The fiber taper is pulled using a hydrogen flame and two motors until the single mode condition is verified by observing taper transmission dynamics in time. The taper is then transferred from the standard taper puller to an aluminum fork secured by epoxy. The taper is pulled to a smaller final length than normal to prevent transmission loss. The fork is only one inch wide and any portion of the fiber taper mode that encounters the epoxy will be scattered away. After being secured on the fork, the taper is transferred into the vacuum chamber and held over the silicon chip. Then, the top ZnSe window is secured and the chamber is evacuated.

After laser reflow in vacuum is completed, the beam combiner is removed, and a high-resolution objective replaces the long working distance lens to allow high resolution imaging (of order 2 μm) of the microtoroid. To achieve coupling between the toroid and taper, the toroid is first moved within ten microns of the taper in steps. Then, once a cavity resonance has been identified by tuning the single frequency 1550 nm diode laser, the toroid position is optimized into critical coupling with the taper by voltage control of the piezo. Piezo control provides ultra-smooth movement of the toroid and provides in stable coupling.

6.5 Vacuum reflow system assembly

The vacuum chamber is secured to an isolated optical table, and all the vacuum equipment is attached. With blank flanges covering unused ports, the vacuum system is tested for low pressure performance and baked out. Then, the CO_2 laser beam line is aligned carefully, ensuring that the beam is not clipped or distorted as it passes through the mirrors, lens, and windows. Figure 6.2 is a photograph of the CO_2 laser assembly and vacuum chamber.

The beam combiner was designed by the author to bring into co-linear propagation the laser and imaging beams. The combiner is cantilevered out over the ZnSe top window. A photograph of the beam combiner is given in Figure 6.3.

Finally, the vacuum interior is populated with the fiber taper holder (u-shaped fork), three nanopositioners, and the sample mount. A picture of the vacuum chamber inside, showing these components, is shown in Figure 6.4.

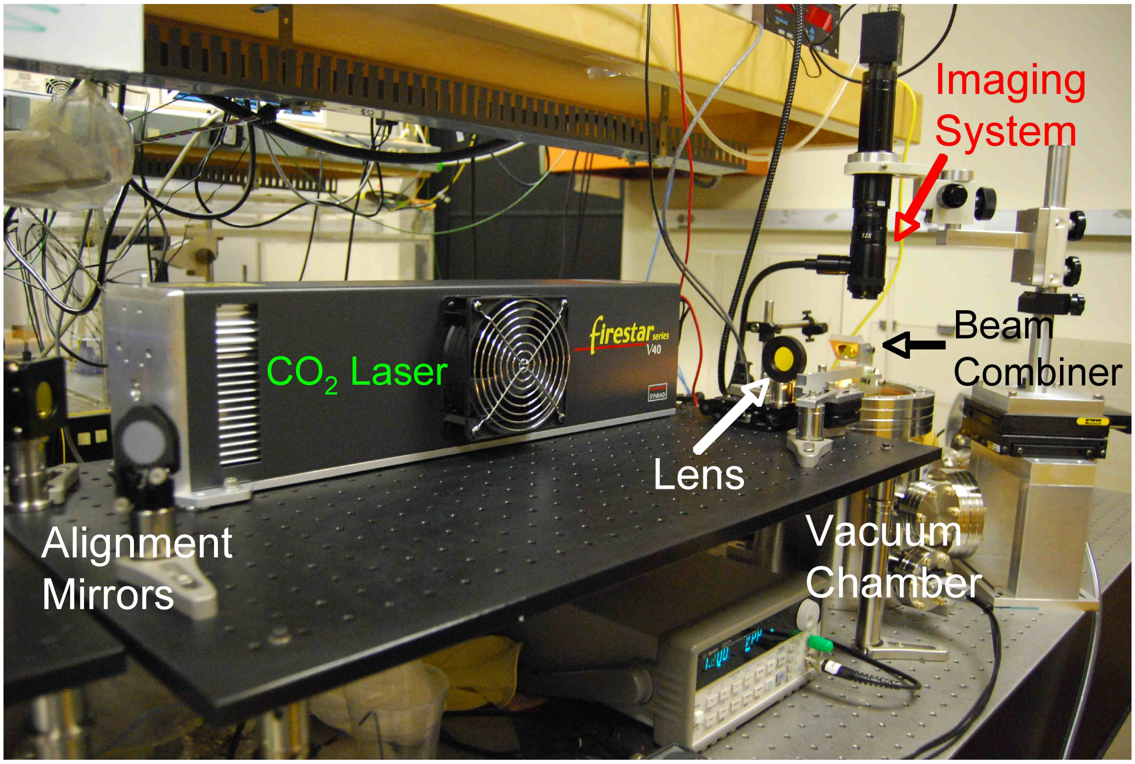

Figure 6.2. Image of CO_2 laser optics and vacuum chamber

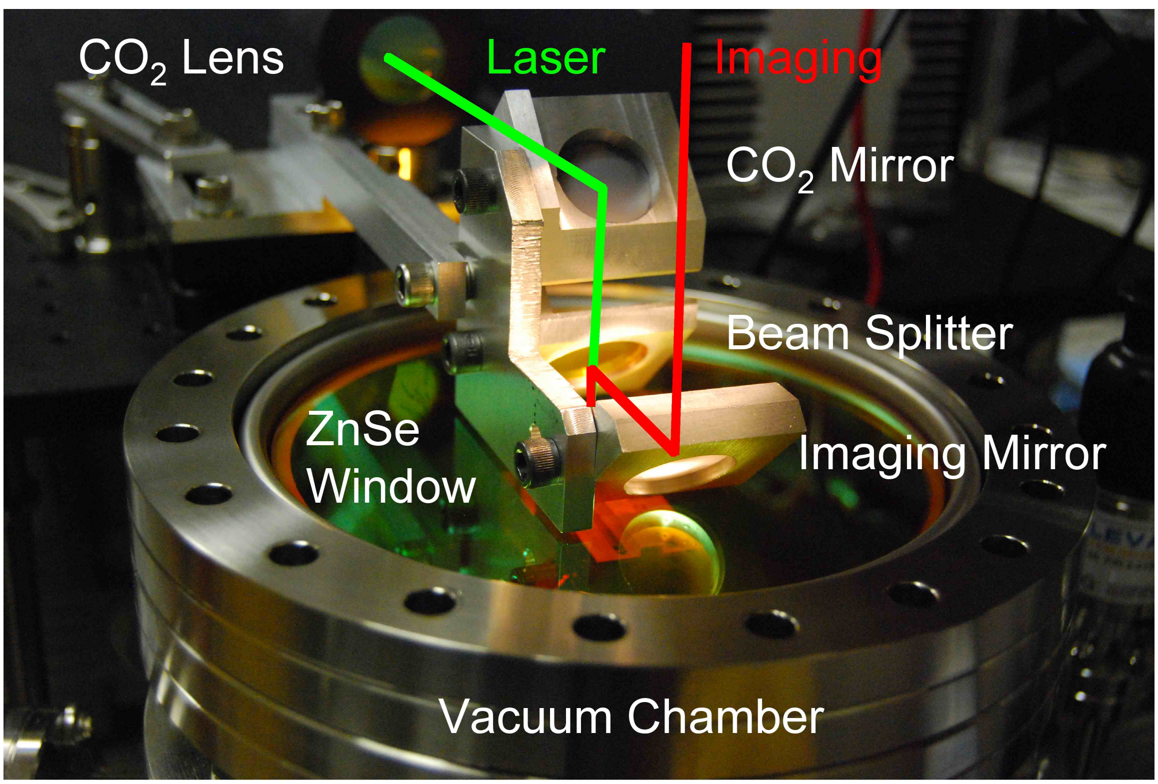

Figure 6.3. Image of laser and imaging beam combiner

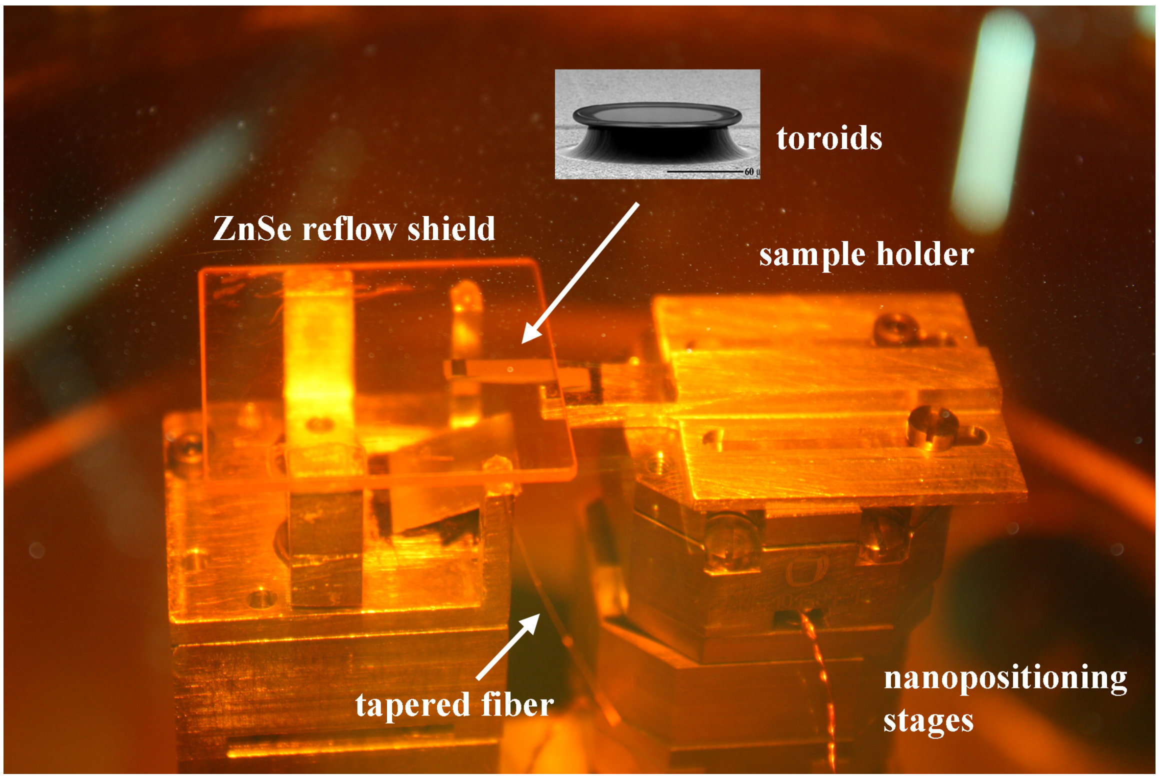

Figure 6.4. Image inside vacuum chamber of microtoroids, shown on a sample holder on nanopositioning stages, underneath a fiber taper. The top ZnSe window (not shown) is protected by a secondary ZnSe window (blast shield).

6.6 Microtoroid reflow and testing in vacuum

To achieve record Q of a microtoroid in vacuum, first the microdisk must have excellent quality. The microdisks were fabricated according to best practices in the Kavli Nanoscience Institute (KNI) at Caltech from 2 μm silicon dioxide layer on prime silicon. The silica layer was grown by wet deposition, which may leave behind lossy OH groups. In the future, silica grown by dry deposition will be tested. In addition to the use of advanced cleaning techniques during all stages of fabrication, the photolithography was done by a microelectronics industry-grade stepper and high resolution chrome mask. Also, best practices were employed during BOE wet etch and xenon diflouride dry etch used to define and isolate the silica microdisk on the silicon substrate. The 100 μm diameter microdisks show no imperfections or roughness, and provides an excellent preform for the silica microtoroid.

Next, the author aligned the CO_2 laser focal spot to the alignment mark by melting a glass slide. This alignment is performed in air, before the silicon chip with microtoroids is loaded into the vacuum chamber, because contamination occurs to anything close to the glass slide. This contamination may be due to impurities in the low quality microscope slide. In the future, higher quality glass may allow laser alignment under vacuum just prior to toroid reflow.

A single-mode optical fiber taper is pulled according to the standard taper fabrication method. As mentioned earlier, the taper length is half of the normal length to prevent leakage of the optical wave into the epoxy on the taper fork. The taper is epoxied to the taper fork, and transferred into the chamber while preserving greater than 90% transmission. The taper must have high transmission to prevent taper destruction in vacuum that can occur if the injected optical power exceeds 50 μW. While tapered fibers with micron scale diameters can carry milliwatts of optical power in air, the lack of air cooling in vacuum makes them more likely to burn. The fiber's input and output ends are routed through teflon inserts compressed by swagelock nuts, to form an UHV seal.

After the taper is placed into the chamber, the silicon chip with microdisks is fixed to its aluminum mount by SEM tape. The chip is cantilevered away from the mount, so that there is no surface immediately underneath the microdisks, preventing poor reflow quality due to reflection of unabsorbed CO_2 light. Figure 6.4 shows the silicon chip near the fiber taper inside the vacuum chamber.

The vacuum chamber is sealed with the large ZnSe window before the chamber's air is removed out by the turbo pump. After the pressure reaches 1×10^{-5} Torr, the noble diode ion pump is activated to further reduce the chamber pressure. After several hours of pumping, the turbo pump is turned off to eliminate vibrations. Then, the microdisks are moved into alignment centered on the alignment mark one by one. Each microdisk is reflowed with a single pulse from the CO_2 laser. A square pulse with 100 ms duration and 1 J of pulse energy is emitted from the laser, which is controlled by a function generator. Laser reflow of the silica microdisks produces microtoroids with

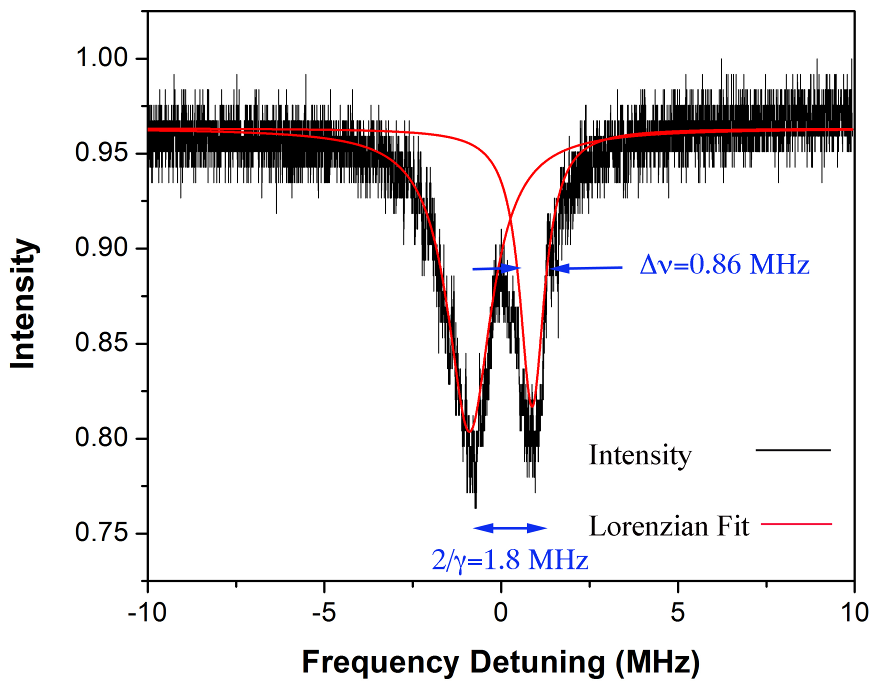

Figure 6.5. Plot of the taper transmission versus laser detuning frequency, showing a characteristic doublet mode of a microtoroid ($D = 55\ \mu$m). The resonance lineshape of each mode (black) is fit to a Lorenzian (red). The sub MHz linewidth ($\Delta\nu$) of one resonance and the splitting frequency (γ^{-1}) are also marked.

55 μm diameter.

The newly reflowed microtoroids are each analyzed in vacuum according to their cavity mode linewidths with a single frequency tunable diode laser. The highest Q measured to date in the vacuum reflow system is 2.1×10^8, determined by resonance linewidth and cavity ringdown measurements. First, the linewidth of a whispering-gallery mode is recorded in the undercoupling regime, where intrinsic loss dominates. At an input power to the taper of only 2 μW, no thermal broadening of the resonance is observed. Mode coupling due to internal scattering in the microtoroid causes previously degenerate counter-propagating modes to split in frequency. The WGM doublet resonance is shown in Figure 6.5, and is a plot of the taper transmission as a function of the diode laser detuning. The resonances are fit to a double peak Lorenzian lineshape, and the resonance linewidth is determined to be 7×10^{-15} m. Therefore, at a wavelength of 1548.1 nm, the intrinsic Q ($\lambda/\Delta\lambda$) is calculated by linewidth measurement to be 2.2×10^8.

Since the diode laser linewidth ($\approx$ 300 kHz) is of the same order as the microtoroid's cavity frequency width (800 kHz), a more accurate measurement of the microtoroid's UHQ is performed

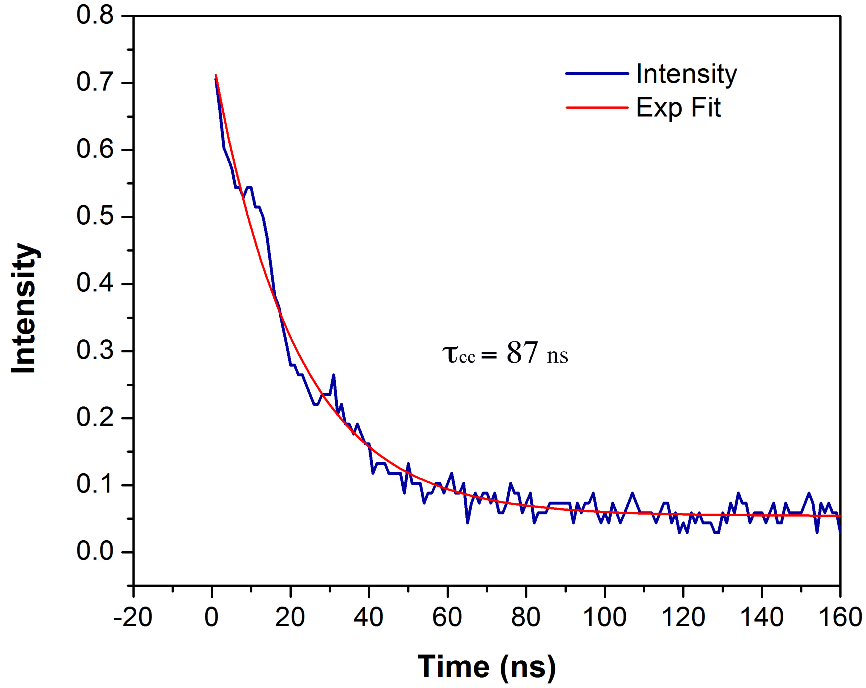

Figure 6.6. Plot showing a microtoroid cavity ringdown measurement in vacuum. The microtoroid laser cavity output is recorded after the input is gated off by a modulator. The intensity decay in time is fit to an exponential, and the cavity ringdown lifetime (τ_{cc}) at critical coupling is calculated.

by cavity ringdown. The cavity ringdown technique is described in **Chapter 2**. The taper and toroid are moved into critical coupling, exciting the toroid cavity with peak circulating power. At $t = 0$, the input laser field is switched to zero by an external phase modulator (8 ns fall time). Then, the taper transmission is recorded in time as the microtoroid cavity releases its stored energy with a measurable time constant, τ_{cc}. After an spike in transmitted power, the transmitted power decreases exponentially as shown in Figure 6.6.

The transmission is fitted to an exponential, whose time constant is the cavity lifetime $\tau_{cc} = 87$ ns. In order to accurately determine the intrinsic Q, the frequency separation of the split modes is need. The resonance linewidth measurement previously performed gives $\gamma^{-1} = 0.89$ MHz. With the critical coupling lifetime and splitting frequency now known, the intrinsic Q of this specific WGM is calculated to be 2.1×10^8 (see Equation (2.15)). The two separate methods for determining cavity Q produce nearly identical results for this vacuum annealed microtoroid.

6.7 Summary

In summary, the first toroid fabricated in the vacuum laser reflow and testing system has a maximum Q of 2.1×10^8. In the future, the laser reflow process will be improved to yield higher Q, possibly record numbers. Also, the author will study the difference in intrinsic Q between toroids manufactured in vacuum from silica grown with wet versus dry deposition methods. The upper limits of quality factor will be studied.

If microtoroid loss can be reduced, new research applications may be found in nonlinear optics, cavity quantum electrodynamics, and narrow linewidth lasers. Microtoroids combine ultra-small mode volume with ultra-high Q whispering-gallery modes, making them excellent platforms for material research and sensing. In the future, this vacuum reflow and testing system may be used for CO_2 gas sensing.

Chapter 7

Additional research into novel whispering-gallery devices

7.1 Introduction

Whispering-gallery devices (e.g., microtoroid) have additional applications aside from those previously discussed, and countless more to be discovered, due to their unique ability to confine light for long periods of time in small mode volumes. For example, the author has investigated spiral waveguides for real-time optical delay, in which WGM propagate significant distances within a small surface area. Also, the author is investigating a dual-doped Cr,Yb:SiO_2 pulsed laser design based on the microtoroid geometry. The Quantum Optics group at Caltech, led by Professor Jeff Kimble, has conducted research on cavity-atom interactions using microtoroids fabricated by the author [30, 31].

7.2 Spiral delay line

The author has conducted research on a novel on-chip optical delay line based on whispering-gallery propagation of light through a spiral waveguide. Optical delay elements are needed for all-optical packet switching for communications [112], and also for laser-based radar systems [113]. Currently, state-of-the-art optical delay lines are made from coils of optical fiber in a large package, whose fabrication is time consuming and expensive. Therefore, there is significant interest today in an on-chip lithographically fabricated real-time optical delay line with attenuation similar to optical fiber. Optical lithography offers precise control over waveguide dimensions, and allows parallel fabrication of many delay-lines with precise and possibly different time delay on the same silicon wafer.

The new optical delay line developed by the author combines two waveguide technologies. First, the waveguide is defined by two Archimedean spirals connected in the center for long-delay in a small area. A stereo-microscope image of the largest silica-on-silicon spiral waveguide the author fabricated is shown in Figure 7.1. The physical length of this spiral is 1.4 m, and the limits of the spiral fit within an area of less than 0.4 cm^2. The spiral geometry is well-recognized as an efficient way to pack long delay into a small space. A GaAs spiral waveguide for optical delay [114] and

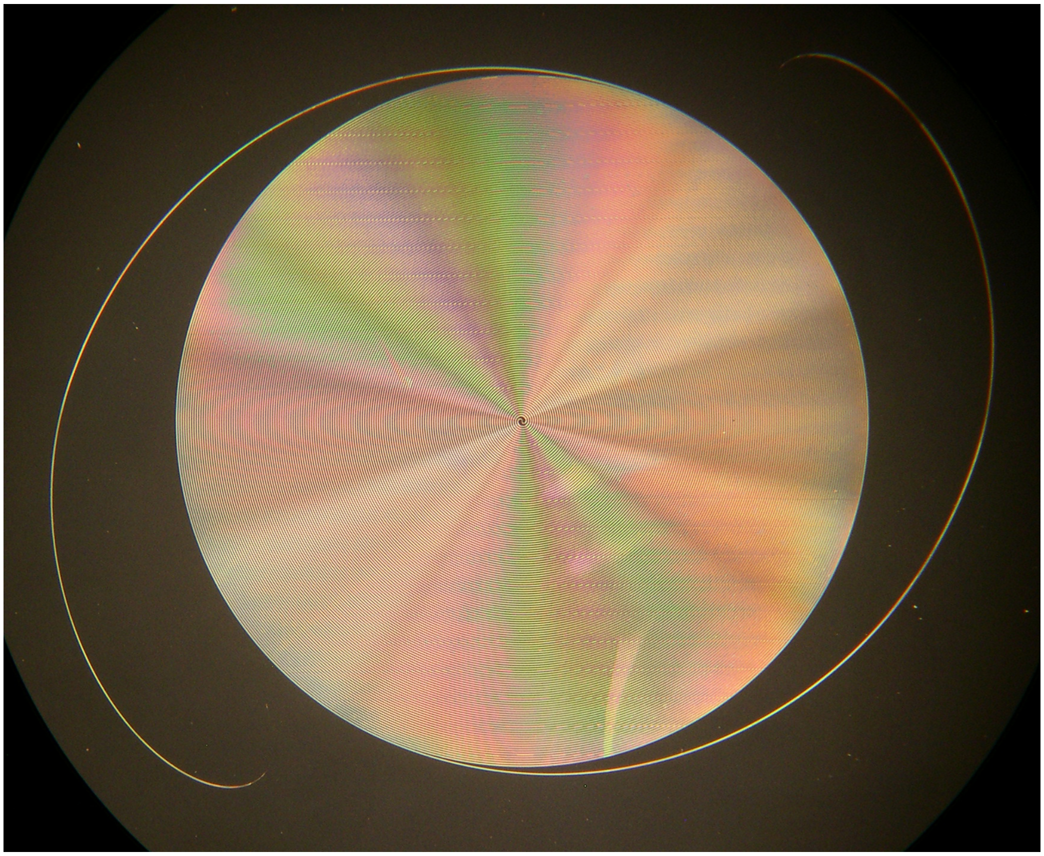

Figure 7.1. Stereo-microscope image of a large silica spiral waveguide with 1.4 m total propagation length defined within < 0.4 cm^2 area

an Er-doped Al_2O_3 spiral waveguide amplifier [115] have been reported. The largest source of loss in a twin-spiral waveguide is the center region, where the WGM must transition from clockwise to counterclockwise propagation. Here, the optical wave must move across the waveguide and switch sides, without exciting higher order modes. The author has conducted detailed simulations of the center "hand-off" region to optimize the transmission, as will be discussed in Section 7.2.1.1.

A second key technology that will enable low-loss propagation in the spiral waveguide is the silica wedge cross-section developed for UHQ silica microdisks [116]. While microtoroids can have higher Q than microdisks due to their nearly atomic smooth surface, the cavity diameter change during reflow makes integrated waveguide coupling to microtoroids difficult. Silica microdisks can be fashioned with a bevelled edge (or wedge) by control of the wet-etch chemistry. To form a wedge, the normal adhesion promoter is not applied before photoresist deposition, which allows the hydrofluoric acid to undercut the photoresist and form a low-angle bevel during the BOE etch step. An SEM micrograph of a wedged microdisk resonator is presented in Figure 7.2.

The bevel confines the whispering-gallery-mode and pushes it deep into the silica, away from lithographic roughness at the extreme edge. In this way, surface scattering is reduced and the

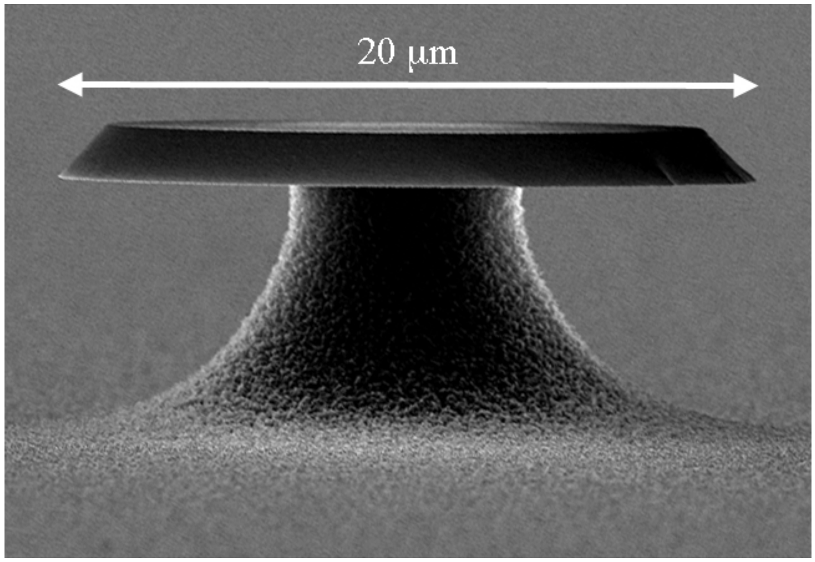

Figure 7.2. SEM image of a 20 μm diameter silica microdisk with wedge feature to confine the WGM away from surface roughness visible at the knife edge

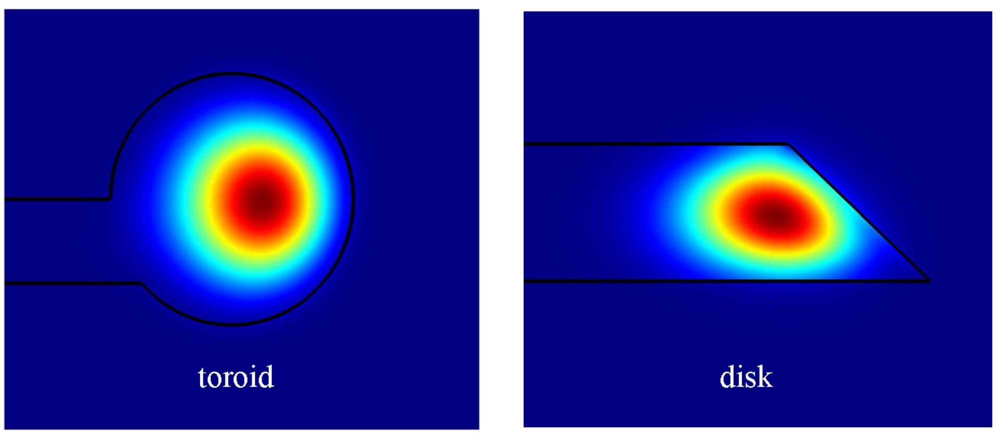

Figure 7.3. Comparison image of the WGM field pattern for a microtoroid (left) and a wedged microdisk (right). The WGM is confined further away from the extreme edge in the microdisk.

microdisk cavity Q increases. The mode confinement caused by the bevel silica surface is illustrated in Figure 7.3.

To illustrate the benefit of the silica bevel, Kippenberg demonstrated a wedged microdisk with Q as high as 6×10^7 [116], a significant improvement in Q over the normal microdisk Q (1×10^6). The effective waveguide loss for a microdisk resonator with $Q = 6 \times 10^7$ is 4×10^{-3} dB/cm, compared to silica fiber's intrinsic loss of 2×10^{-6} dB/cm. Clearly, there is room for improvement in wedged WGM propagation loss in silica, which can be achieve with lower index contrast cladding and higher purity silica deposition by flame hydrolysis. But, assuming the worst case scenario in which the wedged waveguide loss is not reduced, a 3 m long spiral can be fabricated in a 1 cm^2 area with only 1 dB of transmission loss.

7.2.1 Spiral waveguide design

A spiral with any number of total turns and turn pitch can be designed with a Matlab program the author wrote. The spiral consists of two Archimedean spiral arms, which are joined in the center by a custom transition region where the optical wave reverses circulation direction. Archimedean spirals were chosen for their smoothness and simplicity. The functional equation that generates an Archimedean spiral is easily written in polar coordinates.

$$r(\theta) = a \pm b\theta \tag{7.1}$$

Parameter a controls the starting position of the spiral by rotating the spiral around the origin, and parameter b determines the distance between successive turnings. One arm of an Archimedean spiral with three complete rotations is shown in Figure 7.4.

If two Archimedean spiral arms (one positive, one negative) are simply joined by brute force in the center, then the waveguide that results will have significant loss due to the severe bending. Alternatively, a custom center hand-off region that connects the two opposite arms smoothly is designed in Matlab.

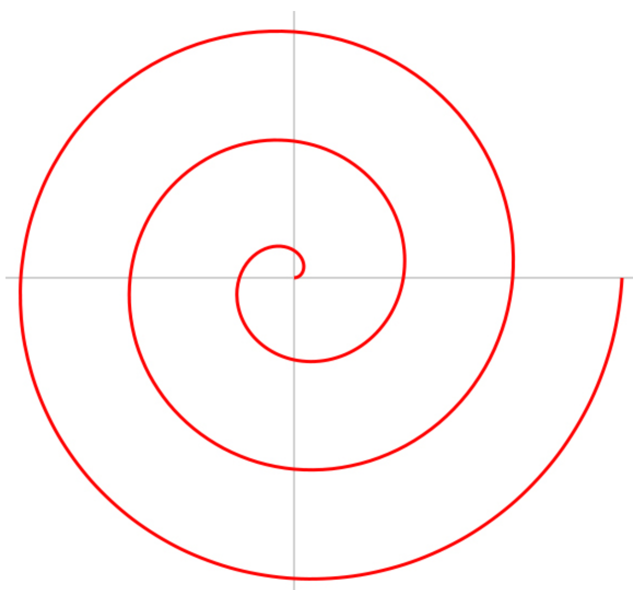

Figure 7.4. Single Archimedean spiral with three rotations; two arms are joined to form the complete spiral geometry of this work.

7.2.1.1 Spiral center transition

The center transition region (hand-off) must guide the light propagating in the positive spiral arm (clockwise rotation), into the negative spiral arm where the light will propagate in the counterclockwise direction. This transition region is most simply implemented in a smooth s-shaped curve. But, the curvature of the s-bend can follow any type of function, for instance sinusoidal or circular to name just two. The optimum shape will be determined by final transmission through the hand-off region.

In order to quantify the transmission loss through different s-bend designs, the author conducted simulations of the transmission with the commercial BeamPROP software (RSoft). BeamPROP is a waveguide design tool based on the Beam Propagation Method (BPM), and is capable of performing 3D simulations. Applied to the spiral waveguide, the simulation calculates the percentage of power that is transmitted from a single-mode whispering-gallery mode in one arm into the symmetric single mode in the arm. First, the lowest-order WGM field distributions of both positive and negative curvature are determined with the FEM solver. The geometric cross-section of the spiral waveguide is a trapezoid shape, shown with the fundamental WGMs for positive and negative curvature in Figure 7.5. The bottom width of the waveguide is 8 μm and the bevel angle is 45°.

Then, the positive curvature end of the s-bend waveguide is excited with the exact field distribution of an incident optical field from the positive spiral arm. Next, the optical field is propagated through the s-bend curve being studied. At the output of the negative curvature end of the s-curve, an overlap integral is computed of the optical field that passes through the s-bend and the single-mode WGM field that will propagate through the negative arm of the spiral. The value of this

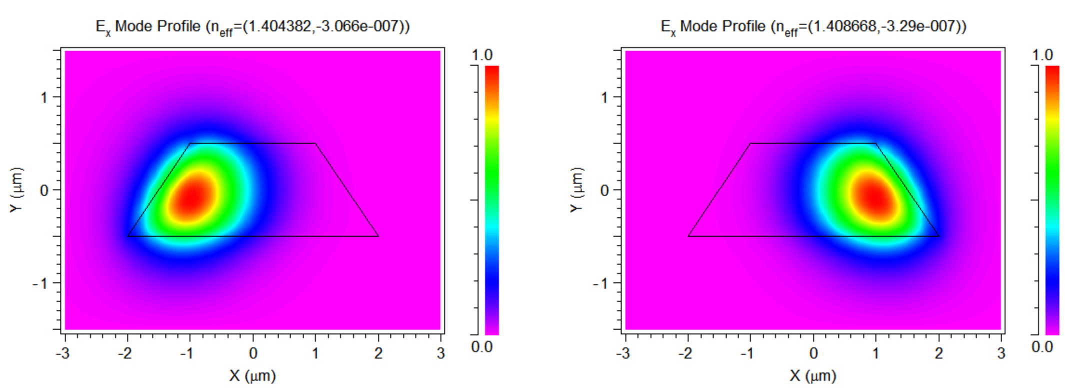

Figure 7.5. Field distributions of negative (left) and positive (right) spiral spatial modes. The field profiles are calculated by FEM, and show the effect of waveguide curvature on the mode position in the cross-section view.

integral is the fraction of incident power that actually couples from a single mode in the positive spiral arm into the single mode of the negative arm after passing through the center transition region.

Circular s-curves were studied through beam propagation simulation as described above, since they could be easily implemented into the software. The s-curve consists of two quarter circles (20 μm radius of curvature) with opposite curvature, connected at their ends. For optimum transmission, the waveguide should be close to single mode in the center. Also, the center region must be undercut completely, not supported by a silicon wall, otherwise the optical radiation traveling in silica will leak out into the silicon (higher refractive index). But, the main spiral cannot be made with single-mode width, since the spiral must be kept flat in one plane by the silicon support. Therefore, a symmetric linear taper of the waveguide width from 4 to 2 μm is included on both sides of the s-bend design. At the ends of the s-bend, the waveguide cross-section dimensions are identical to the trapezoid shape used for the FEM solver. But, the waveguide tapers down to a smaller width in the center for increased transmission.

Initially, simulations of the s-bend transmission were conducted with no horizontal offset at the center of the quarter circles. However, with no offset, the maximum transmission was only 61%. Previous work on s-bends in optical modulators determined that a horizontal offset reduces transmission losses in bent waveguides [117]. A physical horizontal offset was inserted between the two quarter circles, and its value was optimized for highest transmission through the transition region. For an s-curve with dimensions of $R = 20\ \mu$, $2 \leq w \leq 4$, and thickness $t = 2\ \mu$m, the optimum offset for single-mode transmission of 1550 nm light is $\Delta x = 1.8\ \mu$m. The final transmission through the s-bend waveguide with these parameters is 88%. Figure 7.6 is a plot of the s-bend design showing the waveguide width taper and horizontal offset in the center. Future research into other transitional functions and parameters will increase the transmission. Perhaps a true single-mode center hand-off can be designed and fabricated for higher transmission. The current design presented did not have a single-mode waveguide element, instead it relied on offset and tapering to prevent the single WGM from coupling into other modes.

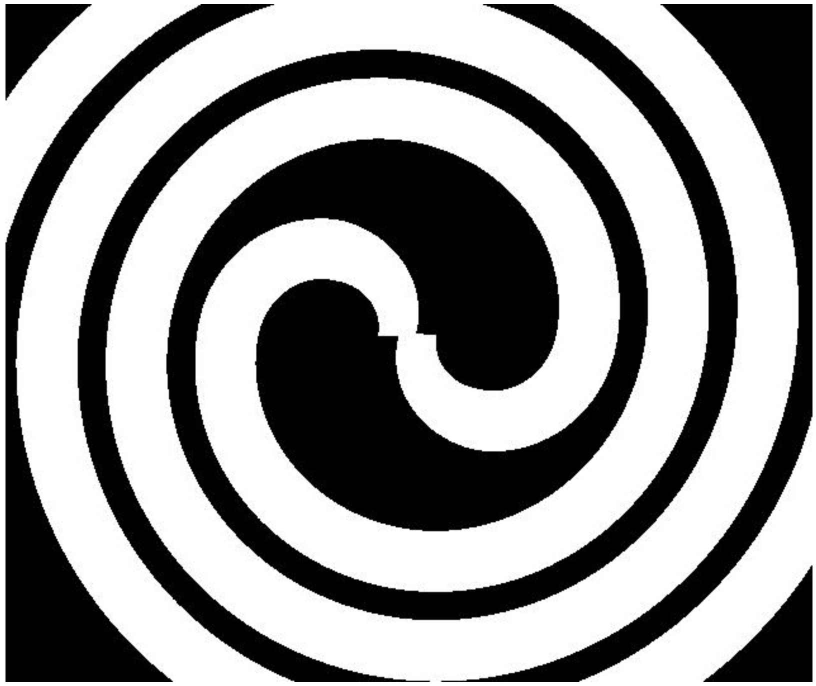

Figure 7.6. Plot of the center s-bend design for high transmission in a spiral waveguide

7.2.2 Spiral waveguide fabrication

Several different spiral waveguides are fabricated to demonstrate the device and measure its transmission of light. Standard photolithography and etching techniques are utilized, similar to the fabrication of microtoroids. First, a layer of photoresist is spin coated onto a silicon wafer with 2 μm thermal oxide on top, using HMDS to increase the adhesion and prevent over etching of the narrow hand-off region in the spiral center. The spiral pattern designed using Matlab and BeamPROP is transferred into the photoresist with an industry grade wafer stepper, providing the highest resolution possible in our facilities. After the exposed photoresist is removed by developer, the spiral pattern is transferred into the fused silica layer by BOE wet etch. The etching time is carefully controlled to produce the 45° bevel as designed, without over etching the center s-bend region. Finally, a XeF_2 dry etch completely undercuts the silica s-bend region in the spiral center, and leaves the spiral waveguide supported by thin rails of silicon. An SEM image of the center portion of one completed spiral is shown in Figure 7.7. The center hand-off region with the width tapering and center offset is visible.

The silicon wafer was cleaved directly through a spiral waveguide, revealing the sidewall bevel and cross-section of the wedged waveguide supported by silicon (Figure 7.8).

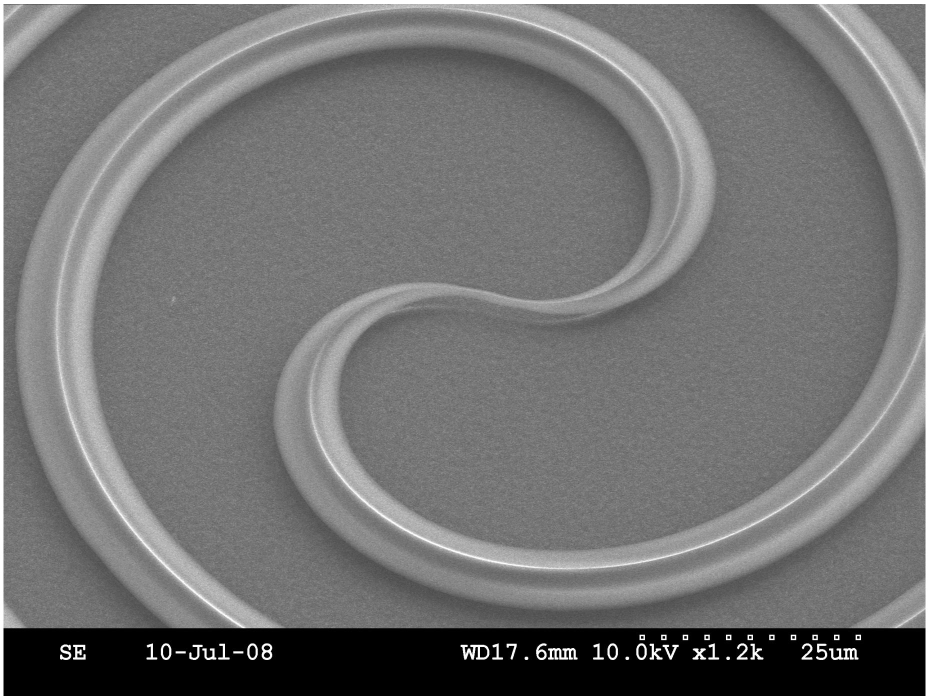

Figure 7.7. SEM image of the center portion of one completed silica on silicon spiral waveguide. Notice that the center transition region of the spiral is completely undercut.

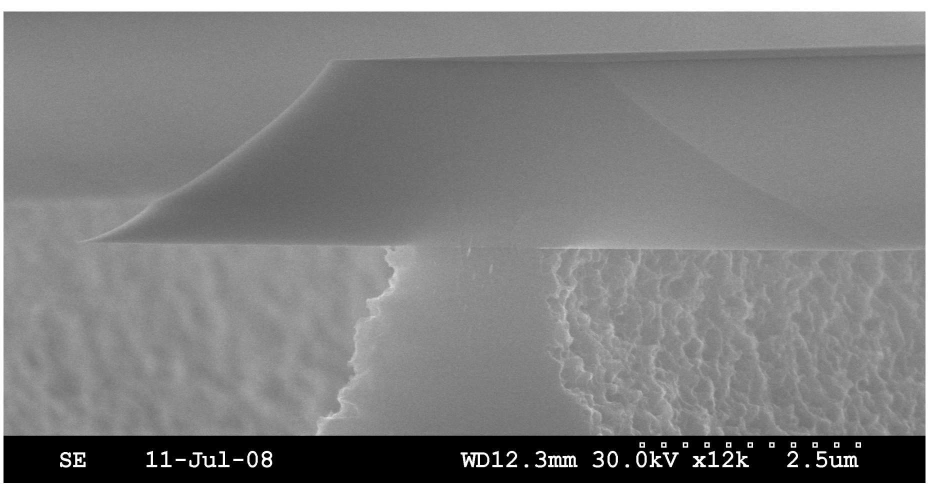

Figure 7.8. SEM image of a cleaved spiral showing the waveguide cross-section with sidewall bevel and silicon support

7.2.3 Spiral waveguide measurement

In addition to the larger spirals fabricated for physical demonstration (see Figure 7.1), smaller single-turn spirals are made for measurement of the transmission loss of the s-bend hand-off region. The largest source of loss at this stage is believed to be due to the center region. In order to perform accurate insertion loss measurements of the spiral waveguide, two fiber tapers are pulled simultaneously. A dual-fiber taper drawing system is constructed that pulls two tapers over a single hydrogen flame, similar to that used for dual taper testing of a microtoroid four-port coupler [107]. To make two quasi-identical tapers, the flame location and hydrogen gas flow are carefully optimized. After significant trial and error, dual tapers separated by 0.5 mm are fabricated with high transmission and nearly identical diameters.

The spiral waveguide is elevated until it is in close contact with both tapers, the spiral waveguide outer diameter is 100 μm. The spiral position is adjusted using nanopositioning stages, one taper is fixed in place, and the second taper is controlled by a probe attached to the taper. To make an accurate measurement of the transmission through the short spiral, the transmission of each taper is recorded. The input fiber is aligned to the input arm of the spiral at the outside of the bevel. This spiral is moved until maximum extinction is achieved, indicating maximum power transfer into the spiral waveguide. The output taper is precisely moved until output radiation is measured at the end of the fiber. The output fiber radiation is the light that couples into the spiral input arm, propagates through the spiral (including the center hand-off region), and couples out into the output fiber. A microscope image of the short spiral and two fiber tapers is shown in Figure 7.9. The ratio of output power to input power is computed, and then adjusted for taper losses. This final value is the percentage of light that is coupled through the spiral waveguide, and contains any taper-spiral coupling losses. The highest transmission measured for the first short spiral is 4 %, indicating that significant loss accumulates either in the hand-off region or taper coupling, or both.

In the future, numerous different short spirals will be tested to determine the best s-bend design, quantified by the spiral transmission. Then, larger spirals with quantified lengths and identical center regions will be tested to determine the transmission loss of the spiral arms themselves, independent of the center transition region.

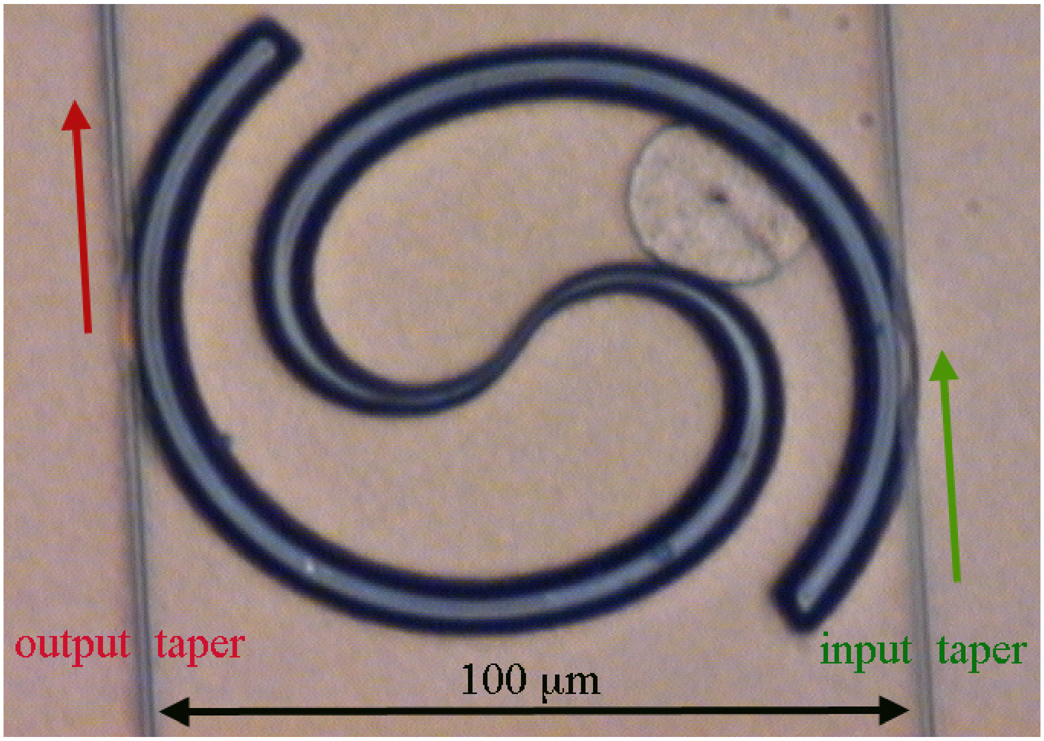

Figure 7.9. Top view of the one-turn two arm spiral with dual fiber taper coupling for transmission measurement. The outer diameter of the spiral is 100 μm.

7.3 Short-pulse microcavity laser

The Yb:SiO_2 microtoroid sol-gel lasers presented in Chapters 3 and 4 normally operated with continuous output power. However, unstable 100 ns duration pulses were observed in higher ytterbium concentration toroid lasers as discussed in Section 3.6.4. A stable short-pulse microcavity laser has never been demonstrated, and is an interesting field of research.

7.3.1 Laser concept

The author has developed a new short-pulse microcavity laser concept made possible by flexible doping of solgel silica. The short pulse laser operates by passive Q switching in a dual doped Cr,Yb:SiO_2 microtoroid. The microtoroid laser can be easily fashioned according to the solgel fabrication method, by including chromium nitrate and ytterbium nitrate in the solution before the main chemical reaction occurs. The author gained experience in short pulse lasers with his work developing a Yb:YAG microchip laser oscillator with a Cr:YAG passive Q switch [52].

Q switched lasers produce short pulses due to repeated modulation of the cavity loss or gain. This dual doped laser receives gain from the ytterbium ions, and time-dependent loss from the chromium ions. Chromium (Cr^{4+}) ions have an intensity dependent cross-section of absorption

(σ). The ground state cross-section of chromium is $\sigma_g = 4 \times 10^{-20}$ cm^{-2}, and the excited state cross-section is $\sigma_e = 7 \times 10^{-21}$ cm^{-2}. Inside the laser microcavity, the absorption loss caused by Cr^{4+} ions in the ground state prevent laser emission at low intracavity intensities. However, the constant-power pump light linearly increases the stored energy in the ytterbium ions, and hence the intracavity intensity. Once the intensity reaches a threshold value, the chromium ions transition from the ground to excited state, and their absorption loss drops. At this point, the cavity gain (from Yb) is greater than the cavity loss (from Cr, coupling, scattering, etc.) and a giant pulse is emitted from the microtoroid cavity laser as the ytterbium ions coherently decay by stimulated laser emission.

7.3.2 Pulsed laser modeling

A numerical model of the short-pulse Cr,Yb:SiO_2 laser was implemented by the author in Matlab to research the design considerations and predict the laser performance. This laser model builds on the short-pulse laser model developed by Dong et al. for Cr,Yb:YAG microdisk lasers [118]. The initial (N_i), threshold (N_t), and final (N_f) ytterbium population inversion densities are calculated by solving the laser rate equations. Then, the laser pulse energy (E_p), peak pulse power (P_{peak}), and pulse duration (τ_p) are computed as,

$$\begin{aligned}
P_{th} &= \frac{N_i A l h\nu}{\tau_{Yb}} \\
E_p &= \frac{h\nu A}{4\sigma} ln\left(\frac{1}{R}\right) ln\left(\frac{N_i}{N_f}\right) \\
P_{peak} &= \frac{h\nu A l}{2t_r} ln\left(\frac{1}{R}\right)\left[N_i - N_{th} - N_{th} ln\left(\frac{N_i}{N_f}\right)\right] \\
\tau_p &\approx \frac{E_p}{P_{peak}}
\end{aligned} \tag{7.2}$$

where A is the laser cavity mode area, $R = 1 - T$ is the round trip total cavity loss, t_r is the cavity round trip time, and σ is the stimulated emissions cross section of ytterbium.

Extensive simulations were conducted to elucidate the performance of the Cr,Yb doped silica microtoroid laser. The final configuration under consideration is a microtoroid cavity with 50 μm diameter, 5×10^{18} cm^{-3} Cr^{4+} concentration, and 5×10^{19} cm^{-3} Yb^{3+} concentration. The pulsed laser model just described predicts that the Q switched microcavity laser will generate a pulse train with 1 ns pulse duration, 100 pJ pulse energy, and 1 MW/cm^2 peak intensity. This laser is also expected to have a pump threshold of 1 μW, easily reached with existing tunable semiconductor diode lasers. Therefore, it is expected that such a chromium and ytterbium doped silica microtoroid laser, fabricated by sol-gel, will produce stable laser pulses.

The microcavity laser pulse duration (τ_p) is inversely dependent on the chromium concentration (N_{Cr}) as shown in Figure 7.10. Laser pulses as narrow as 10 ps can be generated by increasing

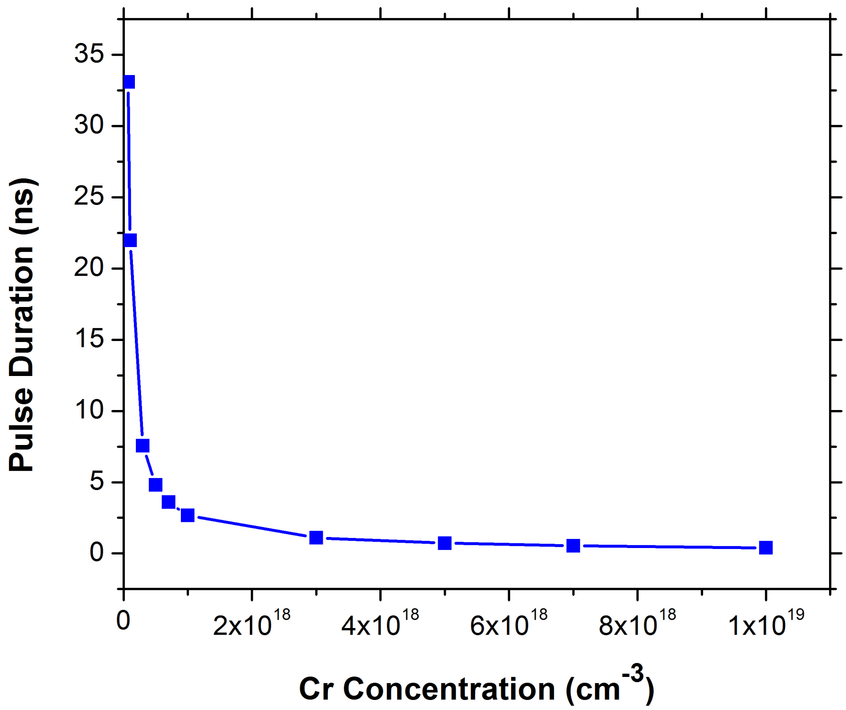

Figure 7.10. Plot of the Cr,Yb:SIO_2 microtoroid pulse duration as a function of Cr^{4+} concentration. This curve was generated for a fixed ytterbium concentration of $N_{Yb} = 5 \times 10^{19}$ cm^{-3} and 50 μm toroid diameter.

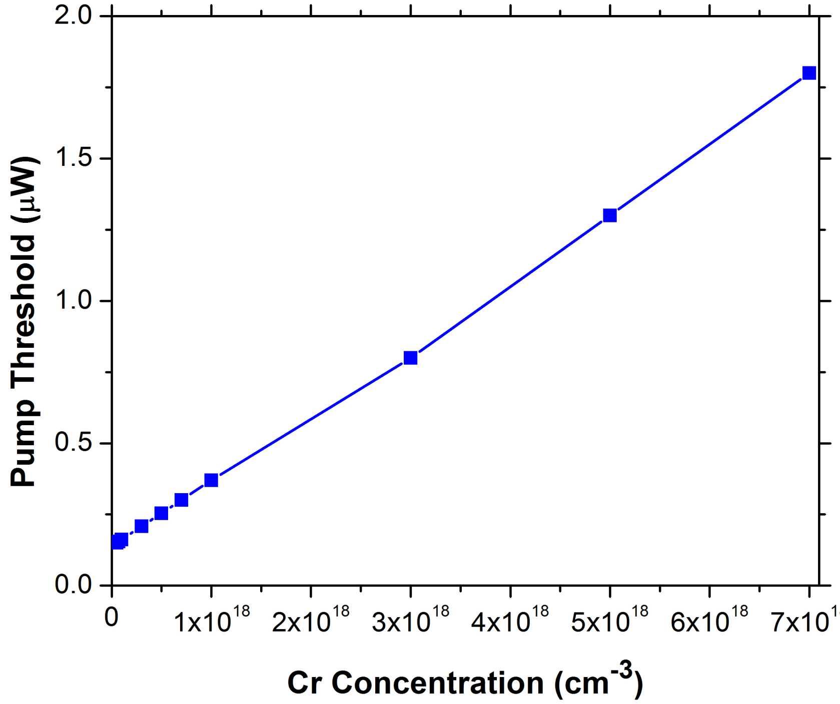

Figure 7.11. Plot of the pulsed laser threshold as a function of Cr^{4+} concentration for a 50 μm toroid

the chromium concentration, but will require higher pump power. Simulation also demonstrates in Figure 7.11 the linear dependence of laser pump threshold on chromium concentration.

A short-pulse laser, like the one designed here, will offer new areas of scientific research in microcavities. For instance, a pulsed laser can be used as a light source for on-chip optical communication. Also, the laser pulse train is very sensitive to any sources of loss, and may find application as a particle or biological sensor. Now, it is up to future research to experimentally demonstrate this novel passively Q switched laser and apply it to new problems.

7.4 Microtoroids for atom cavity experiments

The author collaborated with the Kimble research group at Caltech, by fabricating UHQ and ultra-low mode volume microtoroids for their cavity quantum electrodynamics (cQED) experiments. Utilizing these toroids, a novel photon turnstile and a high-efficiency single-photon router were demonstrated. Cavity QED is the study of the interaction between light confined in a cavity and atoms or other particles, for situations when the quantum nature of photons is evident. In principle, cQED research could be used to construct a quantum computer.

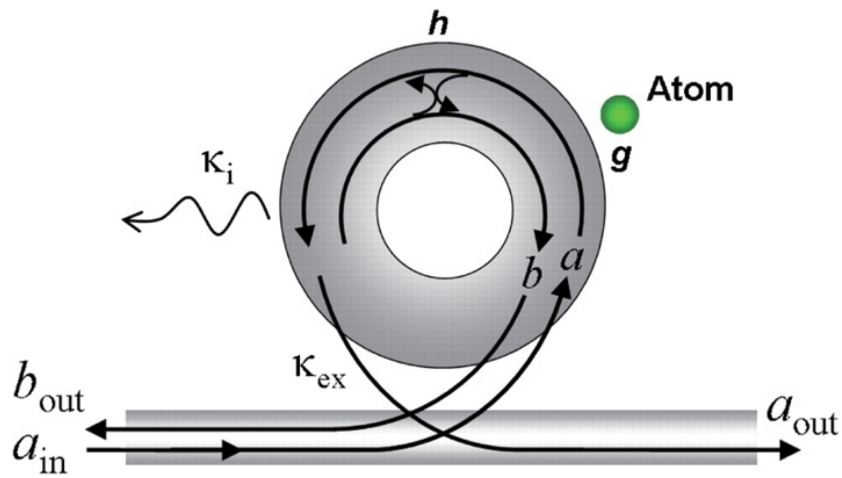

Figure 7.12. Schematic of microtoroidal resonator and fiber taper coupler. A cesium atom interacts at rate g with the evanescent fields of two cavity modes (a,b), which are coupled by scattering.

7.4.1 Cavity quantum electrodynamics

The strong coupling rate, g, between an electromagnetic field and an atomic system can be defined in terms of the cavity and atom parameters.

$$g = \gamma_{\perp}|E|\sqrt{V_a/V_m} \tag{7.3}$$

Here, $\gamma_{\perp}$ is the transverse atomic dipole transition rate, $|E|$ is the cavity's electric field strength at the atom location, V_a is the atom interaction volume, and V_m is the cavity mode volume. Strong coupling between a microtoroid and a cesium atom was shown by Aoki[17]. To satisfy the strong coupling condition, the rate of atom to cavity coupling must exceed all other dissipation mechanisms, therefore $g >> (\kappa, \gamma_{\perp}, T^{-1})$. The toroid cavity decay is defined as $\kappa = \frac{\pi c}{\lambda Q}$. Also, T is the length of time that the cavity and atom are strongly coupled.

Since photons have small intracoupling cross sections, a material system must be used for their interactions. Still, typical materials produce photon to photon coupling rates that are orders of magnitude too small for significant dynamics with photon pairs. But, in cavity quantum electrodynamics (cQED), strong interactions between single photons of light and matter have been demonstrated, including single atoms coupled to optical resonators, and quantum dots paired with photonic bandgap cavities.

Photon blockade is observed, in which photon transport is regulated dynamically by the conditional state of one intracavity atom. As illustrated in Figure 7.12, an atom interacting with the fields of a microtoroidal resonator regulates the photon statistics of light transmitted and reflected by the resonator [17]. This control is made possible by the interference of the directly transmitted optical field, the intracavity field, and the polarization field radiated by the atom. The quantum emission of the single atom provides nonlinearity, required for the turnstile behavior. The presence of a photon in the forward transmission causes any subsequent photons to be directed back towards the pump source.

The observation of photon anti-bunching relied on measurements of photon correlations based on the normalized intensity correlation function $g_F^{(2)}(\tau)$ for the forward-propagating transmitted light [119]. The incident field has $g_F^{(2)}(\tau) = 1$, corresponding to a Poisson distribution for photon number independent of time delay τ. An ideal photon turnstile would achieve $g_F^{(2)}(0) = 0$ in correspondence to the state of a single photon. More generally, $g_F^{(2)}(0) < 1$ represents a nonclassical effect with the variance in photon number reduced below that of the incident field. The observation $g_F^{(2)}(0) < g_F^{(2)}(\tau)$ represents photon anti-bunching−photons are transported one by one through the turnstile.

7.4.2 Experimental details

In the photon turnstile experiment, individual cesium atoms are dropped vertically through the evanescent field of the resonator. The author fabricated the toroidal resonator from SiO_2 on a silicon chip [10], had major diameter $D \approx 25\,\mu$m and minor diameter $d \approx 6\,\mu$m. The microtoroid and single-mode fiber taper waveguide are located inside an ultrahigh vacuum chamber.

With the taper and toroid in critical coupling, the transmitted power is sent to two single-photon counters, with the outputs from these detectors being time-stamped and stored for time bins for each time value. Then, the cross correlation is calculated from the time-stamped photon counting records.

7.4.3 Demonstration of anti-bunching and sub-Poissonian statistics

The intensity correlation function exhibits clear anti-bunching and sub-Poissonian photon statistics, demonstrated by a dip in the correlation function near $t = 0$. The efficiency of single photons is measured as high as 25% during single-atom transit events. Because the toroidal resonators are lithographically fabricated with input-output coupling via optical fiber, this experiment is a key step into the quantum domain towards implementing compact atom-cavity systems.

7.4.4 High efficiency single photon routing

The author also fabricated a small diameter, 20 μm, microtoroid cavity that showed higher efficiency routing of single photons as a part of an atomic system [31]. Single photons from a coherent laser input were efficiently directed to a separate output by way of a fibercoupled microtoroidal cavity interaction with individual cesium atoms. By operating in an overcoupled regime for the input-output to a tapered fiber, this system works as a quantum router with high efficiency. Single photons are reflected back towards the input, and excess photons are transmitted, as proven by observations of photon antibunching for the reflected light. The single photons are directed to a separate output with an efficiency of $\xi \approx 0.6$.

Detection of a first photon for the reflected field forces the cesium atom into its ground state, which prevents the detection of a second photon [30, 120]. Therefore, the reflected light shows sub-Poissonian photon statistics and photon antibunching. Single photons are reflected the excess photons are transmitted into the forward field. In the future, the routing efficiency can approach $\xi > 0.999$ through use of microtoroids with smaller major diameter and higher intrinsic q factor [11, 121].

7.4.5 Fabrication of small mode volume UHQ microtoroids for cQED research

The author fabricated small-mode volume microtoroids for the atom and cavity experiments detailed above. These microtoroids have a major diameter (D) of only 25 μm. To create these small toroids, small silica microdisks, 40 μm diameter, were first made by photolithography and wet etching. The XeF_2 etch reduced the silicon pillar diameter to approximately 10 μm. Then, the microdisks were selectively reflowed using a single 100 ms duration CO_2 laser pulse. The final microtoroid major diameter is 20–25 μm, the minor diameter is 4–5 μm. The fundamental whispering-gallery mode volume, V_m, is estimated to be only 40 μm^{-3}. These small mode volume toroids can provide a very high atom-cavity coupling rate, g, due to the inverse relationship between the coupling rate and cavity mode volume (see Equation (7.3)).

7.4.6 Vacuum reflow of microtoroids for cQED

In the photon turnstile experiment, the microtoroid quality factor was modest at $Q = 3 \times 10^6$. For future work, higher Q is required to meet the strong-coupling condition and allow for more advanced quantum optics research. The author's work on vacuum reflow of microtoroids, discussed in **Chapter 5**, will produce higher quality factors, theoretically up to $Q = 1 \times 10^{10}$. The increase in the microtoroid cavity Q leads to an important reduction in the critical atom number, or the number of Cesium atoms required to affect the optical cavity [11]. In the future, microtoroid reflow and quantum optics research may be performed in a single vacuum chamber, leveraging ultra-high Q microtoroids for new research applications.

7.5 Summary

In this chapter, several additional research projects involving novel whispering-gallery devices were discussed. An on-chip, low-loss spiral waveguide for optical delay was investigated. Beam propagations simulated the loss through the center transition region, and optimized the design for low loss propagation. Also, complete spiral waveguides were designed in Matlab and fabricated. Secondly, a dual-doped Cr,Yb silica microlaser was designed, and simulations predict sub nanosecond pulse widths. Finally, the author's work on ultra-low mode volume microtoroids for cQED experiments was presented. These projects illustrate the flexibility and unique characteristics of whispering-gallery optical waveguides.

Bibliography

[1] J. Lott, N. Ledentsov, V. Ustinov, N. Maleev, A. Zhukov, A. Kovsh, M. Maximov, B. Volovik, Z. Alferov, and D. Bimberg, "InAs-InGaAs quantum dot VCSELs on GaAs substrates emitting at 1.3μm," Electronics Letters **36**(16), 1384–1385 (2000). 1

[2] J. Kringlebotn, J. Archambault, L. Reekie, and D. Payne, "Erˆ 3+: Ybˆ 3+-codoped fiber distributed-feedback laser," Optics Letters **19**(24), 2101–2103 (1994). 1

[3] S. Qian, J. Snow, H. Tzeng, and R. Chang, "Lasing droplets: highlighting the liquid-air interface by laser emission," Science **231**(4737), 486–488 (1986). 1

[4] B. Little, J. Foresi, G. Steinmeyer, E. Thoen, S. Chu, H. Haus, E. Ippen, L. Kimerling, and W. Greene, "Ultra-compact Si-SiO 2 microring resonator opticalchannel dropping filters," IEEE Photonics Technology Letters **10**(4), 549–551 (1998). 1

[5] V. Braginsky, M. Gorodetsky, and V. Ilchenko, "Quality-factor and nonlinear properties of optical whispering-gallery modes," Physical Review A **137**(7-8) (1989). 1

[6] M. Gorodetsky, A. Savchenkov, and V. Ilchenko, "Ultimate Q of optical microsphere resonators," Optics Letters **21**(7), 453–455 (1996). 1, 12, 13, 67, 70

[7] D. Vernooy, V. Ilchenko, H. Mabuchi, E. Streed, and H. Kimble, "High-Q measurements of fused-silica microspheres in the near infrared," Optics Letters **23**(4), 247–249 (1998). 1, 67

[8] M. Cai, O. Painter, and K. Vahala, "Observation of critical coupling in a fiber taper to a silica-microsphere whispering-gallery mode system," IEEE Photonics Technology Letters **85**, 74 (1999). 1, 35, 42

[9] T. Kippenberg, J. Kalkman, A. Polman, and K. Vahala, "Demonstration of an erbium-doped microdisk laser on a silicon chip," Physical Review A **74**, 051,802 (2006). 1, 12, 50, 54

[10] D. Armani, T. Kippenberg, S. Spillane, and K. Vahala, "Ultra-high-Q toroid microcavity on a chip," Nature **421**(6926), 925–928 (2003). 1, 5, 10, 23, 44, 50, 95

[11] S. Spillane, T. Kippenberg, K. Vahala, K. Goh, E. Wilcut, and H. Kimble, "Ultrahigh-Q toroidal microresonators for cavity quantum electrodynamics," Physical Review A **71**(1) (2005). 1, 56, 59, 96

[12] T. Kippenberg, S. Spillane, D. Armani, and K. Vahala, "Ultralow-threshold microcavity Raman laser on a microelectronic chip," Optics Letters **29**(11), 1224–1226 (2004). 1, 2, 16, 67

[13] S. Spillane, T. Kippenberg, O. Painter, and K. Vahala, "Ideality in a fiber-taper-coupled microresonator system for application to cavity quantum electrodynamics," Physical Review Letters **91**(4), 35 (2003). 2, 13, 28, 35, 42, 69

[14] T. Kippenberg, S. Spillane, and K. Vahala, "Kerr-nonlinearity optical parametric oscillation in an ultrahigh-Q toroid microcavity," Physical Review Letters **93**, 83,904–83,904 (2004). 2

[15] T. Carmon and K. Vahala, "Visible continuous emission from a silica microphotonic device by third-harmonic generation," Nature Physics **3**(6), 430–435 (2007). 2

[16] H. Rokhsari, T. Kippenberg, T. Carmon, and K. Vahala, "Radiation-pressure-driven micro-mechanical oscillator," Optics Express **13**(14), 5293–5301 (2005). 2

[17] T. Aoki, B. Dayan, E. Wilcut, W. Bowen, A. Parkins, T. Kippenberg, K. Vahala, and H. Kimble, "Observation of strong coupling between one atom and a monolithic microresonator," Nature **443**, 671–674 (2006). 2, 94

[18] A. Armani, R. Kulkarni, S. Fraser, R. Flagan, and K. Vahala, "Label-free, single-molecule detection with optical microcavities," Science **317**(5839), 783 (2007). 2, 41

[19] E. Ostby, L. Yang, and K. Vahala, "Ultralow-threshold Yb^ 3+: SiO_2 glass laser fabricated by the solgel process," Optics Letters **32**(18), 2650–2652 (2007). 2, 26, 41, 67

[20] L. Yang, T. Carmon, B. Min, S. Spillane, and K. Vahala, "Erbium-doped and Raman microlasers on a silicon chip fabricated by the sol–gel process," Applied Physics Letters **86**, 091,114 (2005). 2, 23, 24, 25, 39, 41, 67

[21] B. Min, T. Kippenberg, L. Yang, K. Vahala, J. Kalkman, and A. Polman, "Erbium-implanted high-Q silica toroidal microcavity laser on a silicon chip," Physical Review A **70**, 033,803 (2004). 2, 28, 29, 36, 47

[22] G. Hale and M. Querry, "Optical constants of water in the 200-nm to 200-μm wavelength region," Applied Optics **12**(3), 555–563 (1973). 2, 39, 42, 44, 70

[23] E. P. Ostby and K. J. Vahala, "Yb-doped glass microcavity laser operation in water," Optics Letters **34**(8), 1153–1155 (2009). 2

[24] W. Barnes, A. Dereux, and T. Ebbesen, “Surface plasmon subwavelength optics,” Nature **424**(6950), 824–830 (2003). 3, 50, 64

[25] S. Maier, P. Kik, H. Atwater, S. Meltzer, E. Harel, B. Koel, and A. Requicha, “Local detection of electromagnetic energy transport below the diffraction limit in metal nanoparticle plasmon waveguides,” Nature Materials **2**(4), 229–232 (2003). 3, 50, 64

[26] E. Ozbay, “Plasmonics: Merging photonics and electronics at nanoscale dimensions,” Science **311**(5758), 189–193 (2006). 3, 50, 64

[27] S. Bozhevolnyi, V. Volkov, E. Devaux, J. Laluet, and T. Ebbesen, “Channel plasmon subwavelength waveguide components including interferometers and ring resonators,” Nature **440**(7083), 508–511 (2006). 3, 60, 64

[28] H. Lezec, J. Dionne, and H. Atwater, “Negative refraction at visible frequencies,” Science **316**(5823), 430 (2007). 3

[29] B. Min, E. Ostby, V. Sorger, E. Ulin-Avila, L. Yang, X. Zhang, and K. Vahala, “High-Q surface-plasmon-polariton whispering-gallery microcavity,” Nature **457**(7228), 455–458 (2008). 3, 12

[30] B. Dayan, A. Parkins, T. Aoki, E. Ostby, K. Vahala, and H. Kimble, “A photon turnstile dynamically regulated by one atom,” Science **319**(5866), 1062 (2008). 4, 67, 81, 96

[31] T. Aoki, A. S. Parkins, D. J. Alton, C. A. Regal, B. Dayan, E. Ostby, K. J. Vahala, and H. J. Kimble, “Efficient Routing of Single Photons by One Atom and a Microtoroidal Cavity,” Physical Review Letters **102**(8), 083601 (pages 4) (2009). 4, 67, 81, 95

[32] K. Vahala, *Optical microcavities* (World Scientific, 2004). 5

[33] A. Oraevsky, “Whispering-gallery waves,” Quantum Electronics **32**(5), 377–400 (2002). 5

[34] V. S. Ilchenko, A. A. Savchenkov, J. Byrd, I. Solomatine, A. B. Matsko, D. Seidel, and L. Maleki, “Crystal quartz optical whispering-gallery resonators,” Optics Letters **33**(14), 1569–1571 (2008). 5

[35] B. Min, L. Yang, and K. Vahala, “Perturbative analytic theory of an ultrahigh-Q toroidal microcavity,” Physical Review A **76**, 013,823 (2007). 6

[36] A. Yariv, *Optical Electronics* (Oxford University Press, USA, 1991). 7, 14

[37] I. Chan, K. Brown, R. Lawson, A. Robinson, Y. Ma, and D. Strembicke, “Gas phase pulse etching of silicon for MEMS with xenon difluoride,” in *1999 IEEE Canadian Conference on Electrical and Computer Engineering*, vol. 3 (1999). 12

[38] M. Hossein-Zadeh and K. Vahala, "Importance of intrinsic-Q in microring-based optical filters and dispersion-compensation devices," IEEE Photonics Technology Letters **19**(13/16), 1045 (2007). 12

[39] A. Campillo, J. Eversole, and H. Lin, "Cavity quantum electrodynamic enhancement of stimulated emission in microdroplets," Physical Review Letters **67**, 437–440 (1991). 12

[40] I. Grudinin, A. Matsko, A. Savchenkov, D. Strekalov, V. Ilchenko, and L. Maleki, "Ultra high Q crystalline microcavities," Optics Communications **265**(1), 33–38 (2006). 13

[41] J. Knight, G. Cheung, F. Jacques, and T. Birks, "Phase-matched excitation of whispering-gallery-mode resonances by a fiber taper," Optics Letters **22**(15), 1129–1131 (1997). 13

[42] A. Serpengüzel, S. Arnold, and G. Griffel, "Excitation of resonances of microspheres on an optical fiber," Optics Letters **20**(7), 654–656 (1995). 13

[43] T. Carmon, S. Wang, E. Ostby, and K. Vahala, "Wavelength-independent coupler from fiber to an on-chip cavity, demonstrated over an 850nm span," Optics Express **15**(12), 7677–7681 (2007). 13

[44] D. Weiss, V. Sandoghdar, J. Hare, V. Lefevre-Seguin, J. Raimond, and S. Haroche, "Splitting of high-Q Mie modes induced by light backscattering in silica microspheres," Optics Letters **20**(18), 1835–1837 (1995). 16

[45] T. Toyoda and M. Yabe, "The temperature dependence of the refractive indices of fused silica and crystal quartz," Journal of Physics D: Applied Physics **16**, L97–L100 (1983). 18

[46] T. Carmon, L. Yang, and K. Vahala, "Dynamical thermal behavior and thermal self-stability of microcavities," Optics Express **12**(20), 4742–4750 (2004). 18

[47] T. Kippenberg and K. Vahala, "Cavity optomechanics: back-action at the mesoscale," Science **321**(5893), 1172 (2008). 20

[48] A. Schliesser, R. Riviere, G. Anetsberger, O. Arcizet, and T. Kippenberg, "Resolved-sideband cooling of a micromechanical oscillator," Nature Physics **4**(5), 415–419 (2008). 20

[49] D. Nikogosyan, *Properties of optical and laser-related materials. A handbook* (2003). 20

[50] L. Wu and A. Knoesen, "Absolute absorption measurements of polymer films for optical waveguide applications by photothermal deflection spectroscopy," Journal of Polymer Science Part B: Polymer Physics **39**(22), 2717–2726 (2001). 20

[51] L. He, Y. Xiao, C. Dong, J. Zhu, V. Gaddam, and L. Yang, "Compensation of thermal refraction effect in high-Q toroidal microresonator by polydimethylsiloxane coating," Applied Physics Letters **93**, 20 (2008). 20

[52] E. Ostby, J. Fukumoto, R. Stultz, S. Matthews, and D. Filgas, “Short pulse and high repetition rate Q-switched Yb: YAG microchip laser,” **5707**, 72 (2005). 23, 90

[53] P. Lacovara, H. Choi, C. Wang, R. Aggarwal, and T. Fan, “Room-temperature diode-pumped Yb: YAG laser,” Optics Letters **16**(14), 1089–1091 (1991). 23, 26

[54] A. Asseh, H. Storoy, J. Kringlebotn, W. Margulis, B. Sahlgren, S. Sandgren, R. Stubbe, and G. Edwall, Electronics Letters **31**(12), 969–970 (1995). 23, 26, 39

[55] L. Hench and J. West, “The sol-gel process,” Chem. Rev **90**(1), 33–72 (1990). 23, 24

[56] C. Li, J. Chisham, M. Andrews, S. Najafi, J. Mackenzie, and N. Peyghambarian, “Sol-gel integrated optical coupler by ultraviolet light imprinting,” Electronics Letters **31**(4), 271–272 (1995). 23

[57] J. Meegan, A. Aggeli, N. Boden, R. Brydson, A. Brown, L. Carrick, A. Brough, A. Hussain, and R. Ansell, “Designed Self-Assembled &bgr;-Sheet Peptide Fibrils as Templates for Silica Nanotubes,” Advanced Functional Materials **14**, 31–37 (2004). 23

[58] X. Orignac, D. Barbier, X. Min Du, R. Almeida, O. McCarthy, and E. Yeatman, “Sol–gel silica/titania-on-silicon Er/Yb-doped waveguides for optical amplification at 1.5 μm,” Optical Materials **12**(1), 1–18 (1999). 23

[59] U. Pedrazza, V. Romano, and W. Lüthy, “Yb3+: Al3+: sol–gel silica glass fiber laser,” Optical Materials **29**(7), 905–907 (2007). 23

[60] H. Cheng, C. Chen, and C. Tsay, “Transparent ZnO thin film transistor fabricated by sol-gel and chemical bath deposition combination method,” Applied Physics Letters **90**, 012,113 (2007). 24

[61] C. Brinker and G. Scherer, *Sol-Gel Science: The Physics and Chemistry of Sol-Gel Processing* (Academic Press, 1990). 24

[62] L. Yang and K. Vahala, “Gain functionalization of silica microresonators,” Optics Letters **28**(8), 592–594 (2003). 24, 39

[63] L. Yang, D. Armani, and K. Vahala, “Fiber-coupled erbium microlasers on a chip,” Applied Physics Letters **83**, 825 (2003). 24

[64] H. Etzel, H. Gandy, and R. Ginther, “Stimulated emission of infrared radiation from ytterbium activated silicate glass,” Applied Optics **1**(4), 534–536 (1962). 26

[65] H. Pask, R. Carman, D. Hanna, A. Tropper, C. Mackechnie, P. Barber, and J. Dawes, “Ytterbium-doped silica fiber lasers: versatile sources for the1-1.2 μm region,” IEEE Journal of Selected Topics in Quantum Electronics **1**(1), 2–13 (1995). 26

[66] U. Brauch, A. Giesen, M. Karszewski, C. Stewen, and A. Voss, "Multiwatt diode-pumped Yb: YAG thin disk laser continuously tunable between 1018 and 1053 nm," Optics Letters **20**(7), 713–715 (1995). 26

[67] R. Paschotta, J. Nilsson, A. Tropper, and D. Hanna, "Ytterbium-doped fiber amplifiers," IEEE Journal of Quantum Electronics **33**(7), 1049–1056 (1997). 27, 28

[68] Y. Zakharenkov, T. Clatterbuck, V. Shkunov, A. Betin, D. Filgas, E. Ostby, F. Strohkendl, D. Rockwell, and R. Baltimore, "2-kW Average Power CW Phase-Conjugate Solid-State Laser," pp. 1–2 (2007). 28

[69] H. Haus, *Waves and fields in optoelectronics.* (1984). 28, 68, 69

[70] M. Gorodetsky and V. Ilchenko, "Optical microsphere resonators: optimal coupling to high-Q whispering-gallery modes," Journal of the Optical Society of America B **16**(1), 147–154 (1999). 28

[71] B. Min, T. Kippenberg, and K. Vahala, "Compact, fiber-compatible, cascaded Raman laser," Optics Letters **28**(17), 1507–1509 (2003). 28

[72] Y. Jeong, J. Sahu, D. Payne, and J. Nilsson, "Ytterbium-doped large-core fiber laser with 1.36 kW continuous-wave output power," Optics Express **12**(25), 6088–6092 (2004). 29

[73] A. Holmes, R. Syms, M. Li, and M. Green, "Fabrication of buried channel waveguides on silicon substrates using spin-on glass," Applied Optics **32**(25), 4916–4921 (1993). 34

[74] G. Brusatin, M. Guglielmi, P. Innocenzi, A. Martucci, G. Battaglin, S. Pelli, and G. Righini, "Microstructural and optical properties of sol-gel silica-titania waveguides," Journal of Non Crystalline Solids **220**(2), 202–209 (1997). 34

[75] T. Kippenberg, S. Spillane, and K. Vahala, "Modal coupling in traveling-wave resonators," Optics Letters **27**(19), 1669–1671 (2002). 37

[76] Y. Zhou, Q. Thai, Y. Chen, and S. Zhou, "Monolithic Q-switched Cr, Yb: YAG laser," Optics Communications **219**(1-6), 365–367 (2003). 39

[77] R. Thrash and L. Johnson, "Upconversion laser emission from Ybˆ 3+-sensitized Tmˆ 3+ in BaY_2F_8," Journal of the Optical Society of America B **11**(5), 881–885 (1994). 39

[78] K. J. Vahala, "Optical microcavities," Nature **424**(6950), 839–846 (2003). URL `http://dx.doi.org/10.1038/nature01939`. 41, 64

[79] S. Arnold, M. Khoshsima, I. Teraoka, S. Holler, and F. Vollmer, "Shift of whispering-gallery modes in microspheres by protein adsorption," Optics Letters **28**(4), 272–274 (2003). 41

[80] K. De Vos, I. Bartolozzi, E. Schacht, P. Bienstman, and R. Baets, "Silicon-on-Insulator microring resonator for sensitive and label-free biosensing," Optics Express **15**(12), 7610–7615 (2007). 41

[81] A. Armani and K. Vahala, "Heavy water detection using ultra-high-Q microcavities," Optics Letters **31**(12), 1896–1898 (2006). 41

[82] J. Yang and L. Guo, "Optical sensors based on active microcavities," IEEE Journal of Selected Topics in Quantum Electronics **12**(1), 143–147 (2006). 41

[83] M. Lu, S. Choi, C. Wagner, J. Eden, and B. Cunningham, "Label free biosensor incorporating a replica-molded, vertically emitting distributed feedback laser," Applied Physics Letters **92**, 261,502 (2008). 41

[84] D. Armani, T. Kippenberg, S. Spillane, and K. Vahala, "Ultra-high-Q toroid microcavity on a chip," Journal High Energy Physics **8**, 37 (2000). 41

[85] A. Armani, D. Armani, B. Min, K. Vahala, and S. Spillane, "Ultra-high-Q microcavity operation in HO and DO," Applied Physics Letters **87**, 151,118 (2005). 42

[86] A. Schawlow and C. Townes, "Infrared and optical masers," Physical Review Letters **112**(6), 1940–1949 (1958). 47

[87] M. Stockman, "Nanofocusing of optical energy in tapered plasmonic waveguides," Physical Review Letters **93**, 137,404–137,404 (2004). 50, 64

[88] E. Cubukcu, E. Kort, K. Crozier, and F. Capasso, "Plasmonic laser antenna," Applied Physics Letters **89**, 093,120 (2006). 50, 64

[89] F. López-Tejeira, S. Rodrigo, L. Martin-Moreno, F. Garcia-Vidal, E. Devaux, T. Ebbesen, J. Krenn, I. Radko, S. Bozhevolnyi, M. Gonzalez, *et al.*, "Efficient unidirectional nanoslit couplers for surface plasmons," Nature Physics **3**(5), 324–328 (2007). 50, 64

[90] S. Lal, S. Link, and N. Halas, "Nano-optics from sensing to waveguiding," Nature Photonics **1**(11), 641–648 (2007). 50, 64

[91] M. Brongersma and P. Kik, "Surface plasmon nanophotonics," (2007). 50, 64

[92] M. Borselli, T. Johnson, and O. Painter, "Beyond the Rayleigh scattering limit in high-Q silicon microdisks: theory and experiment," Optics Express **13**(5), 1515–1530 (2005). 50

[93] M. Oxborrow, "Instrumentation and Measurement Techniques-Traceable 2-D Finite-Element Simulation of the Whispering-Gallery Modes of Axisymmetric Electromagnetic Resonators," IEEE Transactions on Microwave Theory and Techniques **55**(6), 1209–1218 (2007). 56

[94] P. Johnson and R. Christy, “Optical constants of the noble metals,” Physical Review B **6**(12), 4370–4379 (1972). 56, 59

[95] E. Palik, “Handbook of optical constants of solids,” (1985). 56, 59

[96] D. Rowland and J. Love, “Evanescent wave coupling of whispering gallery modes of adielectric cylinder,” IEEE Journal of Selected Topics in Quantum Electronics **140**(3), 177–188 (1993). 58, 62

[97] H. Ditlbacher, A. Hohenau, D. Wagner, U. Kreibig, M. Rogers, F. Hofer, F. Aussenegg, and J. Krenn, “Silver nanowires as surface plasmon resonators,” Surf. Sci Phys Rev Lett **95**, 257,403 (1974). 60, 64

[98] H. Miyazaki and Y. Kurokawa, “Squeezing visible light waves into a 3-nm-thick and 55-nm-long plasmon cavity,” Physical Review Letters **96**(9), 97,401 (2006). 60, 64

[99] J. Weeber, A. Bouhelier, G. Colas des Francs, L. Markey, and A. Dereux, “Submicrometer in-plane integrated surface plasmon cavities,” Nano Letters **7**(5), 1352–1359 (2007). 60, 64

[100] E. Vesseur, R. de Waele, H. Lezec, H. Atwater, F. de Abajo, and A. Polman, “Surface plasmon polariton modes in a single-crystal Au nanoresonator fabricated using focused-ion-beam milling,” Applied Physics Letters **92**, 083,110 (2008). 60, 64

[101] M. Hill, Y. Oei, B. Smalbrugge, Y. Zhu, T. de Vries, P. van Veldhoven, F. van Otten, T. Eijkemans, *et al.*, “Lasing in metallic-coated nanocavities,” Nature Photonics **1**(10), 589–594 (2007). 64

[102] S. Noda, M. Fujita, and T. Asano, “Spontaneous-emission control by photonic crystals and nanocavities,” Nature Photonics **1**(8), 449–458 (2007). 64

[103] V. Almeida, C. Barrios, R. Panepucci, and M. Lipson, “All-optical control of light on a silicon chip,” Nature **431**(7012), 1081–1084 (2004). 64

[104] Y. Gong and J. Vučković, “Design of plasmon cavities for solid-state cavity quantum electrodynamics applications,” Applied Physics Letters **90**, 033,113 (2007). 64

[105] A. Akimov, A. Mukherjee, C. Yu, D. Chang, A. Zibrov, P. Hemmer, H. Park, and M. Lukin, “Generation of single optical plasmons in metallic nanowires coupled to quantum dots,” Nature **450**(7168), 402–406 (2007). 64

[106] H. Raether, *Surface Plasmons on Smooth and Rough Surfaces and on Gratings: On Smooth and Rough Surfaces and on Gratings* (Springer-Verlag, 1988). 64

[107] H. Rokhsari and K. Vahala, "Ultralow loss, high Q, four port resonant couplers for quantum optics and photonics." Physical Review Letters **92**(25 Pt 1), 253,905 (2004). 67, 89

[108] M. Gorodetsky, A. Pryamikov, and V. Ilchenko, "Rayleigh scattering in high-Q microspheres," Journal of the Optical Society of America B **17**(6), 1051–1057 (2000). 67, 68

[109] V. Sandoghdar, F. Treussart, J. Hare, V. Lefevre-Seguin, J. Raimond, and S. Haroche, "Very low threshold whispering-gallery-mode microsphere laser," Physical Review A **54**(3), 1777 (1996). 69

[110] A. Adamson and J. Klerer, "Physical chemistry of surfaces," Journal of The Electrochemical Society **124**, 192C (1977). 70

[111] H. Rokhsari, S. Spillane, and K. Vahala, "Loss characterization in microcavities using the thermal bistability effect," Applied Physics Letters **85**, 3029 (2004). 71

[112] D. Hunter, W. Cornwell, T. Gilfedder, A. Franzen, and I. Andonovic, "SLOB: A switch with large optical buffers for packet switching," Journal of Lightwave Technology **16**(10), 1725 (1998). 81

[113] L. Eldada, R. Scarmozzino, R. Osgood Jr, D. Scott, Y. Chang, and H. Fetterman, "Laser-fabricated delay lines in GaAs for optically steeredphased-array radar," Journal of Lightwave Technology **13**(10), 2034–2040 (1995). 81

[114] R. Hayes and D. Yap, "GaAs spiral optical waveguides for delay-line applications," Journal of Lightwave Technology **11**(3), 523–528 (1993). 81

[115] G. Van den Hoven, R. Koper, A. Polman, C. Van Dam, J. Van Uffelen, and M. Smit, "Net optical gain at 1.53 μm in Er-doped AlO waveguides on silicon," Applied Physics Letters **68**, 1886 (1996). 82

[116] T. Kippenberg, S. Spillane, D. Armani, and K. Vahala, "Fabrication and coupling to planar high-Q silica disk microcavities," Applied Physics Letters **83**, 797 (2003). 82, 83

[117] T. Kitoh, N. Takato, M. Yasu, and M. Kawachi, "Bending loss reduction in silica-based waveguides by using lateraloffsets," Journal of Lightwave Technology **13**(4), 555–562 (1995). 86

[118] J. Dong, A. Shirakawa, and K. Ueda, "Numerical simulation of a diode-laser-pumped self-Q-switched Cr, Yb: YAG microchip laser," Optical Review **12**(3), 170–178 (2005). 91

[119] L. Mandel and E. Wolf, *Optical coherence and quantum optics* (Cambridge University Press, 1995). 95

[120] H. Carmichael, "Quantum trajectory theory for cascaded open systems," Physical Review Letters **70**(15), 2273–2276 (1993). 96

[121] D. Vernooy, A. Furusawa, N. Georgiades, V. Ilchenko, and H. Kimble, "Cavity QED with high-Q whispering gallery modes," Physical Review A **57**(4), 2293 (1998). 96